Solar Sail Trajectory Design for a Martian Moon Sample-return Mission

Master Thesis

Punit Naresh Gwalani

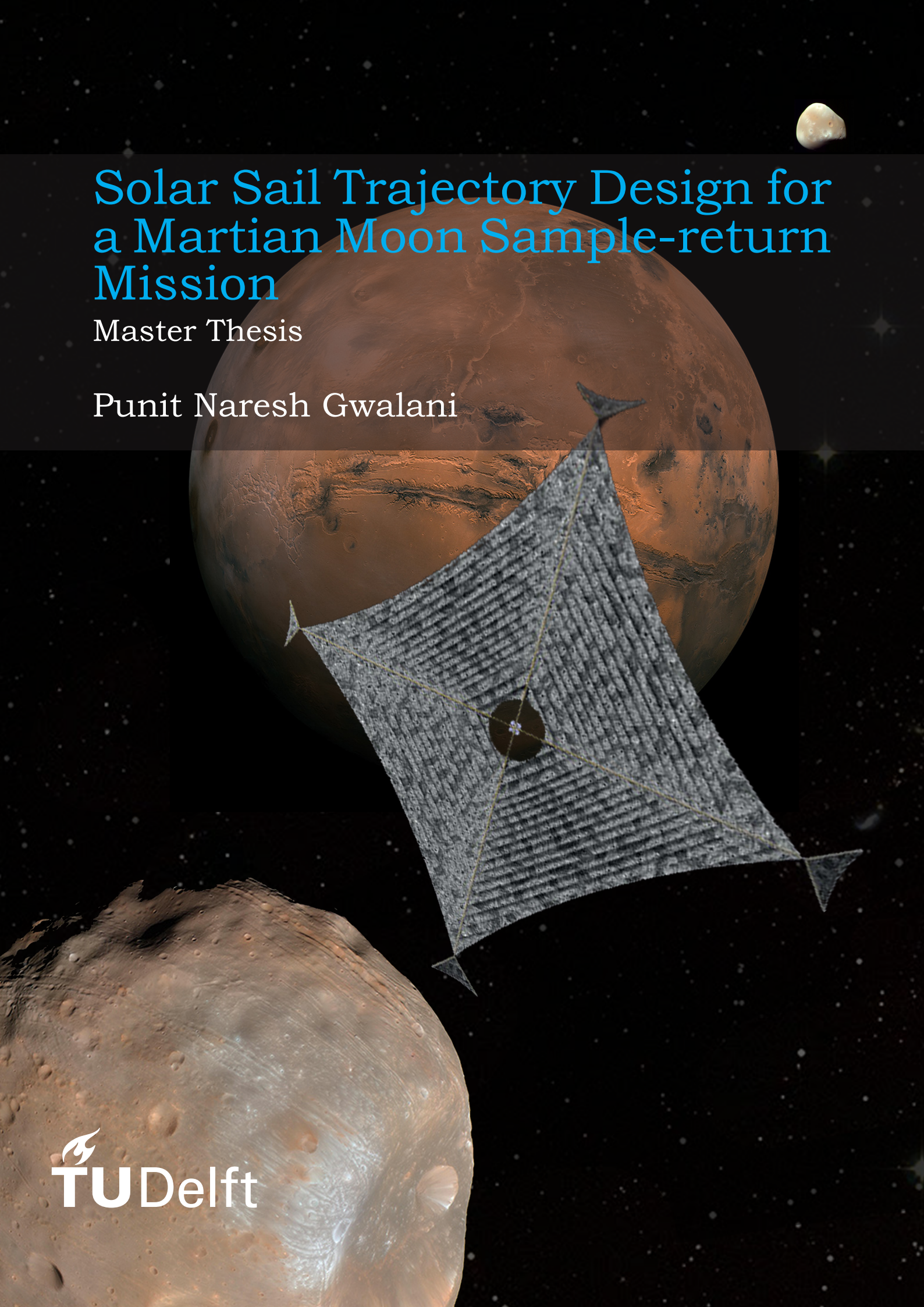

TU Delft

Solar Sail Trajectory Design for a Martian Moon Sample-return Mission

by

Punit Naresh Gwalani

Student Number:	5540011	
Project Duration:	5 April 2023 - 30 January 2024	
Thesis committee:	Dr.ir. E. Mooij	Committee Chair
	ir. K. J. Cowan MBA	Supervisor
	Dr. ir. J.G. de Teixeira da Encarnacao	External Examinator

Cover Image: A Solar-sail in the Martian system with moons Phobos and Deimos in the background. Created by compositing images of Mars, Deimos and Phobos retrieved from `https://photojournal.jpl.nasa.gov/`, and an artist's impression of solar sail Sunjammer (Image credit: L.Garde, Inc.).

TU Delft

Preface

With the completion of this thesis, I bid adieu to one of the most challenging yet beautiful arcs of my life. Looking back, the past 2.5 years at Delft were anything but smooth, but I can genuinely say that I've grown in ways I never imagined. To say the least, none of this would have been possible without the people who stood by me during this journey. I would like to take this moment to express my gratitude towards these individuals.

It was during my Bachelor's that I first encountered solar sailing; I was deeply intrigued by the technology and I had hoped to work on it someday in the future. So, when I discovered a course titled 'Special Topics in Astrodynamics' partially dedicated to this subject, I was genuinely excited to pursue it. Fortunately, after completing the course, Jeannette Heiligers agreed to supervise me for an MSc thesis on solar sails. I would like to thank her for the guidance and advice she provided during the initial stages of my thesis, helping me lay down its foundations. Her support towards the end was also invaluable in addressing certain critical aspects of my work. Two months into my thesis, my supervision was handed over to Kevin Cowan and firstly, I want to express my gratitude to him for agreeing to take over my supervision midway. I always used to look forward to our weekly meetings, as the constant brainstorming sessions, coupled with his advice and support, helped me navigate through my thesis. I also thoroughly enjoyed our non-thesis related conversations, which each time taught me something new.

I consider myself lucky to have made some beautiful friends during my time at Delft. To be candid, they were the ones who kept me sane, motivated, and made my life here truly enjoyable (and adventurous) beyond the computer screens. These include: the basketball gang, my flatmates at César Franckstraat 108, 71+108, and the master room 2.44 family. I also sincerely appreciate the 2.44 family's constant help throughout my thesis, from our study sessions to brainstorming sessions. Thank you very much, and as we move forward, my only wish is to stay connected with all of you.

Additionally, I would like to give a shout-out to two friends from RVCE who joined me in Delft: Advait and Gargi. Even though it's only been 6 months since Gargi arrived in Delft, she played a pivotal role in ensuring the completion of my thesis - providing me with tasty food, B&B service, infinite tolerance to my rants, and moral support. Then, there's Advait. It's still funny how we used to hang out in the same group back in RV, but never really spoke to each other. I'm glad to have had someone with whom I could start my journey in Delft. Advait has helped me in many ways, some of which he may not even be aware of - from listening to my rants and cooking sessions to exploring Europe together, assisting with assignments, playing cricket, and of course, always agreeing to come to my aid.

Finally, the biggest thank you to my parents. To say that whatever and wherever I am is because of them would be an understatement of unimaginable proportions. They have been pillars of support throughout my life - constantly cheering me on, guiding me, tolerating me, and caring for me. As I depart from my student life (for now), I only hope to make them proud and keep them happy.

Punit Naresh Gwalani
Delft, January 2024

Executive Summary

Mars has long captured the human imagination as a prime destination for space exploration; however, the natural satellites, Phobos and Deimos, have often been overlooked. But with the realization of their potential importance to future Mars-bound missions along with the mysteries surrounding their origins and compositions, there is a growing interest in these moons. Especially with a pioneer sample-return mission to these moons in the final stages of development, future mission concepts are already being explored to possibly revisit the moons - particularly by employing cost-effective low-thrust propulsion systems. Among the low-thrust propulsion options, solar sails are one of the most fascinating technologies that operate as a propellantless form of propulsion, relying solely on the the solar radiation pressure exerted by the solar photons. While the potential of solar sails for visiting Mars's moons has been briefly mentioned in the past, there is currently no existing study that thoroughly investigates their application in designing trajectories to Deimos and/or Phobos.

In this thesis, a solar sail propulsion technique is employed to investigate transfers between the Earth and a Martian moon for a sample-return mission, with Deimos taken as the case study. The focus is on designing time-optimal transfers, given the low-thrust nature of solar sails, with the primary objective of maximizing the duration of stay near the moon for a minimum feasible total mission duration. To achieve this, an optimal control problem (OCP) is formulated and solved by employing a direct pseudospectral method implemented through the PSOPT software package. Since direct methods necessitate a sufficiently accurate initial guess for optimization, the initial guess is obtained by applying a patched circular restricted three-body problem (CR3BP) method with the intention to find heteroclinic-like connections between the Lagrange points of two CR3BP systems. Each leg of the mission, namely the outbound leg from Earth to Deimos and the inbound leg from Deimos to Earth, traverses three CR3BP systems: Sun-Earth, Sun-Mars, and Mars-Deimos. They are considered to depart and arrive in the vicinity of Earth at the Sun-Earth (SE) L_2 Lagrange point, while near Deimos, the target is the Mars-Deimos L_1 point. The departure window from the SE L_2 point for the outbound trajectory is assumed as 2030-2032.

Before proceeding with initial guess generation the necessary dynamical model is set up by identifying the relevant perturbations in the Mars-Deimos CR3BP system. The initial guess is then generated by searching for heteroclinic-like connections between the SE L_2 and MD L_1 points, for which a Monte Carlo and differential evolution method is implemented. The primary objective of these methods is to minimize position and velocity errors for the solar-sail perturbed stable and unstable invariant manifolds originating from these Lagrange points, ensuring they fall below a satisfactory limit to serve as a viable initial guess. During the process of initial guess generation, it is also found that total mission durations of less than seven years are unattainable, and thus the maximum limit to the total mission duration is set to eight years. Considering this, the optimal control problem (OCP) yields a stay duration at the MD-L_1 of 329 days, with a total mission duration of 7.7 years.

While the use of the patched CR3BP approximation successfully yields valid time-optimal transfer trajectories between Earth and Deimos, the final outcome is considered sub-optimal. This sub-optimality arises from computational limitations associated with solving many revolution spiral escape and capture trajectories within the Martian system using the direct pseudospectral method. Consequently, a full end-to-end trajectory optimization is not performed. Instead, the outbound

and return legs are solved separately, with a partial dependence on each other. Despite this, the obtained solution is deemed sufficiently optimal for a preliminary mission concept. Furthermore, extending the same method to Phobos resulted in computational times for producing initial guesses nine times greater than that for Deimos. This renders the process highly inefficient with the available computational resources. Therefore, in future, alternative methods such as those employing a patched 2BP-CR3BP could be considered to generate transfers for similar missions either to Phobos alone or to both Phobos and Deimos within a single mission.

Nonetheless, this thesis demonstrates the feasibility of designing trajectories to and from the Martian moons using the fuel-free solar sail propulsion technology. If found to be potentially cost-efficient compared to existing space propulsion techniques, it will be interesting to see its practical realisation to explore these enigmatic moons.

Contents

Preface i

Executive Summary ii

List of Figures vi

List of Tables viii

Nomenclature ix

1 Introduction 1
- 1.1 Dynamical Approach . . . 3
- 1.2 Research Objective and Questions . . . 4
- 1.3 Report Outline . . . 4

2 Conference Article 6
- 2.1 Introduction . . . 7
- 2.2 Dynamical Model . . . 8
  - 2.2.1 Circular Restricted Three-body Problem . . . 8
  - 2.2.2 Reference Frames and Transformations . . . 9
  - 2.2.3 Solar sail Acceleration . . . 12
  - 2.2.4 Fourth-body Perturbations . . . 12
  - 2.2.5 J_2 Perturbations . . . 13
  - 2.2.6 Perturbations in the Martian System . . . 13
- 2.3 Transfer Design Framework . . . 14
- 2.4 Initial Guess . . . 15
  - 2.4.1 Design Approach . . . 16
  - 2.4.2 Monte Carlo Analysis . . . 17
  - 2.4.3 Differential Evolution . . . 19
- 2.5 Optimal Control Problem . . . 20
  - 2.5.1 Problem Definition . . . 20
  - 2.5.2 OCP Solver . . . 21
  - 2.5.3 Results . . . 21
- 2.6 Conclusion . . . 25
- 2.7 References . . . 26
- 2.8 Appendix: Fourth-body Perturbations . . . 27

3 Conclusion and Future Recommendations 28
- 3.1 Conclusion . . . 28
- 3.2 Future Works and Recommendations . . . 30

Bibliography 37

A Verification and Validation 38
- A.1 Dynamical Model . . . 38
  - A.1.1 Circular Restricted Three-body Problem . . . 38
  - A.1.2 Frame Transformations . . . 40

A.1.3 Solar sail Acceleration 43
A.1.4 Fourth-body Perturbation 44
A.1.5 J_2 Perturbation 45
A.2 PSOPT 45

B Numerical Techniques for Initial Guess Generation **49**
B.1 Integrator Selection 49
B.2 Differential Evolution Tuning 51

C Moon to Moon Transfer **53**

D Sensitivity of the manifold distance parameter **55**

E Additional Plots **58**

List of Figures

1.1 Images of the natural satellites of Mars taken by NASA's Mars Reconnaissance Orbiter (MRO) . . . 1
1.2 Fully deployed Near-Earth Asteroid (NEA) Scout's solar sail. Its side is the length of a school bus. . . . 3

A.1 Stable and Unstable invariant manifolds associated with the Earth-Moon L_1 point. . . . 40
A.2 States of Earth in the heliocentric inertial reference frame (H) . . . 41
A.3 Verification of frame transformation from a Sun-Mars CR3BP to a Mars-Moon CR3BP and vice versa - for position. . . . 41
A.4 Verification of the frame transformations between the Sun-Mars and Mars-Deimos CR3BP - for velocity. . . . 42
A.5 The motion of the Sun in an Earth-Moon system transformed using the analytical expression using literature [50] and the transformations employed in this thesis (labelled "Derived"). The transformations used in this thesis assume an inclination and raan of 0deg for generating this plot. Dotted lines are the lines joining the EM barycenter and the values obtained from the literature formulations. Green and red arrows are the scaled unit vectors representing the y and x-axis of the EM CR3BP frame, respectively. 43
A.6 Solar sail model verification using the data provided by the author of Ref. [25], Heiligers, for a lightness number of 0.05. . . . 43
A.7 Separate components of the fourth-body perturbation plotted in a Mars-Deimos CR3BP frame, assuming that Deimos' orbit lies in the ecliptic. The green solid arrow corresponds to acceleration by the fourth body on the particle, the blue arrow is the absolute acceleration between the CR3BP system and the perturber, and the red arrow indicates the total relative acceleration experienced by the particle. The dashed line joins the perturber and the particle at a certain instance along its trajectory. . . . 44
A.8 Verification of the fourth-body perturbation magnitude. The perturber is the Sun in a Mars-Phobos CR3BP reference frame planar to the ecliptic. This image is a snapshot at a particular instance in time for a specific orientation of the Sun. The perturbation magnitude is given as the ratio of the fourth-body perturbation due to the Sun ($|\mathbf{p_s}|$ or $|\mathbf{a_4}|$) and the point-mass gravitational acceleration of Phobos ($|\mathbf{p_m}|$ or $|\mathbf{a_p}|$). . . . 45
A.9 Norm of position and velocity errors between the PSOPT optimal results and reintegrated trajectory for leg 1. . . . 47
A.10 Interpolated control profile for the interplanetary phases of leg 1 along with the Legendre-Gauss-Lobatto (LGL) nodes displayed using black dots. . . . 47

B.1 Position and velocity error for various integrators against the CPU time for the Sun-Earth case. For each integrator, the position and velocity errors are proportional to the integrator tolerance - the largest errors are associated with the largest tolerance (10^{-5}) and the smallest errors with the smallest tolerance (10^{-11}). . . . 50
B.2 Position and velocity error for various integrators against the CPU time for the Mars-Deimos case. For each integrator, the position and velocity errors are proportional to the integrator tolerance - the largest errors are associated with the largest tolerance (10^{-5}) and the smallest errors with the smallest tolerance (10^{-11}). . . . 50

B.3 Convergence of the fitness over the generations for different values of the parameters - shown for leg 1. 52

C.1 Results of Monte Carlo analysis showing a scatter plot for the position error, velocity error and difference in the Jacobi constant computed in the Sun-Mars frame at the linkages. 53
C.2 Relation between position errors, velocity errors and maximum feasible difference in Jacobi constants. 54
C.3 Trajectory of the solution with sufficiently low linkage errors employing the locally optimal steering for a Deimos to Phobos transfer. The zoomed-in image shows the end state of the stable and unstable manifold at the linkage condition. It is plotted in the Mars-centered equatorial reference frame. 54

D.1 Classical (ballistic) one-dimensional invariant unstable manifolds propagated for different distance parameters (10^{-4}, 10^{-6} and 10^{-10}) from the sub-L_1 point of the Sun-Earth system for a solar sail with lightness number 0.01. Unstable branch 1 (in blue) is the exterior branch while unstable branch 2 (in orange) is the interior branch. The yellow dot is the Sun. 55
D.2 Exterior (unstable branch 1 in blue) and interior (unstable branch 2 in orange) unstable branches plotted from the SE sub-L_1 point for $\beta = 0.01$. The case labelled "Literature" corresponds to the plot obtained from reference [71] for $\epsilon = 10^{-4}$ with a cone angle of -20deg. Additionally, $\epsilon = 10^{-4}$, 10^{-5}, 10^{-6} and 10^{-4} for the same cone angle are also shown. The case labelled "$\beta = 0$" corresponds to the ballistic case. The blue dot is the Earth. 56

E.1 Perturbations in gravitational acceleration, normalized against the Phobos' point mass gravity, at an arbitrary point (x = 1.8) within the Mars-Phobos CR3BP system, observed from January 1, 2030, to January 1, 2033. 58
E.2 Selection of the time of flight for the ballistic segment. Mars' initial position is taken at J2000, for a circular orbit around the Sun. The black regions indicate no impacts, while the white grids are associated with impacts with Deimos. This was plotted for the unstable manifold from Mars-Deimos L_1, the same results were observed for the stable manifold. 59
E.3 Position and velocity errors at linkages shown for combinations of cone and clock angles for mission leg 1. α_1 and δ_1 correspond to the cone and clock angles of the unstable manifold (from Sun-Earth L_2), respectively, and α_2 and δ_2 to that of the stable manifold (from Mars-Deimos L_1). The green crosses represent the designs that impacted either Deimos or Mars. 59
E.4 Escape time of flight plotted against the departure epoch for mission leg 2 60
E.5 Locations at the Martian sphere of influence at which the trajectories either escape or get captured. Their respective time of flights within the Martian system are also specified. 60
E.6 Frequency distribution of trajectories with spiral time of flights less than 230 days and greater than 250 days for varying values of the right ascension of ascending node of Deimos' orbit on the ecliptic at the time of departure or arrival. 61
E.7 Alternate view of the PSOPT obtained optimal interplanetary trajectories with coordinate axes not scaled equally. It is plotted in the heliocentric inertial reference frame. . 62
E.8 Varying inclinations of trajectories arriving at or departing from the Mars-Deimos L_1 point within the Martian SOI with respect to the Sun-Mars plane. 62

List of Tables

A.1 The estimated and literature positions of the Lagrange points [62]. 39
A.2 The estimated and literature eigenvalues for the Sun-Earth CR3BP system [63] 39
A.3 Discontinuities at the linkages and arrival states for reintegrated trajectories for both legs. Those at linkages are obtained by forward and backward propagation of two separate phases while those at arrival are produced by full integration of the interplanetary trajectory. The non-dim discontinuity at arrival for leg 1 is computed in the Sun-Mars frame while the rest is in Sun-Earth. 46

B.1 Parameters for the tuned differential evolution algorithm for both the legs of the mission. 52

C.1 Characteristic parameters of the Mars-Phobos CR3BP system and Phobos' initial phase angle. Based on the values provided by NASA/JPL's Solar System Dynamics group [70]. 53

Nomenclature

Abbreviations

2BP	Two-body problem
ABM	Adams-Bashforth-Moulton
AEP	Artificial Equilibrium Point
AN	Ascending Node
CR3BP	Circular restricted three-body problem
DE	Differential Evolution
EM	Earth-Moon
EoM	Equations of Motion
JAXA	Japan Aerospace Exploration Agency
LGL	Legendre-Gauss-Lobatto
LPO	Lagrange Point Orbit
MC	Monte Carlo method
MD	Mars-Deimos
MMX	Martian Moon eXploration
MP	Mars-Phobos
NLP	Non-Linear Programming
OCP	Optimal Control Problem
PM	Planet-Moon
PSOPT	PSeudospectral OPTimizer
RK	Runge-Kutta
SE	Sun-Earth
SM	Sun-Mars
SOI	Sphere of influence
SP	Sun-Planet
SRP	Solar Radiation Pressure
ToF	Time of Flight
V&V	Verification and Validation

Latin Symbols

$\mathbf{D}$	Initial guess design variable
$\mathbf{l}$	Primer vector
$\mathbf{n}$	Sail normal vector
$\mathbf{r_s}$	Sun-sail line
$\mathbf{R}$	Position vector in inertial frame
$\mathbf{r}$	Position vector in synodic frame
$\mathbf{v}$	Eigenvector
$\mathbf{x}$	State vector
B	Sun-sail reference frame
G	Universal Gravitational constant $[\mathrm{m}^3 kg^{-1} s^{-2}]$
g_1	State linkage error requirement penalty
g_2	Impact penalty
H	Heliocentric inertial reference frame
h	Altitude
i	Inclination [deg]
J	Objective Function
JC	Jacobi constant [-]
L_i	Lagrange Point, $i \in \{1, 2, 3, 4, 5\}$
l_i	Mission legs, $i \in \{1, 2\}$
M	Mars centered reference frame
m	Mass [kg]
p_i	Phases of the mission, $i \in \{1, 2, 3, 4, 5, 6\}$
S	Synodic reference frame
t	Time [s, non-dim]

t_{link}	Linkage fraction
U	Effective gravitational potential
w	DE fitness weights
X, Y, Z	Inertial coordinates
x, y, z	Synodic coordinates

Greek Symbols

α	Sail cone angle [deg]
β	Lightness number
δ	Sail clock angle [deg]
ϵ	Distance parameter
γ	Eigenvalues
λ	CR3BP unit of length [km]
μ	CR3BP mass ratio [-]
Ω	Right ascension of ascending node [deg]
ω	Angular velocity [rad/s]
τ	CR3BP unit of time [s]

Superscripts

$\ddot{}$	Double derivative with time
$\dot{}$	Single derivative with time
$\hat{}$	Unit vector
$\tilde{}$	Dimensionalized values
*	Optimal attitude

Subscripts

4	Corresponding to the fourth-body
arr	Corresponding to arrival
dep	Corresponding to departure
E	Equatorial
EC	Ecliptic
ig	Corresponds to an initial guess
$link$	Corresponding to linkage point
s	Corresponding to stable manifold
us	Corresponding to unstable manifold

1 Introduction

Despite the extensive exploration of Mars, the origins and characteristics of its two moons, Phobos and Deimos, remain largely enigmatic. Currently, there are two main contesting hypotheses regarding the origins of the Martian moons. One hypothesis states that they are captured asteroids, while the other states that they were formed in-situ through accretion either during the formation of Mars or by a giant impact on Mars [1]. By confirming either hypothesis through observations and sample-return missions, valuable insights can be gained into either the delivery process of volatiles to the inner planets or the composition of Mars' primordial material, and potentially the composition of its impactor, depending on the confirmed theory [1, 2]. Moreover, the characterisation of these moons might hold additional significance to the future manned and unmanned exploration of the Martian system. A platform or orbiter around Phobos and Deimos apart from performing in-situ science could also be used for monitoring the Martian atmosphere, space weather, data relay for the Martian and interplanetary spacecrafts (increasing overall bandwidth, mission operation time and reducing risks during solar conjunctions), in-situ resource utilization and supporting human Mars surface operations [3]. Additionally, human exploration of Phobos has been suggested as a precursor for a successful human mission to the Martian surface and if the moons do contain hydrated minerals, they could also be exploited for an economical mission to Mars [4]. The scientific significance of the exploration of these moons, as well as their potential utility in future human exploration, make Phobos and Deimos a compelling destination for future space exploration efforts [5]. As a visual reference, the images of Phobos and Deimos are shown in Fig. 1.1a and 1.1b, respectively.

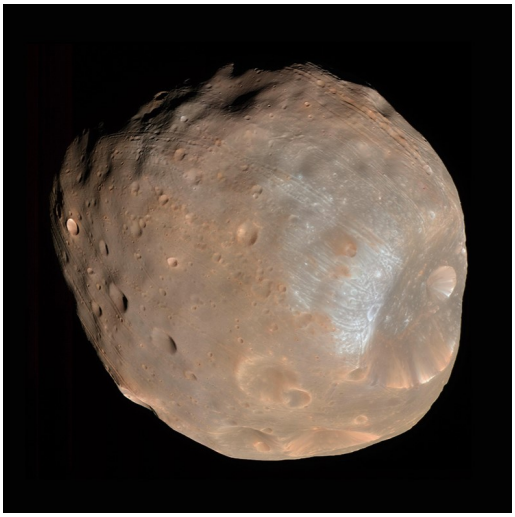

(a) Phobos

(b) Deimos

Figure 1.1: Images of the natural satellites of Mars taken by NASA's Mars Reconnaissance Orbiter (MRO)[1]

Recognizing their importance, multiple efforts have been taken in the past to photograph these moons through missions such as Mariner 9, Viking orbiters and landers, Phobos 2, Mars Reconnaissance Orbiter, Mars Odyssey spacecraft, Mars Global Surveyor and ESA's Mars Express, with

[1] `https://photojournal.jpl.nasa.gov/`

a certain bias towards Phobos [6]. To date, three dedicated missions have been launched to Phobos, namely Phobos 1, Phobos 2, and Fobos-Grunt, all of which have failed to accomplish their objectives [7]. Thus, there has yet to be a successful dedicated mission for the exploration of the moons.

In recent years, various space agencies have proposed missions to explore the Martian moons, Phobos and Deimos. Among these are PADME, PANDORA, and MERLIN by NASA [8, 9], DePihne and PHOOTPRINT by ESA [10, 11], and MMX (Martian Moon eXploration) by JAXA. A few of these proposals also included a sample-return component in their mission design. So far, only the MMX mission has been approved and scheduled for launch in 2024 with a mission duration of 5 years, in collaboration with NASA, ESA, DLR and CNES [12]. The goal of the MMX mission is to uncover the origins of the Martian moons and gain insight into the circum-Martian environment. This will be achieved through a combination of remote observations from orbit, sample return from Phobos, and a rover mission on the surface of Phobos, being developed by DLR and CNES [12].

As of the first quarter of 2022, MMX had begun phase-C of its development schedule and is currently on track for its planned launch in 2024 [12]. Although a dedicated mission to the Martian moons with a sample return from Phobos is already underway, there still could be a requirement for additional missions to the Martian moons. Given the short three-year operation period in the Martian system, MMX is limited in the amount of science it can collect from both the returned sample and remote observations, though it is optimized for maximum feasible output [12]. This, therefore, leaves room for follow-on missions to supplement the scientific return from the MMX mission [3, 13]. The follow-up spacecrafts can be engineered to maybe offer more coverage, observe key areas of interest, sample Deimos, perform in-situ analysis, or even return samples from the other targets of interest on Phobos to complement the data from MMX. For example, if the giant impact hypothesis for the formation of the Martian moons is confirmed by MMX, the returned sample may have a disproportionate mix relative to Phobos' bulk fraction, necessitating further surface sampling to better understand the proportion of the progenitors that make up the moon [3]. Furthermore, if short mission duration is not a strict requirement, a potentially low-cost mission using low-thrust propulsion to and from the moons could be a preferred solution.

Compared to their chemical engine counterparts, low-thrust engines provide a more fuel-efficient propulsion technique. This approach could potentially increase the payload capacity of the mission and possibly allow for more science; however, at the expense of larger time-of-flight. Several previous studies have envisioned the use of low-thrust propulsion for the exploration of Phobos and Deimos [14, 15, 16, 17], but only Englander et al. [18] investigated a sample-return mission using low-thrust propulsion, specifically Solar Electric Propulsion (SEP). However, it does not explicitly study the dynamics within the Martian Sphere of Influence (SOI). This study aims to fill this gap by exploring the feasibility of using a solar sail as the sole low-thrust propulsion technique for designing a sample-return mission from the Martian moons.

A solar sail, shown in Fig. 1.2, is a low-thrust propulsion technique which propels the spacecraft by exploiting the solar radiation pressure generated by the photons reflecting off its thin reflective membrane [19]. The idea of leveraging sunlight to propel in space was first envisioned by Johannes Kepler in 1607 and was deemed viable when James Clerk Maxwell in 1873 theoretically proved that light exerts pressure [20]. In fact, solar radiation pressure played a vital role in the Mariner 10's success in 1974 when it was actively controlled for the first time using the spacecraft's solar panels; it became the first satellite to rendezvous with two planets, Venus and Mercury [21]. However, it was only in 2010 that the first dedicated solar-sail mission, IKAROS, was flown by JAXA [22]. Since then, several missions have been successful in demonstrating and testing solar-sail technology, such as NASA's NanoSail-D2 in 2010 [23], the Planetary Society's LightSail-1 (2015) and LightSail-

2 (2017) [24], and most recently Gama's Alpha (2023) [2].

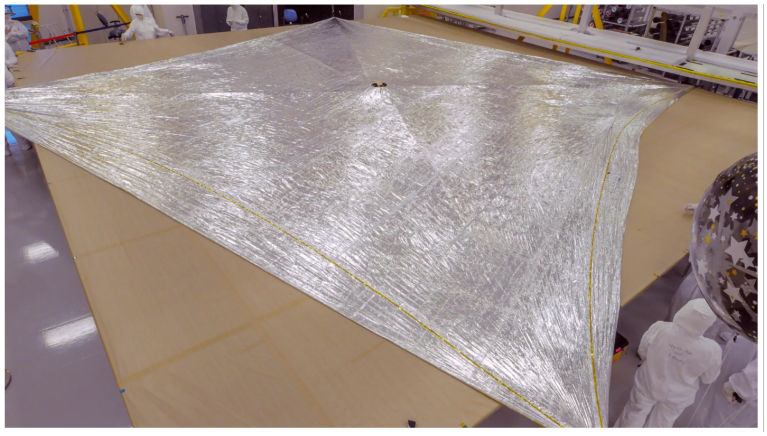

Figure 1.2: Fully deployed Near-Earth Asteroid (NEA) Scout's solar sail. It is the length of a school bus.[3]

Solar sails offer a key advantage over conventional and low-thrust propulsion systems by providing continuous acceleration without the need for additional expendable fuel, limited only by the sail's lifespan. This advantage makes solar sails attractive for a variety of novel missions, for example, space weather warning missions [25], pole-sitters [26, 27], additional highly non-Keplerian orbits [28, 29, 30] and futuristic missions beyond the Solar System [31, 32, 33]. Owing to the absence of fuel, the use of solar sails has also been investigated for sample-return missions from terrestrial planets and small bodies, with it proving to be a promising form of propulsion to enable a rather cost-efficient sample-return in a few cases [19, 34, 35, 36, 37]. Extending upon this, solar sails have also been proposed for a sample-return mission from the moons of Mars [38, 39]. Matloff et al. [39] evaluated the preliminary feasibility of a solar-sail equipped spacecraft to return samples from the Martian moons by not only using solar sails for inter-moon transfers within the Martian system but also by utilizing it to accomplish aerocapture at both Mars and Earth. However, the study did not include a detailed trajectory design nor did it solely rely on solar-sail propulsion. Additionally, there is currently no existing literature that specifically addresses the design of a solar-sail trajectory to the Martian moons, let alone a sample-return mission. Therefore, the current research will focus on addressing this gap in the literature.

1.1. Dynamical Approach

In most of the previous studies, the trajectories near the Martian moons were designed using three-body dynamics [16, 40, 41, 42, 43]. This is attributed to the small masses of the moons, and also the proximity to Mars in the case of Phobos, due to which their sphere of influence is extremely small compared to their sizes. Thus, making it impractical to have a Keplerian orbit around them. Therefore, to arrive in the vicinity of Phobos and Deimos a multi-body dynamical model is preferred [7].

The circular restricted three-body system (CR3BP) is one of the most commonly used multi-body dynamical models. It comprises of three gravitationally interacting bodies: two celestial bodies and a spacecraft, whose mass is assumed to be negligible. The CR3BP model reveals several dynamical structures, such as Lagrange points, Lagrange point orbits (LPOs) and invariant manifolds that aid in mission design, which otherwise are not easily discernible using a two-body problem (2BP)

[2] https://gamaspace.super.site/

[3] https://www.nasa.gov/humans-in-space/nasas-near-earth-asteroid-cubesat-goes-full-sail/

approximation [44]. For instance, one-dimensional and two-dimensional invariant manifolds associated with the Lagrange points and Lagrange point orbits (LPOs) have been employed in the past to design low-energy efficient transfers between celestial bodies; results of which closely align with the optimized solutions in a full N-body system [45].

Similar to a patched-conic approach, a system with more than three bodies can be decomposed into multiple CR3BP systems. A transfer from one celestial body to another can be achieved by finding intersections between the invariant manifolds originating from the LPOs or Lagrange points near the bodies of interest present in different CR3BP systems. This modelling technique is known as a patched CR3BP method, and the trajectories are called heteroclinic orbits or connections [44]. However, intersections between the manifolds for different CR3BP systems do not always exist, for example: there are no intersections between the Sun-planet CR3BPs of the inner planets. To bypass this problem, a patched 2BP-CR3BP model was proposed [46]. A study by Park [16] for a low-thrust mission to Phobos and Deimos used electric-propulsion in a patched 2BP-CR3BP model for trajectory design, and similarly, Canales et al. [40] employed the same to design Phobos-Deimos inter-moon transfers.

Alternatively, low-thrust propulsion can be used to replace and manipulate the standard invariant manifolds to find suitable intersections between the restricted three-body models, as shown by Mingotti et al. [47] for the Sun-Earth and Sun-Mars CR3BP systems [47]. Likewise, solar sail perturbed manifolds have also been employed for the transfers between different Sun-Planet CR3BP systems [48, 49, 50].

For a preliminary trajectory design, a patched CR3BP approach ideally offers a sufficiently accurate model that considers the dominant perturbing bodies. It serves as a good initial estimate for transitioning to a higher-fidelity ephemeris model for further accurate analysis. Furthermore, the equations of motion (EoM) governing the CR3BP system can be easily adjusted to incorporate additional perturbations during the preliminary design phase. Therefore, given the dynamical constraints near Phobos and Deimos, and the proven feasibility of using solar-sail propulsion for trajectory design between Earth and Mars using a patched CR3BP, this study employs a patched CR3BP model. This approach also eliminates the need to define two different sets of EoMs, as required in a patched 2BP-CR3BP approach.

1.2. Research Objective and Questions

The present research considers Deimos as the case study for designing a sample-return mission from a Martian moon. Following this and the introduction, the research objective for the thesis is:

"To design solar-sail propelled transfer trajectories by leveraging heteroclinic-like connections for a sample-return mission from the Martian moon Deimos, with the objective to maximize the scientific output."

The research objective can further be achieved by answering the following set of research questions:

1. *How feasible is patched CR3BP as a technique to design trajectories for a sample-return mission from a Martian moon?*
2. *What is the maximum feasible duration of stay in the vicinity of Deimos for a given possible minimum mission duration?*

1.3. Report Outline

In Chapter 2, the research questions outlined in the previous section will be addressed through an AAS/AIAA Astrodynamics Specialist Conference paper titled "Solar sail trajectory design for

a Martian moon Sample-return mission." The paper structure commences with an abstract and introduction. It then provides an overview of the dynamical models employed, followed by a discussion on the trajectory design framework and the method employed to generate initial guesses. Subsequently, the paper delves into the formulation of the optimal control problem, utilizing the initial guesses to derive final optimal trajectories. The concluding section summarizes the findings.

Chapter 3 follows the article and addresses the research questions posed. Additionally, the chapter proposes future recommendations based on the obtained results. This is followed by three appendices: Appendix A is dedicated to the verification and validation of the models employed, and Appendix B discusses settings for the numerical techniques used in the analysis. Appendix C offers observations from preliminary analyses focusing on Deimos to Phobos transfer utilizing solar sail. Appendix D discusses the sensitivity of the distance parameter. Finally, Appendix E presents additional plots that back the discussions in the article.

2 Conference Article

This chapter acts as the main body of the report with the content laid down in the form of a conference article for the AAS/AIAA Astrodynamics Specialist Conference.

AAS 08-XXX

SOLAR-SAIL TRAJECTORY DESIGN FOR A MARTIAN MOON SAMPLE-RETURN MISSION

Punit Naresh Gwalani*, and Kevin Cowan†

With a dedicated mission to the Martian moons, Phobos and Deimos, set to launch soon, there is a growing interest in further exploring these moons using low-thrust propulsion. This paper investigates the trajectory design for a sample-return mission from Deimos using fuel-free solar sail propulsion technology, aiming to maximize operational time near Deimos within a minimum permissible total mission duration. Time-optimal transfers between Earth and Deimos are sought by formulating and solving an optimal control problem using a direct pseudospectral method. Initial guesses for the direct method are generated by considering a patched circular restricted three-body problem (CR3BP) approximation and by searching for heteroclinic-like connections between the Sun-Earth and Mars-Deimos systems using the differential evolution algorithm. The obtained solution, with a maximum mission duration set to eight years based on the insights from initial guess generation, results in an optimal duration of stay at Deimos of 329 days with a mission duration of 7.7 years. Although the patched CR3BP approximation demonstrated valid transfer solutions for this study, it is deemed computationally inefficient for future trajectory designs for similar mission concepts targeting either only Phobos or both moons at once. Nevertheless, the trajectories obtained back and forth from Deimos are sufficiently optimal for a preliminary mission concept and validate the feasibility of achieving such a mission employing a solar sail.

INTRODUCTION

Mars, despite being one of the focal points of space exploration, still holds mysteries regarding the origin and characteristics of its moons, Phobos and Deimos. Two contesting hypotheses exist: one states that these moons are captured asteroids, while the other suggests in-situ formation through accretion or a giant impact.[1] Unravelling this mystery can provide valuable insights into either the delivery processes of the volatiles to the inner planets or Mars' primordial composition.[2] Further, these moons could potentially also hold significance for future Mars missions, offering platforms for diverse scientific and logistical operations.[3]

Historically, multiple efforts have been taken to photograph these moons, with a certain bias towards Phobos.[4] To date, three dedicated missions have been launched to Phobos, namely Phobos 1, Phobos 2, and Fobos-Grunt, all of which fell short of their objectives.[5] In recent years while several missions have been proposed to explore the moons,[6–9] so far only Martian Moon eXploration (MMX) by JAXA has followed through, with an expected launch in 2024.[10] Although the development of MMX is already underway, there may arise a future need for additional scientific exploration of the moons. This could serve to either supplement the scientific findings from MMX, including resampling of Phobos, or explore additional targets such as sampling Deimos, which has received comparatively less attention.[3,10,11]

If short mission duration is not a strict requirement, a potentially low-cost mission using low-thrust propulsion to and from the moons could be a preferred solution. Among low-thrust propulsion, one of the fascinating technologies is a solar sail. It propels a spacecraft by exploiting the solar radiation pressure generated by the photons reflecting off its thin reflective membrane.[12] The idea of leveraging sunlight to propel in space was first envisioned by Johannes Kepler in 1607 and over the years this has evolved into the concept of a solar sail.[13] Despite being around for almost a century, it was only in 2010 that the first dedicated solar-sail mission, IKAROS by JAXA, was flown.[14] Since then, several missions have been successful in demonstrating

*Graduate Student, Faculty of Aerospace Engineering, Delft University of Technology, Deft, The Netherlands, punitgwalani27@gmail.com.

†Education Fellow and Lecturer, Faculty of Aerospace Engineering, Delft University of Technology, Deft, The Netherlands.

and testing solar-sail technology, such as NASA's NanoSail-D2 in 2010,[15] the Planetary Society's LightSail-1 (2015) and LightSail-2 (2017),[16] and most recently Gama's Alpha (2023) *.

The key advantage of a solar sail over conventional and other low-thrust propulsion systems is its ability to generate thrust without the need for expendable fuel, limited only by the sail's lifespan. This capability enables various missions, which otherwise may not be feasible or cost-effective with other propulsion systems.[17–23] Similarly, the application of solar sails has also been investigated for sample-return missions from terrestrial planets and small bodies, with it proving to be a promising form of propulsion to enable rather cost-efficient sample-return for Mercury and Near Earth Asteroids, compared to their conventional counterparts.[12,24–26] Building upon this application, the idea of a solar sail for a sample-return mission from the Martian moons has been tossed around in the past, notably its application in retrieving samples from Phobos or Deimos as part of a two-spacecraft interplanetary CubeSat.[27,28] However, to date, no trajectory design has been performed using a solar sail for a mission to and/or from the Martian moons. Thus, this study aims to design the trajectory for a sample-return mission to a Martian moon, with Deimos as the case study.

Designing a Keplerian orbit around these moons is challenging due to their small sphere of influence (SOI) compared to their sizes. Therefore, a multi-body dynamical model is preferred to arrive in the vicinity of Phobos or Deimos.[5] To design trajectories to these moons, past studies such as by Park[29] and Canales et al.[30] have thus incorporated a patched 2BP-CR3BP (two-body problem - circular restricted three-body problem) approach. In contrast, the present study explores the use of a patched CR3BP approach to design transfers, where, similar to a patched-conic approach, an N-body system is decomposed into multiple CR3BP systems. Considering the dominant perturbing gravitational forces along the mission, it can serve as a good initial estimate for transitioning to a higher-fidelity ephemeris model. Additionally, several previous studies have demonstrated solar-sail transfers between different CR3BP systems using the same.[31–33]

In this study, the departure/arrival locations near Earth and Deimos are considered to be the Sun-Earth L_2 Lagrange point and the Mars-Deimos L_1 point, respectively. For these, heteroclinic-like connections between different CR3BP systems in the patched model are sought using the Monte Carlo method and differential evolution. The results obtained from differential evolution then serve as an initial guess for the optimal control problem (OCP), where a direct pseudospectral method is employed to find time-optimal transfers.

The paper is organized as follows: first, the relevant mathematical models governing the dynamical model are discussed, along with the relevant perturbations for the analysis. The second section provides an overview of the transfer design framework, followed by a discussion of the approach and results of the initial guess generation in the third section. The fourth section presents the optimal control problem and its results, and finally, the paper ends with a conclusion section.

DYNAMICAL MODEL

As discussed in the previous section, a solar-sail augmented patched CR3BP dynamical framework has been adopted to design the trajectories for the sample-return mission. Additionally, relevant dominant perturbations due to fourth bodies and non-spherical gravity fields have also been incorporated. The following subsections individually describe the various components of this dynamical framework, including the reference frame definitions and transformations.

Circular Restricted Three-body Problem

The CR3BP is an autonomous dynamical model that describes the motion of a body with negligible mass (m_3), such as a spacecraft, under the gravitational influence of two larger point masses (m_1 and m_2), called the primaries, that move in a circular orbit about their barycenter. Here, the mass of the first primary (m_1) is larger than the second primary (m_2).

The motion is described in a barycentric synodic reference frame $S(\hat{\mathbf{x}}, \hat{\mathbf{y}}, \hat{\mathbf{z}})$ that rotates at a constant angular velocity ω about $\hat{\mathbf{z}}$ as shown in Figure 1. To aid with numerical integration, mass, length, and time are non-dimensionalized by normalizing with the sum of the masses of the primaries ($m_1 + m_2$), the distance

*https://gamaspace.super.site/

between the primaries (λ), and the inverse of the angular velocity ($\tau = 1/\omega$), respectively. Consequently, the masses of the primaries are defined as $m_1 = (1-\mu)$ and $m_2 = \mu$, with $\mu = m_2/(m_1+m_2)$ being the mass ratio. The equations of motion for the CR3BP model are thus then written as:

$$\ddot{x} = 2\dot{y} + \frac{\partial U}{\partial x} + a_x, \quad \ddot{y} = -2\dot{x} + \frac{\partial U}{\partial y} + a_y, \quad \ddot{z} = \frac{\partial U}{\partial z} + a_z \tag{1}$$

where U represents the effective gravitational potential given by Eq. (2), and a_x, a_y and a_z are the components of the total perturbing acceleration ($\mathbf{a}$). In this study, the total perturbing acceleration comprises the solar sail acceleration ($\mathbf{a_s}$), fourth-body perturbation ($\mathbf{a_4}$) and J_2 perturbations ($\mathbf{a_{J_2}}$), which are further elaborated upon in subsequent subsections.

$$U = -\frac{1}{2}(x^2+y^2) - \frac{1-\mu}{r_1} - \frac{\mu}{r_2} \tag{2}$$

For this system, there exists a first integral of motion called Jacobi Constant (JC), expressed in Eq. (3). A lower JC corresponds to a greater energy of a spacecraft in the CR3BP system.

$$JC = 2U - (\dot{x}^2 + \dot{y}^2 + \dot{z}^2) \tag{3}$$

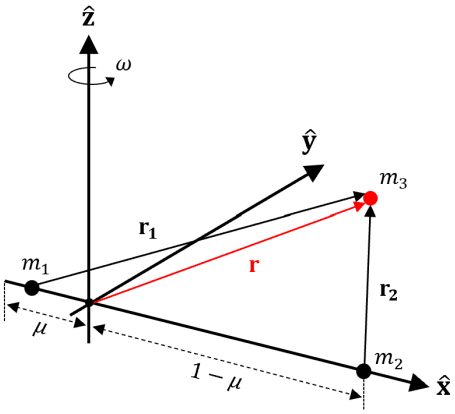

Figure 1: Schematic representation of the CR3BP and the rotating reference frame $S(\hat{\mathbf{x}}, \hat{\mathbf{y}}, \hat{\mathbf{z}})$.

Moreover, the CR3BP also has five equilibrium solutions called the Lagrange points, where a particle with zero velocity experiences no acceleration relative to the rotating frame and are computed by equating the gradient of the potential to zero ($\nabla U = 0$). Three of the Lagrange points (L_1, L_2 and L_3) are collinear with the primaries along the x-axis while the other two (L_4 and L_5) form an equilateral triangle with primaries in the $(\hat{\mathbf{x}}, \hat{\mathbf{y}})$ plane.

Finally, the values of the characteristic parameters (μ, λ and τ) for different CR3BP systems of interest to this study are compiled in Table 1.

Table 1: Characteristic parameters of different CR3BP systems. Computed using the physical data for the planets and satellites provided by NASA/JPL's Solar System Dynamics group[34]

System	μ [-]	λ [km]	τ [s]
Sun-Earth (SE)	$3.0542 \cdot 10^{-6}$	$1.495958219 \cdot 10^{8}$	$5.022548 \cdot 10^{6}$
Sun-Mars (SM)	$3.2272 \cdot 10^{-7}$	$2.279406953 \cdot 10^{8}$	$9.446647 \cdot 10^{6}$
Mars-Deimos (MD)	$2.2462 \cdot 10^{-9}$	$2.34632 \cdot 10^{4}$	$1.7316 \cdot 10^{4}$

Reference Frames and Transformations

Given the patched CR3BP approach, the states have to be propagated in three separate CR3BP systems (Sun-Earth, Sun-Mars and Mars-Deimos). To ensure continuity between trajectories in various CR3BP systems, and the computation of fourth-body perturbations and solar-sail acceleration within specific systems, frame transformations are necessary. Consequently, this also requires the formulation of intermediate inertial reference frames. The subsequent discussion delves into the necessary reference frames and transformations. Before proceeding with this, a few prior assumptions are stated regarding the orbits of planets and moons:

- Given the small inclination of Mars to the ecliptic, it is assumed that Earth and Mars are planar.
- Given Deimos' inclination of roughly 1.8 deg to the Martian equatorial plane,[34] it is assumed to lie along Mars' equator inclined at 26 deg to the ecliptic.

Inertial reference frames: Three distinct inertial reference frames are defined: the Heliocentric inertial reference frame $H(\tilde{X}_H, \tilde{Y}_H, \tilde{Z}_H)$, Mars-centred ecliptic inertial frame $M_{EC}(\tilde{X}_{EC}, \tilde{Y}_{EC}, \tilde{Z}_{EC})$ and Mars-centred equatorial inertial frame $M_E(\tilde{X}_E, \tilde{Y}_E, \tilde{Z}_E)$, where the tilde ($\tilde{}$) denotes dimensional quantities.

The Heliocentric inertial frame, shown in Figure 2 in black, is centred at the Sun, where the $\tilde{X}_H$-axis points towards the vernal equinox (at J2000), $\tilde{Z}_H$-axis perpendicular to the ecliptic plane and the $\tilde{Y}_H$-axis completes the right-handed reference frame. The Mars-centered ecliptic frame maintains the same orientation but with only its origin shifted to the centre of Mars. In contrast, the Mars-centred equatorial frame (in green in Figure 2) has its $\tilde{X}_E$-axis aligned with Deimos' ascending node (AN) on the ecliptic plane, the $\tilde{Z}_E$-axis is directed perpendicular to the Martian equatorial plane and the $\tilde{Y}_E$-axis completes the right-handed system. The orientation of the M_E frame relative to the M_{EC} frame is defined by two angles: the inclination to the ecliptic (i) and the right ascension of the ascending node (Ω), as illustrated in Figure 2. Deimos is assumed to have a constant Ω equal to 83 deg.[34] Alongside the inertial reference frames, Figure 2 also show the Sun-Mars ($S_{SM}(x_{SM}, y_{SM}, z_{SM})$), in blue, and Mars-Deimos ($S_{MP}(x_{MD}, y_{MD}, z_{MD})$), in red, CR3BP reference frames.

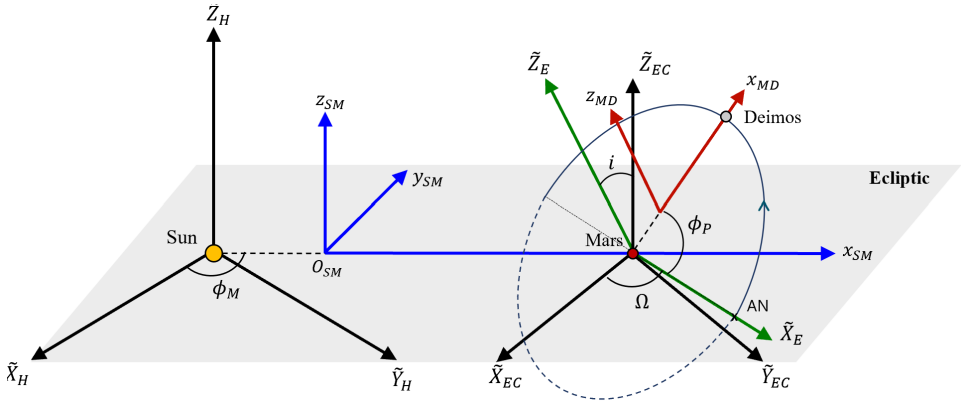

Figure 2: Schematic of Heliocentric inertial reference frame $H(\tilde{X}, \tilde{Y}, \tilde{Z})$, Sun-Mars CR3BP frame $S_{SM}(x_{SM}, y_{SM}, z_{SM})$, Mars-centred ecliptic inertial frame $M_{EC}(\tilde{X}_{EC}, \tilde{Y}_{EC}, \tilde{Z}_{EC})$ and Mars-centred equatorial inertial frame $M_E(\tilde{X}_E, \tilde{Y}_E, \tilde{Z}_E)$.

CR3BP to Inertial frame: The transformation from a synodic CR3BP reference frame to an inertial frame is described in the following Eqs. (4) - (6). This is only applicable when the z-axis of the CR3BP reference frame is parallel to the $\tilde{Z}$-axis of an inertial frame. First, the origin of the CR3BP system (barycenter) is translated to the first primary (for example Sun in Sun-Earth or Mars in Mars-Deimos system) by:

$$\mathbf{r}' = \mathbf{r} + \begin{bmatrix} \mu & 0 & 0 \end{bmatrix}^T \tag{4}$$

following which the position is dimensionalized and rotated clockwise about the z-axis by a phase angle (ϕ), which is the angle between the reference axis of the inertial frame ($\tilde{X}_H$ for the heliocentric frame and $\tilde{X}_E$ for the Mars-centered equatorial plane, refer Figure 2) and the line joining the primaries:

$$\tilde{\mathbf{R}} = \mathbf{T}_z(-\phi)\tilde{\mathbf{r}}' \tag{5}$$

where $\mathbf{T_z}$ is the rotation matrix about the z-axis. Similarly, the velocity in the inertial reference frame is given by:

$$\dot{\tilde{\mathbf{R}}} = \mathbf{T}_z(-\phi)(\dot{\tilde{\mathbf{r}}} + \boldsymbol{\omega} \times \tilde{\mathbf{r}}') \tag{6}$$

The phase angle is computed using the Eq. (7):

$$\phi = \phi_0 + t \tag{7}$$

where ϕ_0 is the angle at J2000 and t is the non-dimensional time in the respective CR3BP system. Table 2 lists initial phase angles for all the relevant CR3BP systems.

Inertial to CR3BP: This follows a transformation reverse to the one detailed in the previous section. The dimensionalized states are non-dimensionalized, translated with respect to the CR3BP's barycenter and rotated anti-clockwise about the z-axis as demonstrated in Eqs. (8)-(10).

$$\tilde{\mathbf{r}}' = \mathbf{T}_z(\phi)\tilde{\mathbf{R}} \tag{8}$$

$$\mathbf{r} = \mathbf{r}' - \begin{bmatrix}\mu & 0 & 0\end{bmatrix}^T \tag{9}$$

$$\dot{\mathbf{r}} = \mathbf{T}_z(\phi)(\dot{\mathbf{R}} - \boldsymbol{\omega} \times \mathbf{r}') \tag{10}$$

Using these two frame transformations, states can be converted from one CR3BP system to another, provided their primaries lie on the same plane. For example, to transform states from SE CR3BP to SM CR3BP, the process involves two steps: conversion to the heliocentric inertial frame using Eqs. (4)-(6), followed by the transformation from the inertial frame to the SM CR3BP using Eqs. (8)-(10).

Mars-Deimos CR3BP to Sun-Mars CR3BP: Given the inclined orbit of Deimos, an additional intermediate inertial reference frame is necessary to transform states from a MD to an SM CRBP system. The transformation sequence involves converting from MD CR3BP to the M_E frame using Eqs. (4)-(6). This is followed by a series of rotations specified by Eq. (11) to align the intermediate Mars-centered equatorial reference frame with the Mars-centered ecliptic frame. The resulting position is non-dimensionalized, translated to the barycenter of the SM CR3BP reference frame, and then rotated counterclockwise by ϕ_M as depicted in Eq. (12). The corresponding velocity is determined by Eq. (13).

$$\tilde{\mathbf{R}}_{\mathbf{EC}} = \mathbf{T}_z(-\Omega)\mathbf{T}_x(-i)\tilde{\mathbf{R}}_{\mathbf{E}}, \qquad \dot{\tilde{\mathbf{R}}}_{\mathbf{EC}} = \mathbf{T}_z(-\Omega)\mathbf{T}_x(-i)\dot{\tilde{\mathbf{R}}}_{\mathbf{E}} \tag{11}$$

here, $\mathbf{T_x}$ is the rotation matrix about the x-axis.

$$\mathbf{r}_{SM} = \mathbf{T}_z(\phi_M)\mathbf{R}_{\mathbf{EC}} + \begin{bmatrix}1-\mu_{SM} & 0 & 0\end{bmatrix}^T \tag{12}$$

$$\dot{\mathbf{r}}_{SM} = \mathbf{T}_z(\phi_M)(\dot{\mathbf{R}}_{\mathbf{EC}} - \boldsymbol{\omega} \times \mathbf{R}_{\mathbf{EC}}) \tag{13}$$

Sun-Mars CR3BP to Mars-Deimos CR3BP: This follows the reverse of the previous transformation sequence. Initially, the synodic position in the Sun-Mars CR3BP is translated to the Mars centre through Eq. (14). Subsequently, rotation to the inertial Mars-centered ecliptic frame is performed, aligning with M_{EC} using Eq. (15). Finally, the states are transformed from M_{EC} inertial frame to Mars-Deimos CR3BP using Eqs. (8)-(10).

$$\mathbf{r}' = \mathbf{r} - \begin{bmatrix}1-\mu & 0 & 0\end{bmatrix}^T \tag{14}$$

$$\tilde{\mathbf{R}}_{\mathbf{E}} = \mathbf{T}_x(i)\mathbf{T}_z(\Omega)\tilde{\mathbf{R}}_{\mathbf{EC}}, \qquad \dot{\tilde{\mathbf{R}}}_{\mathbf{E}} = \mathbf{T}_x(i)\mathbf{T}_z(\Omega)\dot{\tilde{\mathbf{R}}}_{\mathbf{EC}} \tag{15}$$

Table 2: Initial phase angles for difference systems corresponding to their respective reference axes (X_H for SE and SM, X_E for MD). These values are based on the JPL's online Horizon ephemeris system.[34]

	SE-CR3BP	SM-CR3BP	MD-CR3BP
ϕ_0 [deg]	100.378	359.433	172.321

Solar sail Acceleration

The solar sail model considered for this study is a one-sided ideal solar sail that assumes a pure specular reflection of the incident photons with only a single reflective side.[12] Thus, the acceleration due to the solar radiation pressure (SRP) always acts along the sail's surface normal $\hat{\mathbf{n}}$ away from the Sun. Figure 3 defines the sail-centred sun-sail reference frame $B(\hat{\mathbf{r}}_\mathbf{s}, \hat{\mathbf{q}}, \hat{\mathbf{p}})$, where $\hat{\mathbf{r}}_\mathbf{s}$ is along the sun-sail line. The attitude of the sail is expressed through the cone (α) and clock angle (δ) as seen in Figure 3. The cone angle is the angle between the sail normal and the sun-sail line, while the clock angle is the angle between the projection of the sail's normal on $(\hat{\mathbf{q}}, \hat{\mathbf{p}})$ plane, $\hat{\mathbf{d}}$, and $\hat{\mathbf{p}}$. Hence, the normal vector in the sun-sail frame is given by:

$$\hat{\mathbf{n}}_B = \begin{bmatrix} \cos\alpha & \sin\alpha\sin\delta & \sin\alpha\cos\delta \end{bmatrix}^T \tag{16}$$

As the sail cannot generate acceleration towards the Sun, the cone angle is constrained within the range $[-90, 90]$ deg and the clock angle takes all values within $[0, 180]$ deg. In a CR3BP system, the orientation of the sail can be defined by transforming the normal vector as:

$$\hat{\mathbf{n}} = \begin{bmatrix} \hat{\mathbf{r}}_s & \hat{\mathbf{q}} & \hat{\mathbf{p}} \end{bmatrix} \hat{\mathbf{n}}_B \tag{17}$$

The formulation of the solar-sail acceleration varies depending on whether the Sun is one of the primaries or a fourth-body. For a Sun-Planet (SP) CR3BP system where the Sun is located at $-\mu$ from the barycenter, the acceleration is formulated as:

$$\mathbf{a_s}|_{\mathbf{SP}} = \beta \frac{1-\mu}{r_1^2} (\hat{\mathbf{n}} \cdot \hat{\mathbf{r}}_1)^2 \hat{\mathbf{n}} \tag{18}$$

here $\hat{\mathbf{r}}_\mathbf{s} = \hat{\mathbf{r}}_\mathbf{1}$ (refer Figure 1) and β is lightness number that signifies the percentage of solar gravitational acceleration that is equivalent to the exerted SRP acceleration. For this entire study, the lightness number is assumed to be 0.05, which is considered to be a realistic near-term value.[33]

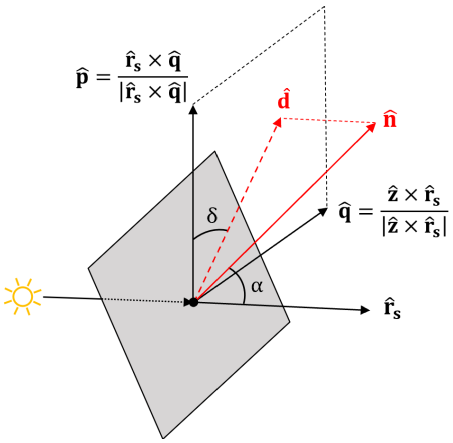

Figure 3: Definition of the sun-sail frame $B(\hat{\mathbf{r}}_\mathbf{s}, \hat{\mathbf{q}}, \hat{\mathbf{p}})$ and the corresponding solar sail attitude angles. Vector $\hat{\mathbf{d}}$ is the projection of the normal vector on the $(\hat{\mathbf{q}}, \hat{\mathbf{p}})$ plane.

However, for a Planet-Moon (PM) CR3BP system the motion of the Sun with respect to its barycenter has to be accounted for, rendering the PM system non-autonomous. This sail acceleration in a PM system is hence expressed as:

$$\mathbf{a_s}|_{\mathbf{PM}} = \beta \frac{G m_{sun}}{r_{3,s}^2} \frac{\tau^2}{\lambda} (\hat{\mathbf{n}} \cdot \hat{\mathbf{r}}_{\mathbf{3,s}})^2 \hat{\mathbf{n}} \tag{19}$$

where G is the universal gravitational constant, m_{sun} is the mass of the Sun, and $\mathbf{r_{3,s}} = \mathbf{r} - \mathbf{s}$ is a vector from the Sun to the sail, with $\mathbf{s}$ being the position vector of the Sun in the PM system. The Sun's position in the PM-CR3BP is computed by transforming its state in the SM CR3BP frame, $[-\mu, 0, 0, 0, 0, 0]^T$, to the MD CR3BP frame.

Fourth-body Perturbation

Two reasons necessitate the inclusion of fourth-body perturbations. Firstly, a study by Kardec and Bertachini[35] showed that the Sun's perturbation in the Mars-Phobos CR3BP system was the largest compared to any other Planet-Moon pairs in the Solar System. This finding indicates that a pure CR3BP approximation may not accurately model transfer trajectories in the similar Mars-Deimos system, necessitating the incorporation of external gravitational perturbations. Building upon that, the specific fourth bodies relevant within the Martian system will be discussed in the subsequent section. Secondly, the transfers in this study are modelled by patching different CR3BP systems, and to maintain consistency in the dynamics during the transitions between systems, fourth-body perturbations are incorporated.[33] Hence, Mars acts as a fourth body while propagating in the Sun-Earth system, and vice versa.

This perturbing acceleration from an external body is computed as:

$$\mathbf{a_4} = \frac{\partial U_4}{\partial r_4} \tag{20}$$

where,

$$U_4 = \mu_4 \left(\frac{1}{r_{3,4}} - \frac{\mathbf{r} \cdot \mathbf{r_4}}{r_4^3} \right) \tag{21}$$

where, $\mathbf{r_4}$ is the position vector from the barycenter to the fourth body, $\mathbf{r}_{3,4}$ is the position vector from the particle (spacecraft) to the fourth body which is given as $\mathbf{r}_{3,4} = \mathbf{r}_4 - \mathbf{r}$, and μ_4 is the dimensionless gravitational parameter of the fourth body with respect to the specified CR3BP system. Equation 20 represents the relative acceleration acting on the sail which not only accounts for the absolute acceleration experienced by the sail solely due to the fourth body but also the fourth-body acceleration acting on the CR3BP system.[36]

The state of the fourth body in the desired CR3BP system can be computed by assuming the perturber to be the second primary in a Sun-perturber CR3BP system. From this, its state, $[1-\mu \quad 0 \quad 0 \quad 0 \quad 0 \quad 0]^T$, can be transformed to the respective CR3BP system using one of the relevant transformations discussed earlier.

J_2 Perturbation

The gravitational field of a non-uniform body can be modelled using a spherical harmonics series, of which the acceleration associated with the oblateness of a body is the dominant term and is called J_2 perturbation. In a CR3BP the acceleration due to the oblateness of the primaries is computed as:

$$\mathbf{a_{J_2}} = \frac{\partial U_{J_2}}{\partial r} \tag{22}$$

where $U_{J_2,1}$ corresponds to potential of smaller primary while $U_{J_2,2}$ for the larger, and they are given as:

$$U_{J_2,1} = -\frac{1}{2} J_{2_1} \frac{1-\mu}{r_1^3} \left(\frac{R_1}{\lambda} \right)^2 \left[3 \left(\frac{z}{r_1} \right)^2 - 1 \right] \tag{23}$$

$$U_{J_2,2} = -\frac{1}{2} J_{2_2} \frac{\mu}{r_2^3} \left(\frac{R_2}{\lambda} \right)^2 \left[3 \left(\frac{z}{r_2} \right)^2 - 1 \right] \tag{24}$$

here, R_1 and R_2 are the radius of the smaller and larger primaries in dimensional units, respectively. Constants J_{2_1} and J_{2_2} are the corresponding harmonic coefficient, values for the bodies under investigation are given in Table 3.

Table 3: J_2 coefficients of different bodies.[34,37,38]

	Mars	Phobos	Deimos
J_2 coefficient	0.0019566	0.1042085	0.107935

Perturbations in the Martian System

In this section, the relevant perturbations are identified for trajectories propagated in the Martian system. The perturbations considered for this analysis include the fourth-body effects due to the Sun, Earth, and Jupiter, perturbations due to the oblateness of Mars, Phobos, and Deimos, and the planetary radiation pressure from Mars, Phobos, and Deimos. A perturbation is regarded relevant if its maximum acceleration is not less than two orders of magnitude lower than the maximum sail acceleration ($\alpha = 0$) for a sail with a lightness number of 0.05 at Mars' distance from the Sun.

Based on Zamaro and Biggs's findings,[39] the planetary radiation pressures are immediately deemed irrelevant given their values being at least three orders lower than the solar-sail acceleration in the position space beyond Phobos' orbit. Among the fourth-body perturbations (a_4), only the gravitational influence due to the

Sun is identified as significant, as illustrated in Figure 4(a). The figure shows the maximum accelerations due to the fourth bodies computed over three years (which accounts for the periodicity of all fourth body perturbations) and plotted along the positive x-axis of the MD CR3BP system. This one-dimensional variation holds for the entire MD position space, as evidenced by the concentric variations in the maximum accelerations seen in the appendix Figure 16 for the Sun and Jupiter.

The perturbation by Mars' J_2 is notably significant at lower altitudes but falls rapidly below the set criteria beyond Deimos's orbit. Nonetheless, given its significance near Deimos, it will be considered in this study. In contrast, the contributions from the J_2 components of the moons, as depicted in Figure 4(b), are negligible at large distances and thus not relevant here.

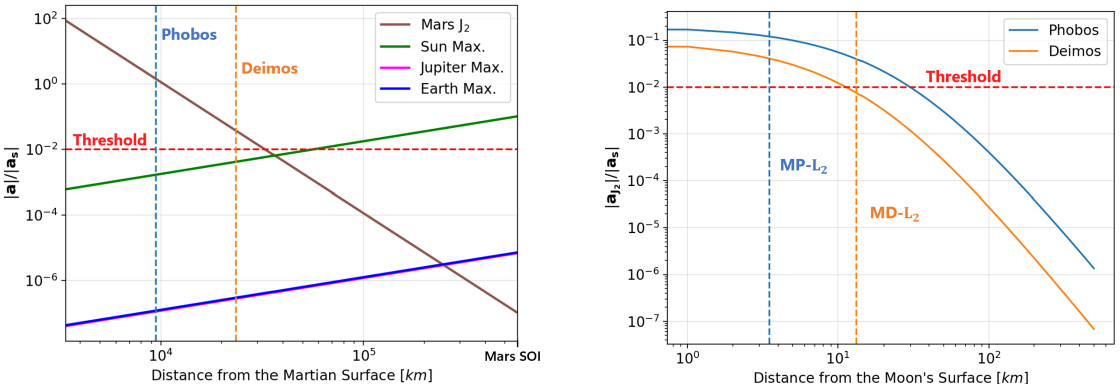

Figure 4: One-dimensional variation of different perturbations normalized against the maximum sail acceleration at that distance. (a) Maximum accelerations of the fourth bodies computed over three years and J_2 perturbation by Mars, calculated in MD CR3BP. Shown along the positive x-axis in the MD frame. (b) Phobos and Deimos J_2 acceleration computed from their surfaces along the positive x-axis in their respective CR3BP frames away from Mars. Vertical Dashed lines indicate their respective L_2 points.

TRANSFER DESIGN FRAMEWORK

The sample return mission consists of two legs: leg 1 (l_1) represents the outbound trajectory, departing from the SE-L_2 point and arriving at the MD-L_1 point, while leg 2 (l_2) represents the inbound return trajectory. Each of these legs is further divided into three phases (p), which model distinct dynamical systems based on the nearby gravitational bodies: Sun-Earth, Sun-Mars, and Mars-Deimos CR3BP.

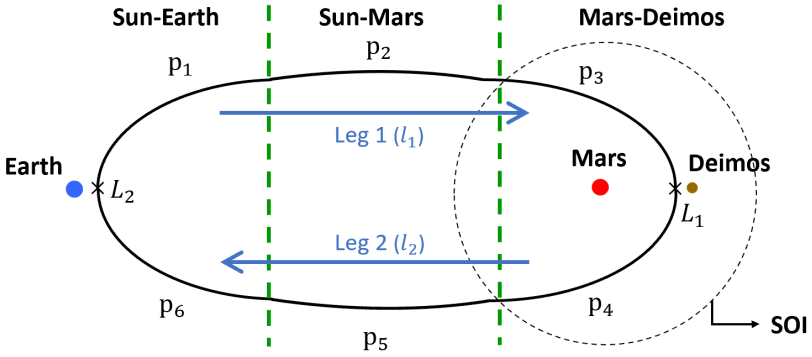

Figure 5: Definition of mission phases and legs.

The objective of the transfer design is to find solar sail trajectories that minimize the transfer duration of

the spacecraft, thereby maximizing the stay time near the Martian moon (at the MD-L_1 point) and enhancing scientific output within a given mission timeframe. The minimum feasible total mission duration will be decided based on the results obtained in the following section. This ensures that, along with increasing the potential scientific output by maximizing the stay duration, the operational costs of the mission are kept in check by limiting the total mission duration. This study adopts a launch period of 2030-2032, following the return of samples from MMX in 2029.[10]

To achieve the desired objective, an optimal control problem will be solved by employing a direct method to find the optimal sail control law (cone and clock angles), and the corresponding departure and arrival epochs. Prior to this, given the direct methods' dependence on an initial guess, first-guess sub-optimal trajectories will be found using the Monte Carlo method and Differential Evolution algorithm.

INITIAL GUESS

As stated earlier, initial guesses are generated using a patched CR3BP approach. This involves connecting solar-sail perturbed stable and unstable manifolds from the Lagrange points of the Sun-Earth and Mars-Deimos systems. In the classical case, i.e. when the sail acceleration is not considered, a stable manifold is a ballistic trajectory that approaches the equilibrium point while an unstable manifold moves away from the point. These one-dimensional manifolds associated with the Lagrange points are computed by integrating an initial state that is slightly perturbed in the direction of the unstable or stable eigenvector. This initial perturbed state is:

$$\mathbf{x}_{0,s} = \mathbf{x} \pm \epsilon \mathbf{v}_s, \qquad \mathbf{x}_{0,u} = \mathbf{x} \pm \epsilon \mathbf{v}_u \tag{25}$$

where $\mathbf{x}_{0,s}$ and $\mathbf{x}_{0,u}$ are the initial perturbed state associated with the stable and unstable manifolds for the eigenvectors $\mathbf{v}_s$ and $\mathbf{v}_u$, respectively. The small perturbation, denoted by ϵ, is taken as 10^{-4}. The signs ($\pm$) in the Eq. (25) depict the interior or exterior branches of the manifold; for the given application, the signs associated with the exterior branches are chosen.

For the first leg, a solar-sail perturbed unstable manifold is propagated forward in time from SE-L_2, while a stable manifold from MD-L_1 is propagated backwards. Once the trajectory from Deimos reaches the Martian sphere of influence (SOI) (refer Figure 5), states are transformed to the Sun-Mars CR3BP frame and continued to be integrated backwards. On the contrary, the second leg involves forward propagation in the MD and SM systems, with simultaneous backward propagation in the SE system. Note that the trajectories passing between the MD and SM frames are continuous with no state discontinuities.

The initial guesses assume that the sail attitude remains constant in the SE and SM systems. However, a locally optimal tangential control law for the sail is implemented for the trajectories in the MD systems (phases 3 and 4). This is because, unlike the Earth-Moon system where past studies assumed a constant sail attitude,[31,40] owing to the low mass and proximity of the moons to Mars, a fixed sail attitude proves inadequate for generating trajectories capable of manipulating energy to reach the Martian SOI. Hence, when shifting from the Mars-Deimos phase to the Sun-Mars phase, the control law is switched from a tangential control to a fixed attitude control (or vice-versa).

Based on Eq. (26), a tangential control law produces low time-of-flight trajectories by maximizing the rate of change in the Jacobi constant by directing thrust either along or against the instantaneous velocity vector in the synodic frame.[41]

$$\dot{JC} = -2\mathbf{a_s} \cdot \mathbf{v_{SM}} \tag{26}$$

In Eq. (26), $\mathbf{v}_{SM}$ is the instantaneous velocity vector of the spacecraft in the Sun-Mars CR3BP. For a Mars escape trajectory, the thrust acts along the velocity vector, maximizing energy. In contrast, for a capture trajectory spiralling inwards to the Lagrange points of the MD system, thrust acts opposite the velocity vector, minimizing energy. However, since trajectories within the Martian SOI are propagated in the MD system, and the rate of change of JC is maximised/minimised in the SM system, the velocity vector in the SM system must be represented in the MD system. This transformation is achieved using Eq. (27).

$$\mathbf{v_{SM}}|_{\mathbf{MD}} = \begin{bmatrix} \dot{x} \\ \dot{y} \\ \dot{z} \end{bmatrix}_{MD} + \begin{bmatrix} -y + y\frac{\tau_{MD}}{\tau_{SD}} \\ x + \mu + (x+\mu)\frac{\tau_{MD}}{\tau_{SD}} \\ 0 \end{bmatrix}_{MD} \tag{27}$$

Given that a solar sail is constrained by its inability to produce acceleration facing the Sun, the sail normal cannot always point in the desired direction. Nonetheless, the sail acceleration acting along it can be maximized using Eqs. (28) and (29), adapted from the locally optimal steering laws introduced by McInnes.[12]

$$\alpha^* = \frac{1}{2}\left[\alpha_l - \sin^{-1}\left(\frac{\sin\alpha_l}{3}\right)\right] \tag{28}$$

$$\delta^* = \delta_l \tag{29}$$

where α^* and δ^* are the locally optimal attitude angles, and α_l and δ_l are the attitude angles of primer vector $\hat{\mathbf{l}}$, i.e. the reference direction ($\pm\mathbf{v_{SM}}|_{\mathbf{MD}}$ here) for desired acceleration, as shown in Figure 6. The figure shows a sail acceleration bubble plotted in the plane ($\hat{\mathbf{r}}_s$, $\hat{\mathbf{d}}$) (see Figure 3), representing the maximum attainable acceleration by a solar sail corresponding to a certain cone angle, and the optimal sail normal ($\mathbf{n}^*$) that maximizes the sail acceleration along the desired reference direction ($\hat{\mathbf{l}}$). Note that the primer vector is not subject to any constraints regarding the attitude angles it can take.

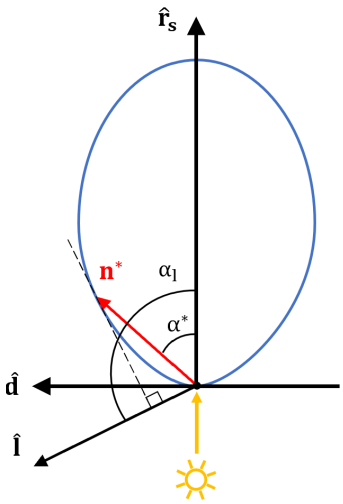

Figure 6: Ideal solar sail acceleration bubble in the ($\hat{\mathbf{r}}_s$, $\hat{\mathbf{d}}$) plane.

Additionally, note that this locally optimal steering is not immediately implemented when propagating the sail-perturbed manifolds near the moons. Instead, a brief 0.25 day ballistic segment (classical manifold) is included in the moon's vicinity. This addresses trajectories that might otherwise impact the moon immediately, depending on the Sun's relative position in the MD CR3BP. The selected duration ensures that the spacecraft reaches an adequate distance from the moon before initiating powered flight, and was determined through a grid search over different epochs for a single Martian year.

Design Approach

Alongside assuming a constant and locally optimal steering law, initial guesses are generated by also neglecting certain perturbations. Additionally, minor discontinuities in position (Δr) and velocity (Δv) between the forwards and backwards propagated trajectories are permitted, as long as they remain feasible enough for the direct method to solve. Feasibility in this context is considered if $\Delta r \leq 10^{-3}$ (1.5e5 km) and $\Delta v \leq 10^{-2}$ (0.30 km/s) in the Sun-Earth CR3BP frame.[31] Thus, yielding a sub-optimal solution for each individual leg. The design variable $\mathbf{D}$ for this optimization problem is:

$$\mathbf{D} = \begin{bmatrix} t_{dep} & t_{arr} & t_{link} & \alpha_{us} & \delta_{us} & \alpha_s & \delta_s \end{bmatrix}^T \tag{30}$$

Here, t_{dep} and t_{arr} represent the departure and arrival epochs of a leg, respectively, in SE dimensionless time unit. The variable t_{link} is the linkage time fraction, defined as the ratio of the forward propagated trajectory's ToF in the interplanetary phase (phase 1 for leg 1 and phase 5 for leg 2) to the total ToF of the interplanetary phase, i.e. between the SE-L_2 point and the Martian SOI. The variables $(\alpha_{us}, \delta_{us})$ and (α_s, δ_s) are the constant sail attitude angles associated with the unstable and stable manifolds, respectively. Note that while the trajectory when switching between the MD and SM phases remains continuous in state, the control may not be continuous.

The first step is to perform a Monte Carlo (MC) analysis for each leg to explore the design space while evaluating the ToF, Δr and Δv as objectives. The insights of this are then used to perform a more refined search using the differential evolution (DE) algorithm. Except for the departure epoch, arrival epoch and

cone angles, the bounds for the design parameters are the same for both legs. The departure epoch always spans one Earth-Mars synodic period while the arrival epoch is computed based on the possible maximum and minimum ToF inferred from literature. The bounds for cone angle for the outbound trajectory is $[0, 90]$ deg and for the inbound leg is $[-90, 0]$ deg.

The following is an example of the first leg of the mission: departure epoch (t_{dep}) spans one Earth-Mars synodic period from Jan 01, 2030, 12:00 noon. The arrival epoch t_{arr} ranges between Nov 01, 2032 and Nov 01, 2036. This is determined by considering both the maximum (1400 days) and minimum (900 days) ToF achievable for a solar sail to travel between Earth and Mars based on past literature,[31–33] and an analytical estimate, Eq. (31), for the ToF of locally-optimal solar-sail escape trajectories from a planetocentric system, adapted from McInnes,[12] which for Deimos is 261 days. Next, the linkage fraction t_{link} is considered to vary between 0.1 and 0.9. Finally, the cone angles α_{us} and α_s fall within $[0, 90]$ deg, while the clock angles δ_{us} and δ_s within $[0, 180]$ deg.

$$ToF_{esc} = \frac{\lambda_{SM}^2 \sqrt{G m_{mars}}}{0.4393\beta \cdot \lambda_{MD}^{0.5} \cdot G m_{sun}} \tag{31}$$

In Eq. (31), m_{sun} and m_{mars} denote the masses of the Sun and Mars, respectively.

Monte Carlo Analysis

The Monte Carlo analysis is performed assuming no perturbations (fourth-body and Mars J_2) in all three phases. The analysis found no clear correlation between the state error at linkages, ToF, and cone and clock angles. This is attributed to the fact that the attitude angles required to obtain a feasible trajectory depend on the arrival and departure epochs and thus will have the same bounds moving forward. However, the bounds for the linkage fraction (t_{link}) are narrowed to [0.2, 0.8] as this ensures that trajectories in the Sun-Mars phase (p_2 and p_5) move sufficiently away from Mars, avoiding flybys and impacts with Mars. Nonetheless, much like the attitude angles, the linkage fraction lacks a strong correlation with the objectives.

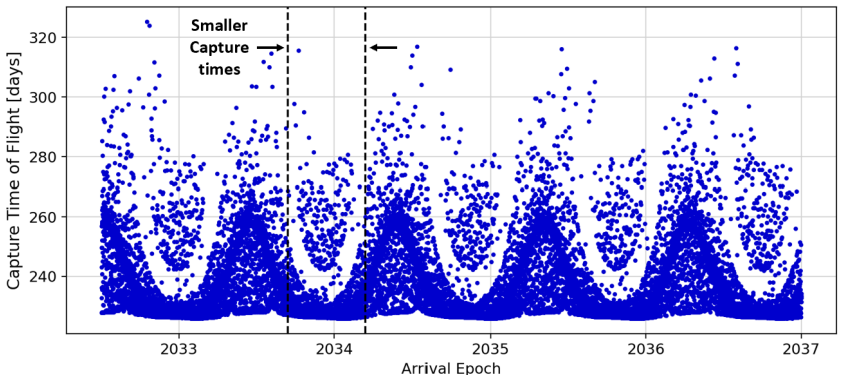

Figure 7: Time of flight to spiral towards the Mars-Deimos L_1 point plotted against the arrival epoch at L_1. Vertical dotted lines encapsulate one of the regions with smaller capture times.

The departure and arrival epochs, on the contrary, exhibit a strong correlation with the linkage position and velocity errors. Additionally, it is also observed that the time of flight for both the capture trajectory to the moon and the escape trajectory to the Martian SOI follow a periodic trend that repeats every half Martian year (roughly 0.94 years), as depicted in Figure 7 for the first leg. Here a minimum ToF of roughly 225 days is attainable, and the same was observed for the second leg as well. This periodicity is attributed to the relative position of Deimos at arrival/departure, specifically the orientation of Deimos' orbit in the Sun-Mars frame. For certain orientations of the orbit, the level of sail acceleration is maximum along the trajectory. When viewed in the Sun-Mars frame, the ascending node of Deimos' orbit in the SM frame "precesses" with time, shown in Figure 8, and a given orientation of the orbit repeats itself every half a Martian year. Additionally,

it was also observed that all the trajectories, as expected, escape the SOI from the anti-Sun direction given the sail's inherent inability to point towards the Sun.

Figure 9 illustrates regions where position errors below $2 \cdot 10^7$ km and velocity errors below 1 km/s are achievable for the first leg of the mission to Deimos, for various arrival and departure epochs. The feasible region, confined by the inclined dashed red line, aligns with the minimum ToF estimate made from the literature. White scatters mark points with the lowest Δr and Δv in the solution set, while green crosses denote epochs where the spacecraft impacts Deimos post-departure, and considering the moon's short orbital period (1.2 days), no specific trend is observed for these impacts. The vertical black dotted line corresponds to the region from Figure 7, where, for given arrival epochs, the spiral times of the trajectories are minimum. The region enclosed within this (shaded in grey in Figure 9) is the refined search space for DE, providing not only feasible solutions with potential minima but also shorter ToFs.

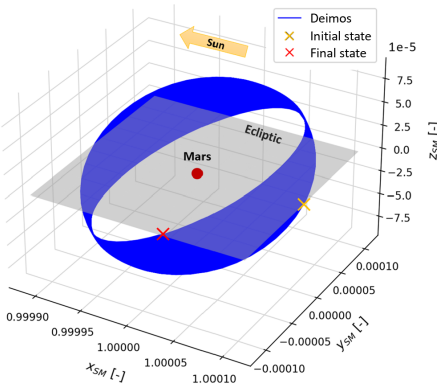

Figure 8: Orbit of Deimos plotted over a period of four months in a Sun-Mars CR3BP system.

Figure 10 presents a similar plot for the second leg. Given the chosen DE region for leg 1, a minimum total mission time of seven years appears to fall within the infeasible region of Figure 10, where linkages between the manifolds cannot be found. Therefore, henceforth, a maximum mission timeframe of eight years will be considered, potentially allowing for a maximum one-year stay near Deimos. Finally, the epoch bounds for DE of leg 2 will be determined by DE-optimized solutions of leg 1 and Figure 10. The leg 2 departure epoch will extend from the arrival epoch of the DE-optimized leg 1 solution to the maximum permissible departure epoch for leg 2 as per Figure 10, i.e. 2035.50. The leg 2 arrival epoch will be constrained by the minimum permissible arrival epoch from Figure 10 and the DE-optimized departure epoch of leg 1 plus eight years. Note that, unlike for leg 1, these epoch bounds are not constrained by the smaller escape ToF limits.

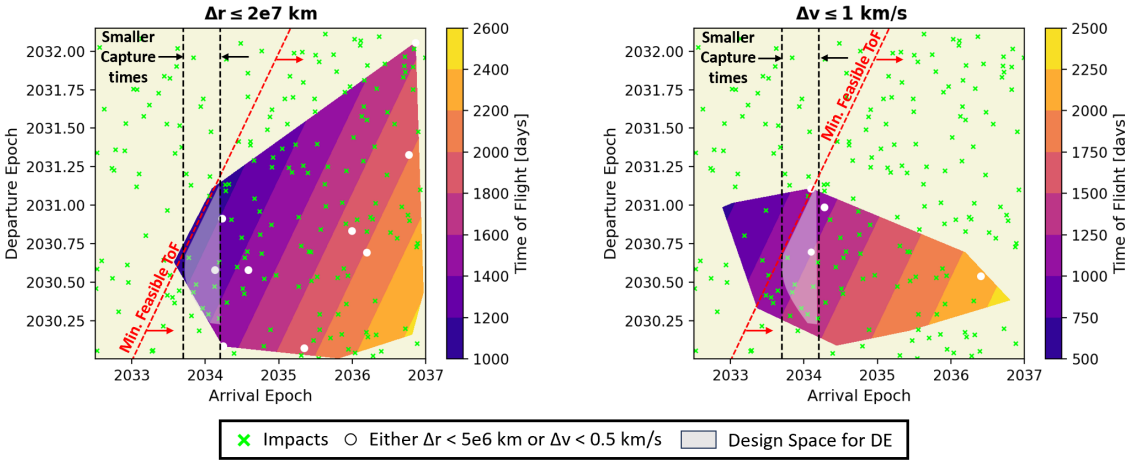

Figure 9: ToF contours for regions with $\Delta r \leq 2 \cdot 10^7$ km (left) and regions with $\Delta v \leq 1$ km/s (right). Plotted for the first leg (outbound trajectory) of a Deimos sample return mission. The transparent grey area is the overlap of the feasible region in both Δr and Δv plots and acts as the restricted design space for the differential evolution.

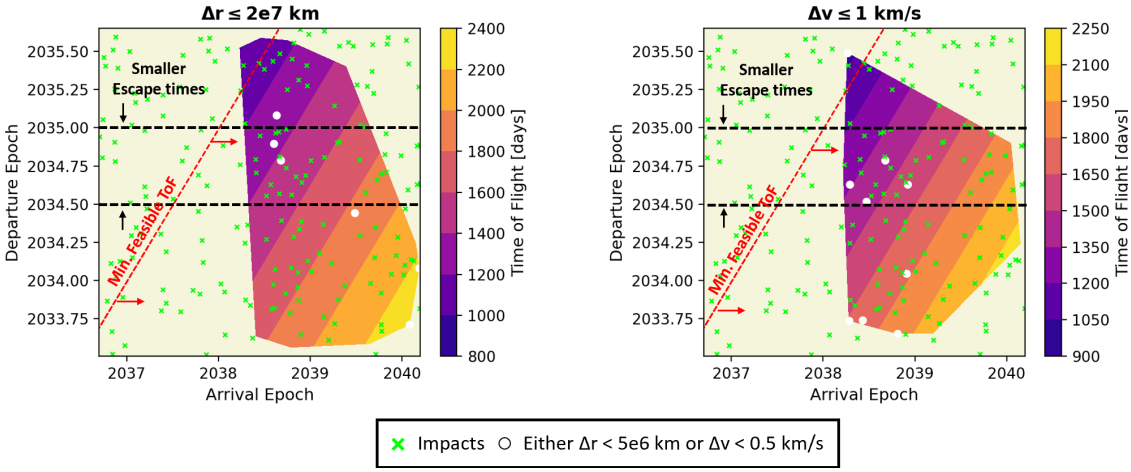

Figure 10: ToF contours for regions with $\Delta r \leq 2 \cdot 10^7$ km (left) and regions with $\Delta v \leq 1$ km/s (right). Plotted for the second leg (inbound) of a Deimos sample return mission.

Differential Evolution

While the MC analysis provides insights into the design space, it falls short in generating results that satisfy the $\Delta r \leq 10^{-3}$ and $\Delta v \leq 10^{-2}$ requirements given the highly non-convex nature of the design space. Achieving feasible designs would demand a larger number of samples, leading to increased computational effort. To address this, differential evolution is applied with the same design variable $\mathbf{D}$ (Eq. (30)), building upon insights gained from the MC analysis. DE focuses on a narrowed search space, as outlined in the previous section, for each leg of the mission separately. Additionally, for DE, the spiral trajectories in the MD system are propagated considering the Sun's gravity and Mars' J_2 effect.

For leg 1, accounting for the minimization of the state error at the linkages and the time of flight, the fitness function formulated is given by Eq. (32).

$$J_{l_1} = k(\Delta r_{l_1} + w_1 \Delta v_{l_1}) + w_2(t_{arr,l_1} - t_{dep,l_1}) + g_1 + g_2 \tag{32}$$

Here, Δr_{l_1} and Δv_{l_1} denote the position (in km) and velocity (in km/s) errors at the linkage, respectively. To address their magnitude difference, the weight w_1 scales the velocity error. The term $(t_{arr,l_1} - t_{dep,l_1})$ represents the time of flight (in days) for the first leg, with w_2 as the corresponding weight. The binary variable k ensures that once the minimum requirement for linkage state errors is met, the focus shifts to further minimizing the ToF, as defined in Eq. (33). Additionally, g_1 and g_2 serve as penalty functions. Due to the problem's complexity, g_1 penalizes fitness values deviating from the set requirements (Eq. (34)). Meanwhile, g_2 is a death penalty, set to 10^{20}, penalizing the objective for trajectories that impact either Deimos or Mars.

$$k = \begin{cases} 1 & \text{if } \Delta r_{l_1/l_2} > 1.5 \cdot 10^5 \text{ km and } \Delta v_{l_1/l_2} > 0.3 \text{ km/s} \\ 0 & \text{if } \Delta r_{l_1/l_2} \leq 1.5 \cdot 10^5 \text{ km and } \Delta v_{l_1/l_2} \leq 0.3 \text{ km/s} \end{cases} \tag{33}$$

$$g_1 = 100 \cdot max(0, (\Delta r_{l_1/l_2} + w_1 \Delta v_{l_1/l_2}) - 10^6) \tag{34}$$

For leg 2, the objective function, Eq. (35), is formulated similarly, with the only difference being the second term $(t_{arr,l_1} - t_{dep,l_2})$. The minimization of this term increases the stay time near the moons for the arrival epoch obtained by optimizing Eq. (32).

$$J_{l_2} = k(\Delta r_{l_2} + w_3 \Delta v_{l_2}) + w_4(t_{arr,l_1} - t_{dep,l_2}) + g_1 + g_2 \tag{35}$$

Note that, because the arrival epoch bounds of leg 2 depend on the departure epoch of leg 1 and the eight-year mission time constraint, the escape spiral from MD-L_1, unlike the capture spiral trajectory of leg 1 that considers a restricted design space (Figure 9), might not result in minimum spiral time.

Following the tuning of the DE algorithm, the initial guesses obtained for both legs are listed in Table 4.

Table 4: Initial guesses obtained from differential evolution.

	Leg 1	Leg 2
Δr [km]	$1.59{\cdot}10^4$	$1.21{\cdot}10^5$
Δv [km/s]	0.12	0.28
t_{dep}	Aug 12, 2030	Nov 20, 2034
t_{arr}	Mar 16, 2034	Aug 08, 2038
α_{us} [deg]	54.42	-40.28
δ_{us} [deg]	79.29	75.27
α_s [deg]	23.20	-14.66
δ_s [deg]	100.29	68.66
Stay time [days]	249	

OPTIMAL CONTROL PROBLEM

To tackle the infinite-dimensional low-thrust optimization problem, this study employs a direct pseudospectral method as the optimal control algorithm. The primary objective is to maximize the duration of stay in the vicinity of the moon. While the ideal scenario to achieve this objective involves simultaneously solving both legs of the sample-return mission (as depicted in Figure 5), the trajectories in phases 3 and 4, involving numerous revolutions, are not considered in the optimisation due to computational limitations encountered while employing the direct pseudospectral method. As a result, only the sub-optimal tangential steering law is considered for these phases, and both the legs are solved separately. Nevertheless, it is worth noting that existing literature suggests that the locally optimal steering law for the escape/capture trajectories provides solutions that align very closely to the optimal solutions found using the optimal control theory.[12,42]

Problem Definition

The optimization of both legs is performed separately while being partially dependent on each other. First, phases 1 and 2 of leg 1 are solved for minimum transfer time, utilizing the initial guess generated in the previous section but also incorporating fourth-body perturbations. The objective function is defined by Eq. (36):

$$J = t_f - t_0 \tag{36}$$

where for leg 1, t_0 is the epoch of departure from the SE-L_2 point and t_f is the epoch at the Martian SOI.

The states ($\mathbf{x}$), defined in the respective CR3BP system, and control ($\mathbf{u}$) associated with the OCP considered are:

$$\mathbf{x} = \begin{bmatrix} x & y & z & \dot{x} & \dot{y} & \dot{z} \end{bmatrix}^T \tag{37}$$

$$\mathbf{u} = \begin{bmatrix} \alpha & \delta \end{bmatrix}^T \tag{38}$$

here the bounds for the control are $\alpha \in [-90, 90]$ deg and $\delta \in [0, 90]$ deg, taking the full range of feasible values for the control angles, unlike during the initial guess generation, giving the optimizer more flexibility.

Furthermore, the trajectory is subject to boundary constraints, ensuring its departure from the SE-L_2 point and arrival at the Martian SOI with states and controls equal to the final state and control of the backward-propagated initial guess trajectory from phase 3, represented in the Sun-Mars frame. These constraints are expressed through Eqs. (39) and (40).

$$\mathbf{x_{0_{l_1,p_1}}} = \mathbf{x_{SE-L_2}} \tag{39}$$

$$\mathbf{x_{f_{l_1,p_2}}} = \mathbf{x_{0_{ig,p_3}}}, \qquad \mathbf{u_{f_{l_1,p_2}}} = \mathbf{u_{0_{ig,p_3}}} \tag{40}$$

where the subscripts l_i, p_i and ig refer to the leg number, phase number, and initial guess, respectively. The symbols 0 and f correspond to the initial and final values of the variable for the denoted phase.

Since both phases 1 and 2 are solved in different CR3BP frames, linkage constraints on states, controls and time are applied to ensure a continuous trajectory as follows:

$$\mathbf{x_{f_{l_1,p_1}}} = \mathbf{x_{0_{l_1,p_2}}}, \qquad \mathbf{u_{f_{l_1,p_1}}} = \mathbf{u_{0_{l_1,p_2}}}, \qquad t_{f_{l_1,p_1}} = t_{0_{l_1,p_2}} \tag{41}$$

In this formulation, the state constraints are defined in the Sun-Earth frame, requiring the states of SM CR3BP to be transformed to the SE frame at linkage. Since the control is defined in a sun-sail frame, it need not undergo any transformation.

Given that the arrival time of phase 2 at the Martian SOI is constrained by the initial guess, the sole variable in the objective function (Eq. (36)) is the departure epoch. It is thus the departure epoch that is optimized to minimize the total ToF of the first leg, up to the SOI. The trajectory beyond this point (i.e., for phase 3, involving the spiral into the Martian system) has already been generated as part of the initial guess.

Recall that the maximum bound for the arrival epoch of leg 2 is determined by the leg 1 departure epoch plus eight years. Therefore, the newly optimized departure epoch of leg 1 is utilized to calculate the maximum arrival epoch for the return leg based on the maximum eight-year mission timeline. Subsequently, a new initial guess is generated for the return trajectory by employing the already-tuned DE algorithm. The updated maximum limit on the arrival epoch of leg 2 is expected to surpass that obtained from the departure epoch of the initial guess of leg 1. Consequently, the new estimate from DE for the return leg is anticipated to increase the duration of stay at Deimos further.

The new initial guess for the return trajectory is then subjected to the same optimal control problem (OCP) described in Eqs. (36)-(41), but for phases 5 and 6. In these phases, the arrival epoch at SE-L_2 serves as the free variable, while the departure epoch from MD-L_1 is constrained at the SOI based on the spiral escape trajectory generated using DE.

OCP Solver

PSOPT,[43] a C++-based open-source software package, is used to implement the direct pseudospectral method for the local optimization of the initial guess. This method discretizes the continuous control and state variables on a finite time grid, reducing an infinite-dimensional optimal control problem to a finite-dimensional parameter optimization problem that is solved as a non-linear programming problem (NLP). This study uses the Legendre pseudospectral method, which approximates the states and controls using Legendre polynomials at Legendre-Gauss-Lobatto nodes that serve as the finite time grid. The NLP solver used is IPOPT.

The motivation to opt for a pseudospectral method for the OCP is threefold. Firstly, pseudospectral methods provide high convergence rates and enable accurate solutions even with relatively coarse grids.[44] Secondly, numerous studies, such as those by Heiligers et al.,[33] Vergaaij et al.,[31] and Bakx et al.,[45] have successfully employed pseudospectral methods for their OCPs with similar dynamics. Lastly, its accessibility through an open-source software makes it a convenient choice. Additionally, given that the OCP under consideration involves multiple phases, nonlinear path constraints, bounds on state and control variables, free initial and final conditions, as well as linkage constraints - all of which align with the capabilities of PSOPT - it is the preferred tool for this study.

Results

The time-optimal interplanetary trajectory for leg 1, generated by PSOPT, is presented in Figure 11(a), plotted in the heliocentric inertial frame. Additionally, Figure 11(b) illustrates the capture trajectory that employs the locally optimal steering within the Martian SOI, and is plotted in the SM CR3BP frame. The

control profile for these trajectories is given in Figure 12. The solution obtained from PSOPT clearly satisfies the linkage and boundary constraints as seen in these figures, and produces a result that has a time-of-flight shorter than its initial guess as evident from Figure 12.

Looking at the control profile (Figure 12) and thrust vectors (Figure 11(a)) for the interplanetary phases, it can be observed that the optimal result consists of a significant non-planar thrust segment in the second phase. This steadily changes the inclination of the trajectory to rendezvous with the end state at the SOI.

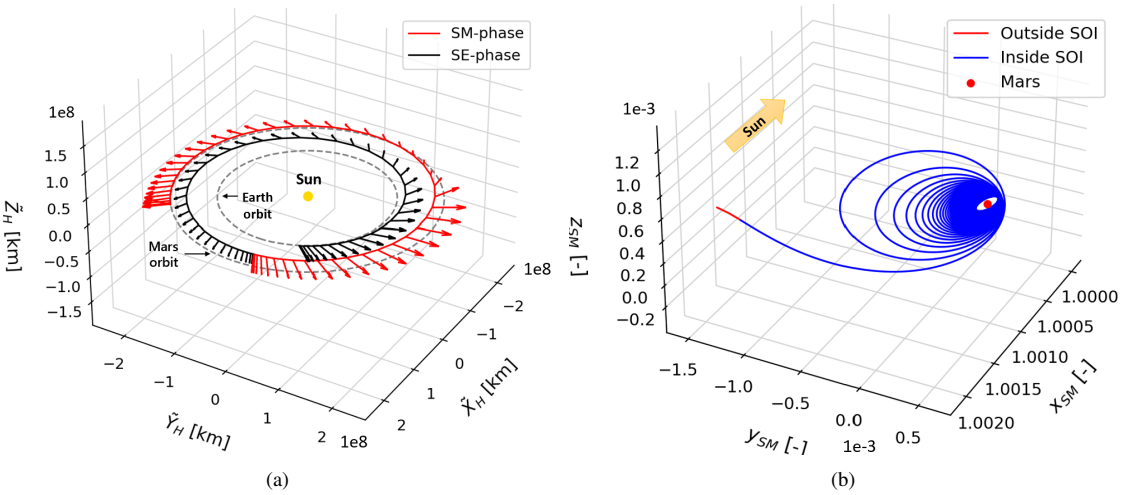

Figure 11: Trajectories for leg 1 of the mission. (a) Interplanetary transfer shown in the heliocentric inertial frame. (b) Capture trajectory shown in the Sun-Mars CR3BP frame

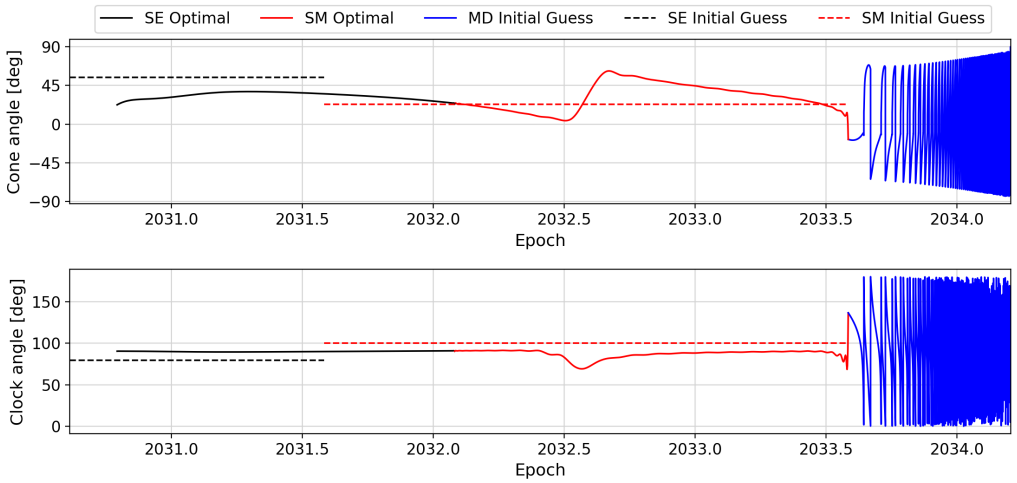

Figure 12: Control profile for the outbound trajectory to Mars-Deimos L_1 point. The solid lines are the outputs from PSOPT, while the dashed lines are the initial guesses obtained through differential evolution.

In phase 3, the locally optimally steering law gradually reduces the inclination of the orbit, to the SM plane (ecliptic), until it reaches MD-L_1, as observed in Figure 11(b). This also explains the gradual increase in the maximum and minimum cone angles for the spiral capture trajectory depicted in Figure 12. Because this phase was computed by propagating backwards in time, a more intuitive understanding of this control profile can be gained by reversing the time perspective. Recall that the locally optimal steering law does not target

a specific end state; rather, it only aims to maximize the rate of change of the Jacobi constant (Eq. (26)) at any given time. When propagating backwards from MD-L_1, given its initial inclination of 26 deg in the SM frame, the velocity vector, optimal normal vector, and Sun-sail vector typically do not lie in the same plane. This introduces an additional non-planar thrust component (to the orbital plane), causing a change in inclination. As the orbit becomes more inclined (backwards in time), the velocity and Sun-sail line orient less in either the maximum acceleration orientation ($\alpha = 0$ deg) or minimum acceleration orientation ($\alpha = \pm 90$ deg). This behaviour is further illustrated in the zoomed-in image of the phase 3 control (Figure 13), where orbits with higher inclination exhibit no data points at 0 deg cone angle. This observation aligns with the findings by Macdonald and McInnes,[46] where higher-inclined orbits led to lower Earth escape times due to a greater non-planar sail acceleration.

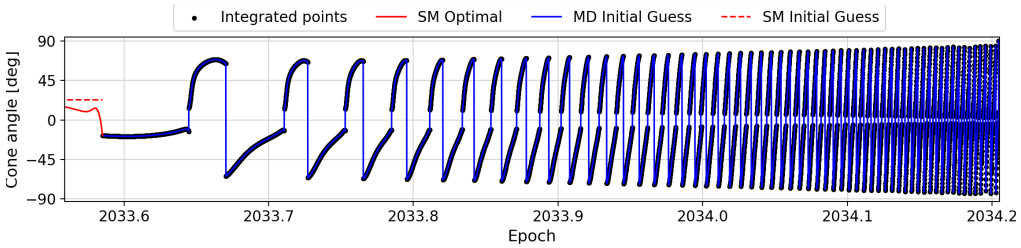

Figure 13: Zoomed-in image of the phase 3 control profile generated using the locally optimal steering law. The black dots represent the points at which integration is performed.

For leg 2, as mentioned earlier, using the time-optimal result for leg 1 the initial guess for leg 2 is regenerated. This guess exhibits a linkage position and velocity error of $1.99 \cdot 10^3$ km and 0.13 km/s, respectively, with fixed control angles and epochs that are shown as part of Figure 14. As expected, the new optimal departure epoch from SE-L_2 increases the duration of stay at Deimos to 329 days, given a maximum mission duration of eight years. This is 80 days longer than that obtained from the leg 1 initial guess (see Table 4).

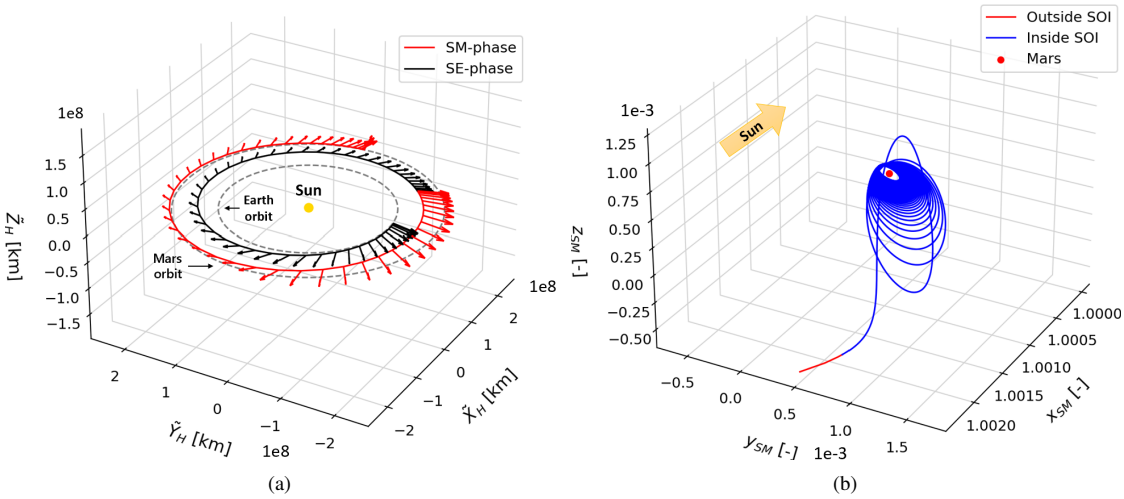

Figure 14: Trajectories for leg 2 of the mission. (a) Interplanetary phases shown in the heliocentric inertial frame. (b) Escape trajectory shown in the Sun-Mars CR3BP frame

Similar to leg 1, Figures 14(a), 14(b), and 15 show the interplanetary trajectory, escape trajectory, and control profile for the inbound leg 2, respectively. The interplanetary control profile is similar to that of leg 1, with only attitude angles adjusted for an inward spiral to Earth. However, the phase 4 control for the escape is rather intriguing. In contrast to phase 3, the maximum and minimum cone angles increase over time until they approach their maximum bounds of $[-90, 90]$ deg, accompanied by clock angles close to 90 deg. This is

followed by a decrease in the maximum bounds of cone angles that the locally optimal algorithm generates. This occurs because the non-planar sail force not only alters the inclination but also the right ascension of ascending node of the orbit when viewed in the SM frame (similar to Figure 8). This leads to a certain orbital orientation where the sun-sail vector is nearly parallel to the velocity along the orbital plane, closely approaching the maximum and minimum acceleration orientations.

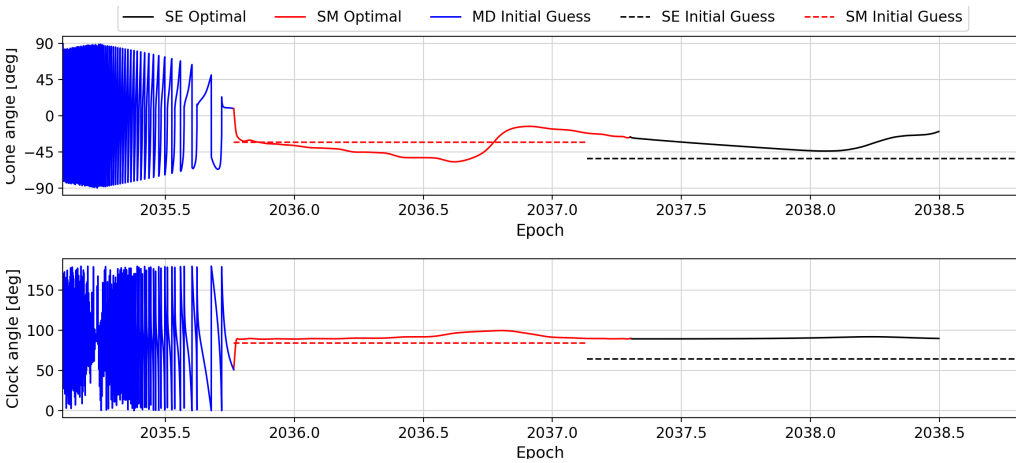

Figure 15: Control profile for the inbound trajectory departing from Mar-Deimos L_1 point. The solid lines are the outputs from PSOPT, while the dashed lines are the initial guesses obtained through differential evolution.

Since the direct pseudospectral method produces optimal control and states only at discrete points in time, the validity of the solution in a continuous time horizon is checked through reintegration. The discrete control obtained from PSOPT is interpolated and used to reintegrate the states of the interplanetary phases for legs 1 and 2 from their respective initial to final states. Reintegrated results for leg 1 show errors of 25,845.82 km in position and 0.00103 km/s in velocity at its end state near the Mars SOI. For leg 2, the errors are 45,829.28 km in position and 0.0019 km/s in velocity. These errors are considered sufficiently low and can be corrected through manoeuvres along the trajectory.

Table 5: Time-optimal results obtained using PSOPT

	Leg 1	Leg 2
Departure epoch	Oct. 17, 2030	Feb. 07, 2035
Arrival epoch	Mar. 16, 2034	July 01, 2038
Heliocentric transfer time [days]	1019.72	998.08
Spiral time [days]	226.55	241.72
Stay duration [days]	329	

Table 5 summarizes the resultant epochs and ToF for different phases of the final time-optimal trajectories. Compared to previous studies which employ the same dynamical model and a lightness number of 0.05 for an ideal sail, the ToF for the Earth-to-Mars transfer (or vice versa) obtained using PSOPT in the present study is up to 10% longer. Vergaaij and Heiligers[32] reported transfer times from SE-L_2 to Mars pole sitters around 952 or 992 days, depending on the type of pole sitter. Similarly, in Ref. 31 and 33 transfers between the Halo orbits of SE-L_2 and SM-L_1 were found to have ToFs roughly in the range of 910-930 days. The longer transfer times seen here can be attributed to the different arrival/departure states (to or from Mars SOI) compared to those in the literature and the fact that the optimizer has the freedom to only vary the epoch at SE-L_2, not the arrival/departure epoch at the SOI. This introduces an additional constraint to the OCP compared to the previous studies. Further, on comparing the results obtained for the near-term sail with those using a realistic model for electric propulsion, the transfer times obtained here are substantially large - the fuel optimal solutions computed by Park[29] had a ToF of 500 days and 27.75 days for the interplanetary and Martian phases, respectively.

The approach to trajectory design using heteroclinic-like connections does indeed find valid trajectories to and from Deimos using a solar sail; however, it is hampered by its computational limitations. While generating the interplanetary trajectory is not computationally expensive, the trajectory within the Martian SOI proves challenging due to Deimos's low mass and proximity to Mars. This renders the consideration of a three-body problem ineffective, as trajectories exhibit behaviour similar to a two-body approximation.

Here, a mission to Deimos involves about 60 revolutions around Mars, which computationally was manageable; but a mission to Phobos, which is closer to Mars, requires 400 revolutions, resulting in computational times nine times that to Deimos. Hence, a more computationally efficient approach is necessary. While a different approach might expedite convergence to a better solution, the lack of constraints on the maximum feasible steering rate and the sail's steering capability during the escape or capture trajectory - where the sail must reorient by 180 deg per orbit, taking all angles between $[-90, 90]$ deg (Figure 13) - will continue to limit the practicality of the optimal trajectory obtained.[12,33,47]

CONCLUSION

In this paper, transfers using solar sails have been designed for a sample-return mission from the Martian moon Deimos. The departure and arrival locations near Earth and Deimos are considered to be the Sun-Earth L_2 and Mars-Deimos L_1 Lagrange points, respectively. The trajectory design aims to maximize operational time near Deimos by minimizing the time of flights (ToFs) for transfers between these two Lagrange points, within a minimum feasible total mission duration. The corresponding optimal control problem is solved using a direct pseudospectral method, implemented with PSOPT. This method depends on a sufficiently accurate initial guess, which is obtained through a patched circular restricted three-body problem (CR3BP) approach. In this approach, heteroclinic-like connections between the Lagrange points of different CR3BP systems are sought by employing Monte Carlo and differential evolution methods. The entire trajectory framework involves three CR3BP systems: Sun-Earth (SE), Sun-Mars (SM), and Mars-Deimos (MD). Furthermore, additional relevant perturbations have been identified for each system: fourth-body perturbations due to Mars for SE, Earth for SM, and the Sun for MD, as well as Mars' J2 perturbation for MD.

For the initial guess, the sail is assumed to have a fixed control law in the interplanetary phases (SE and SM) and a locally optimal steering law within the Martian system (MD). The results of the Monte Carlo analysis reveal that total mission durations of seven years and below are infeasible, thus the maximum limit on the total mission duration is set at eight years. Additionally, the capture and escape ToFs are found to periodically vary over half a Martian year.

Using insights from the Monte Carlo analysis, differential evolution minimizes position and velocity errors at the linkages between the phases below a satisfactory limit while optimizing the transfer time for each leg. These initial guesses for each mission leg are considered to be sub-optimal due to the discontinuities at linkages, the use of constant sail attitude for interplanetary phases, and locally optimal steering for MD. The MD trajectories, involving multiple revolutions for escape and capture, push PSOPT to its limits; thus, these phases are not solved using the direct pseudospectral method. Consequently, the optimal control problem is limited to the interplanetary phases of both mission legs. The optimal control problem employs relevant constraints to remove discontinuities and incorporates all of the relevant perturbations considered. The outbound leg is solved first using PSOPT, and its optimized result then serves as an input for producing an initial guess for the inbound leg, which is later optimized separately.

For a near-term sail with a lightness number of 0.05, the optimization results in 329 days of stay at the MD-L1 point for a total mission duration of 7.7 years. This result, produced with only partial dependence between the outbound and return legs and a locally optimal steering law within the Martian system, is considered to an extent sub-optimal but sufficiently accurate for a preliminary mission concept to Deimos. The patched CR3BP approximation approach towards trajectory design for a sample-return mission from Deimos successfully generates valid solutions. However, it is found to be computationally expensive, where a similar study for Phobos led to computational times nine times longer than those for Deimos, and was later deemed infeasible. Therefore, for future trajectory designs for similar mission concepts to only Phobos or one that tours both Phobos and Deimos, an alternative computationally efficient method should be explored.

REFERENCES

[1] T. Usui, K. i. Bajo, W. Fujiya, Y. Furukawa, M. Koike, Y. N. Miura, H. Sugahara, S. Tachibana, Y. Takano, and K. Kuramoto, "The Importance of Phobos Sample Return for Understanding the Mars-Moon System," 6 2020.

[2] S. Campagnola, C. H. Yam, Y. Tsuda, O. Naoko, and Y. Kawakatsu, "Mission analysis for the Martian Moons Explorer (MMX) mission," *Acta Astronautica*, vol. 146, pp. 409–417, 5 2018.

[3] E. Sefton-Nash, G. Thébault, O. Witasse, D. Koschny, B. Sánchez-Cano, and A. Cardesín-Moinelo, "Visibility analysis of Phobos to support a science and exploration platform," *Earth, Planets and Space*, vol. 73, 12 2021.

[4] T. C. Duxbury, A. V. Zakharov, H. Hoffmann, and E. A. Guinness, "Spacecraft exploration of Phobos and Deimos," *Planetary and Space Science*, vol. 102, no. C, pp. 9–17, 2014.

[5] C. Bezrouk and J. S. Parker, "Ballistic capture into distant retrograde orbits around Phobos: an approach to entering orbit around Phobos without a critical maneuver near the moon," *Celestial Mechanics and Dynamical Astronomy*, vol. 130, 2 2018.

[6] C. A. Raymond, T. H. Prettyman, S. Diniega, and P. Team, "PANDORA-Unlocking the Mysteries of the Moons of Mars," tech. rep., 2015.

[7] A. L. Genova, D. Korsmeyer, L. Plice, M. Loucks, and F. Y. Yang, "Trajectory design for the phobos and deimos & mars environment (PADME) spacecraft," in *AIAA/AAS Astrodynamics Specialist Conference, 2016*, American Institute of Aeronautics and Astronautics Inc, AIAA, 2016.

[8] J. Oberst, K. Wickhusen, K. Willner, K. Gwinner, S. Spiridonova, R. Kahle, A. Coates, A. Herique, D. Plettemeier, M. Díaz-Michelena, A. Zakharov, Y. Futaana, M. Pätzold, P. Rosenblatt, D. J. Lawrence, V. Lainey, A. Gibbings, and I. Gerth, "DePhine – The Deimos and Phobos Interior Explorer," *Advances in Space Research*, vol. 62, pp. 2220–2238, 10 2018.

[9] S. Barraclough, A. Ratcliffe, R. Buchwald, H. Scheer, M. Chapuy, M. Garland, and D. Rebuffat, "PHOOTPRINT : A European Phobos Sample Return Mission," tech. rep., 2014.

[10] Y. Kawakatsu, K. Kuramoto, T. Usui, H. Sugahara, H. Otake, R. Yasumitsu, K. Yoshikawa, S. Mary, M. Grebenstein, H. Sawada, T. Imada, T. Shimada, K. Ogawa, M. Otsuki, M. Baba, K. Fujita, K. Zacny, D. Van Dyne, Y. Satou, and A. Tokaji, "Preliminary Design of Martian Moons eXploration (MMX)," in *Proceedings of the International Astronautical Congress, IAC*, vol. A3, International Astronautical Federation, IAF, 2021.

[11] R. T. Nallapu, G. Dektor, N. Kenia, J. Uglietta, S. Ichikawa, M. Herreras-Martinez, A. Choudhari, A. Chandra, S. Schwartz, E. Asphaug, and J. Thangavelautham, "Trajectory design of perseus: A cubesat mission concept to phobos," *Aerospace*, vol. 7, pp. 1–31, 12 2020.

[12] C. R. McInnes, *Solar Sailing Technology, Dynamics and Mission Applications*. 1999.

[13] A. S. Gohardani, "A historical glance at solar sails," in *AIAA SPACE 2014 Conference and Exposition*, American Institute of Aeronautics and Astronautics Inc., 2014.

[14] Y. Tsuda, O. Mori, R. Funase, H. Sawada, T. Yamamoto, T. Saiki, T. Endo, and J. Kawaguchi, "Flight status of IKAROS deep space solar sail demonstrator," *Acta Astronautica*, vol. 69, no. 9-10, pp. 833–840, 2011.

[15] C. Katan and D. Lanning, "NASA's Next Solar Sail: Lessons from NanoSail-D2."

[16] D. A. Spencer, B. Betts, J. M. Bellardo, A. Diaz, B. Plante, and J. R. Mansell, "The LightSail 2 solar sailing technology demonstration," *Advances in Space Research*, vol. 67, pp. 2878–2889, 5 2021.

[17] J. Heiligers, M. Vergaaij, and M. Ceriotti, "End-to-end trajectory design for a solar-sail-only pole-sitter at Venus, Earth, and Mars," *Advances in Space Research*, vol. 67, pp. 2995–3011, 5 2021.

[18] M. Ceriotti, J. Heiligers, and C. R. McInnes, "Trajectory and spacecraft design for a pole-sitter mission," *Journal of Spacecraft and Rockets*, vol. 51, no. 1, pp. 311–326, 2014.

[19] R. J. McKay, M. MacDonald, J. Biggs, and C. McInnes, "Survey of highly-non-Keplerian orbits with low-thrust propulsion," *Journal of Guidance, Control, and Dynamics*, vol. 34, no. 3, pp. 645–666, 2011.

[20] J. Heiligers, J. S. Parker, and M. MacDonald, "Novel solar-sail mission concepts for high-latitude earth and lunar observation," in *Journal of Guidance, Control, and Dynamics*, vol. 41, pp. 212–230, American Institute of Aeronautics and Astronautics Inc., 2018.

[21] M. Leipold, H. Fichtner, B. Heber, P. Groepper, S. Lascar, F. Burger, M. Eiden, T. Niederstadt, C. Sickinger, L. Herbeck, B. Dachwald, and W. Seboldt, "Heliopause Explorer-a sailcraft mission to the outer boundaries of the solar system," *Acta Astronautica*, vol. 59, pp. 785–796, 10 2006.

[22] R. Heller and M. Hippke, " Deceleration of High-velocity Interstellar Photon Sails into Bound Orbits at α Centauri ," *The Astrophysical Journal*, vol. 835, p. L32, 2 2017.

[23] P. Daukantas, "Breakthrough Starshot," tech. rep., 2017.

[24] B. Dachwald and W. Seboldt, "Multiple near-Earth asteroid rendezvous and sample return using first generation solar sailcraft," *Acta Astronautica*, vol. 57, pp. 864–875, 12 2005.

[25] G. W. Hughes, M. Macdonald, C. R. McInnes, A. Atzei, and P. Falkner, "Terrestrial planet sample return missions using solar sail propulsion," *Acta Astronautica*, vol. 59, pp. 797–806, 10 2006.

[26] K. Zhu, R. Zhang, D. Xu, J. Wang, and S. Li, "Venus round trip using solar sail," *Science China: Physics, Mechanics and Astronomy*, vol. 55, pp. 1485–1499, 8 2012.

[27] R. L. Staehle, B. Anderson, B. Betts, D. Blaney, C. Chow, L. Friedman, H. Hemmati, D. Jones, A. Klesh, P. Liewer, J. Lazio, M. Wen-Yu Lo, P. Mouroulis, N. Murphy, P. J. Pingree, J. Puig-Suari, T. Svitek, A. Williams, and T. Wilson, "Interplanetary CubeSats: Opening the Solar System to a Broad Community at Lower Cost," tech. rep., 2012.

[28] G. L. Matloff, T. Taylor, C. Powell, and T. Moton, "Phobos/deimos sample return via solar sail," *Annals of the New York Academy of Sciences*, vol. 1065, pp. 429–440, 2005.

[29] B. Park, *Low-Thrust Trajectory Design for Tours of the Martian Moons Low-thrust rendezvous design for tour of moons*. PhD thesis, 2021.

[30] D. Canales, M. Gupta, B. Park, and K. C. Howell, "A transfer trajectory framework for the exploration of Phobos and Deimos leveraging resonant orbits," *Acta Astronautica*, vol. 194, pp. 263–276, 5 2022.

[31] M. Vergaaij and J. Heiligers, "Time-optimal solar sail heteroclinic-like connections for an Earth-Mars cycler," *Acta Astronautica*, vol. 152, pp. 474–485, 11 2018.
[32] M. Vergaaij and J. Heiligers, "Solar-sail trajectory design to planetary pole sitters," *Journal of Guidance, Control, and Dynamics*, vol. 42, no. 6, pp. 1402–1412, 2019.
[33] J. Heiligers, G. Mingotti, and C. R. McInnes, "Optimal solar sail transfers between Halo orbits of different Sun-planet systems," *Advances in Space Research*, vol. 55, pp. 1405–1421, 3 2015.
[34] Solar System Dynamics, "Planets and planetary satellites."
[35] A. K. de Almeida Junior and A. F. B. de Almeida Prado, "Comparisons between the circular restricted three-body and bi-circular four body problems for transfers between the two smaller primaries," *Scientific Reports*, vol. 12, 12 2022.
[36] D. J. Scheeres, *Orbital Motion in Strongly Perturbed Environments Applications to Asteroid, Comet and Planetary Satellite Orbiters*. Springer, 2012.
[37] D. J. Scheeres, S. Van wal, Z. Olikara, and N. Baresi, "Dynamics in the Phobos environment," *Advances in Space Research*, vol. 63, pp. 476–495, 1 2019.
[38] D. P. Rubincam, B. F. Chao, and P. C. Thomas, "The Gravitational Field of Deimos," 1994.
[39] M. Zamaro and J. D. Biggs, "Identification of new orbits to enable future mission opportunities for the human exploration of the Martian moon Phobos," *Acta Astronautica*, vol. 119, pp. 160–182, 2 2016.
[40] J. Heiligers, J. M. Fernandez, O. R. Stohlman, and W. K. Wilkie, "Trajectory design for a solar-sail mission to asteroid 2016 HO3," *Astrodynamics*, vol. 3, pp. 231–246, 9 2019.
[41] A. D. Cox, K. Howell, M. Corless, W. Crossley, C. Frueh, and G. Blaisdell, *A dynamical systems perspective for preliminary low-thrust trajectory design in multi-body regimes*. PhD thesis, Purdue University Graduate School, West Lafayette, Indiana, 2020.
[42] V. L. Coverstone and J. E. Prussing, "Technique for Escape from Geosynchronous Transfer Orbit Using a Solar Sail," *Journal of Guidance, Control, and Dynamics*, vol. 26, no. 4, pp. 628–634, 2003.
[43] V. M. Becerra, "Solving complex optimal control problems at no cost with PSOPT," in *2010 IEEE International Symposium on Computer-Aided Control System Design*, pp. 1391–1396, IEEE, 9 2010.
[44] V. M. Becerra, "PSOPT optimal control solver user manual," 2022.
[45] N. K. M. Bakx and M. J. Heiligers, "Using solar-sail induced dynamics to increase the warning time for solar storms heading towards earth," tech. rep., 2021.
[46] M. Macdonald and C. R. McInnes, "Realistic earth escape strategies for solar sailing," *Journal of Guidance, Control, and Dynamics*, vol. 28, no. 2, pp. 315–323, 2005.
[47] H. Spencer and K. A. Carroll, "Real Solar Sails Are Not Ideal, And Yes It Matters," 2014.

APPENDIX: FOURTH BODY PERTURBATIONS

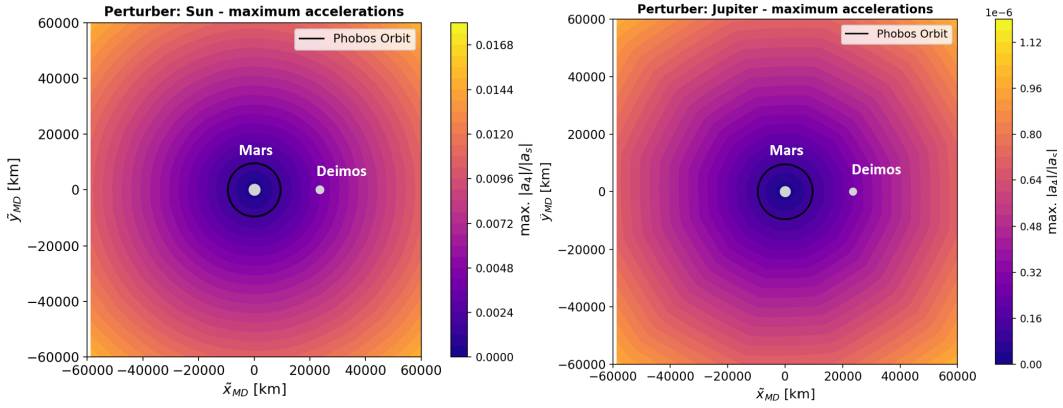

(a) (b)

Figure 16: Maximum point mass gravitational perturbations normalized against the maximum sail acceleration at that distance and plotted in the Mars-Deimos CR3BP system. (a) Sun (b) Jupiter

3 Conclusion and Future Recommendations

This chapter concludes the thesis report by answering the research questions posed in Chapter 1 in Section 3.1 and by stating the possible recommendations for future work in Section 3.2.

3.1. Conclusion

Mars has piqued human interest for many years, and additionally owing to its accessibility from Earth, it has stolen the limelight as the most prominent destination for space exploration in the Solar System. However, its natural satellites, Phobos and Deimos, have received little attention, and no dedicated missions have flown successfully to date. The Japanese Aerospace Exploration Agency (JAXA), with its Martian Moons eXploration (MMX) mission, seeks to bridge this gap. MMX aims to conduct numerous observations of Phobos and Deimos and return samples from Phobos by 2029. Nonetheless, there might be a future need to conduct additional scientific exploration at the moons, possibly complementing and supplementing the data gathered by MMX. In this context, a low-thrust propulsion system could offer a cost-effective solution for a sample-return mission from the moons. One of the fascinating low-thrust techniques is solar sail propulsion which requires no fuel and is propelled solely by solar radiation pressure. No past studies were found that explored the trajectory design to the Martian moons. To that extent, this study investigated the trajectory design for a solar-sail propelled spacecraft targeting a sample-return mission from the less-studied Martian moon, Deimos. Following this, the research objective for the study was laid down as: *"To design solar-sail propelled transfer trajectories by leveraging heteroclinic-like connections for a sample-return mission from the Martian moon Deimos, with the objective to maximize the scientific output."*

The research objective was achieved by designing the trajectories using a patched circular restricted three-body (CR3BP) approach to establish continuous trajectories between different CR3BP systems. Specifically, heteroclinic-like connections were found for solar-sail perturbed trajectories that depart from the Sun-Earth L_2 point and arrive and stay at the L_1 point of the Mars-Deimos CR3BP system, and vice-versa for the return trajectory. This patched CR3BP method provided an initial guess for a direct pseudospectral method to solve the optimal control problem (OCP) at hand. The optimization aimed to maximize the scientific output by increasing the stay duration near Deimos. This was achieved by reducing the time-of-flights (ToFs) for both the outbound and inbound trajectories, within a maximum mission duration of eight years.

The answers to the research questions, that aided in achieving the objective, are as follows:

1. *How feasible is patched CR3BP as a technique to design trajectories for a sample-return mission from a Martian moon?*

   Answer: For the patched CR3BP approach, three separate CR3BP systems were considered, namely, Sun-Earth (SE), Sun-Mars (SM), and Mars-Deimos (MD), with the arrival/departure locations being the SE-L_2 and MD-L_1 point. To design a continuous trajectory, heteroclinic-like connections were sought between the solar-sail perturbed invariant manifolds of the SE-L_2 and MD-L_1, for both the outbound leg (SE-L_2 to MD-L_1) and the inbound leg (MD-L_1 to SE-L_2). To achieve this, first, a Monte Carlo analysis was performed to explore the design

space for minimum Euclidean position and velocity errors between the two manifolds (of a given mission leg). The insights from this were later used to further minimize the errors using the differential evolution (DE) algorithm whilst also minimizing the ToF of each leg. Throughout the implementation of these two methods, it was assumed that the sail attitude was constant for each of the two manifolds in their interplanetary phases (Sun-Earth and Sun-Mars) and locally optimal within the Martian SOI (Mars-Deimos frame). Once the errors were below a sufficiently accurate value, the results of DE were used as initial guesses for a direct pseudospectral method, implemented through PSOPT, that solved the OCP with a full set of relevant perturbations. The relevant perturbations implemented were: the Mars fourth-body perturbation in Sun-Earth CR3BP, the Earth fourth-body in Sun-Mars CR3BP, the Sun fourth-body perturbation in Mars-Deimos CR3BP and Mars J_2 perturbation in Mars-Deimos CR3BP.

This approach successfully generated valid optimal solutions; however, it was computationally very demanding, primarily due to the spiral escape and capture trajectories within the Martian system. The low mass of Deimos rendered the MD CR3BP assumption ineffective, causing the trajectory to behave similarly to that in a two-body problem approximation. Extending the same method to Phobos resulted in computational times nine times that for Deimos, making it impractical with the available computational resources. Additionally, due to the software limitations of PSOPT, only a locally optimal steering law was considered for the spiral trajectory segment with multiple revolutions. This also meant that both the legs could not be solved simultaneously (for an end-to-end trajectory design) and were solved with only a partial dependence on each other. Thus, this means that the results obtained are rather sub-optimal in terms of maximizing the stay duration at Deimos. Nonetheless, they are considered to be adequately optimal for a preliminary mission design.

In summary, while a patched CR3BP approximation provides trajectories that meet all constraints and optimise the objective to a satisfactory extent, it may not be the most suitable option for a mission to only Phobos or to tour both Phobos and Deimos given the computational overhead.

2. *What is the maximum feasible duration of stay in the vicinity of Deimos for a given possible minimum mission duration?*

   Answer: The results of the Monte Carlo analysis made it evident that a total mission duration of seven years or lower was not feasible, thus the maximum mission duration was set to eight years. Following this, for the assumption of an ideal sail with a lightness number of 0.05 and departure epoch between 2030-2032, the maximum duration of stay at MD-L_1 was found to be 329 days with a total mission duration of 7.7 years (2815 days). It is 80 days more than that of the initial guess.

   The majority of the flight time was spent in the interplanetary transfer - 1019.72 days for the outbound leg and 998.08 for the inbound leg. The spiral capture and escape ToFs within the Martian system were 226.55 days and 241.72 days, respectively. As a comparison, the MMX mission which employs a chemical thruster, has a total mission timeline of five years with three of those spent operating within the Martian system (1.8 years in the proximity of Phobos) [12]. This result is significantly large compared to the planned MMX mission but expected given its low-thrust nature. Additionally, even compared to an electric propulsion engine (modelled after a realistic engine), as implemented by Park [16] for a transfer from the low Earth orbit to MD L_1, the ToFs for the transfers are greater. The fuel-optimal solutions obtained by Park had a ToF of 500 days and 27.75 days for the interplanetary and Martian phases, respectively.

3.2. Future Works and Recommendations

Based on the methodology undertaken in this thesis and the outcomes, the following recommendations are made for future works:

1. **Quantify the significance of solar sails:** While the current thesis focuses on trajectory design to enable a sample-return mission from Deimos, it would also be interesting to analyse how substantially can a solar-sail propelled spacecraft affect the total mission cost compared to a chemical or electric propulsion system. A study conducted by Hughes et al. [35] demonstrated that while sample-return missions from Mercury and a high inclination near-Earth asteroid using a sail can lead to substantial budget savings, those to Mars and Venus only resulted in a modest reduction in mission costs. Recall that the ToF for different legs of the mission obtained in this study for a near-term sail technology (0.05 lightness number) itself is significantly larger than the flight-proven electric propulsion, which in turn might result in greater operational costs. Therefore, a cost analysis to quantify the significance of using a solar sail for a mission to and from the Martian moons could be an interesting addition to future works, especially to assess the practical feasibility of employing it.
2. **Alternate modelling approach:** A potentially more efficient approach to address the computational burden and enhance the optimality of solutions could be to explore a patched 2BP-CR3BP model coupled with an orbital averaging method. This alternative would involve using a CR3BP model for trajectories near the moons that transitions to a two-body model to compute the spiral escape/capture trajectories through orbital averaging. In this approach, equations of motion are formulated in terms of slowly evolving orbital elements, and by averaging the dynamics over one orbital period, terms with short periods can be eliminated. This can significantly reduce the number of collocation points needed to capture the dynamics using a direct method. In the context of solar sail, studies by Fitzgerald [51] and Tresaco et al. [52] have employed some form of averaging techniques tailored to their specific applications, wherein particularly Fitzgerald uses a direct pseudospectral method to solve the corresponding OCP. However, no literature has been found on its implementation for solar sail escape and capture trajectories. McInnes [19] briefly mentions its application to reduce computational effort in designing escape trajectories, suggesting the generation of escape trajectories up to a sub-escape point using averaging given its accuracy limitations, beyond which the full set of equations should be integrated for the final few revolutions of the escape. Nonetheless, it could be an interesting approach for future work for computationally efficient analyses.
3. **Departure/arrival orbits:** The current thesis, for simplicity and proof of concept, assumes that the trajectories depart and arrive at the collinear Lagrange points of the Sun-Earth (SE) and Mars-Deimos (MD) systems. However, in reality, this is impractical as the real locations of the Lagrange points are rather fuzzy due to the orbit eccentricities and additional perturbations, and represent more of a region in space. Therefore, instead of considering the departure and arrival locations as points in the rotating reference frame, Lagrange point orbits can be considered. Additionally, the departure and arrival orbit near the Earth could be extended to either the low Earth orbits or the Geostationary orbits, employing similar spiral escape or capture segments within the Earth's SOI.

   Furthermore, Deimos and Phobos have an irregular shape and exhibit an extremely inhomogeneous gravity field, which coupled with their orbital eccentricities, though small, strongly influence the dynamics in their close vicinity [53]. Past studies have observed that under this strongly perturbed environment, multiple closed orbits which exist in a simple CR3BP system diverge to impact the surface [43, 54, 55]. Therefore, accurate modelling of both the gravity and the orbit of the Martian moons is a necessity to design true orbits near them. No re-

search has been performed on the stability and dynamics of solar sail-perturbed orbits at the Lagrange points of these Moons. For a more practical design, further studies need to explore this.

4. **Higher-fidelity models:** The dynamical model employed for the given case study can be made more realistic by potentially employing the following:

   - If continued with a patched CR3BP approximation that assumes the circular motions of the primaries about their barycenters, a more realistic approach would involve incorporating the eccentricities of their orbits. This can be achieved by implementing an elliptical restricted three-body problem (ER3BP). In fact, for Lagrange point orbits at the colinear Lagrange points of both the Mars-Deimos and Mars-Phobos systems, it was found that the moons' orbital eccentricity, though small, significantly influences these orbits when combined with the inhomogeneous gravity fields of the moons. This influence is to the extent that multiple closed orbits, which exist in a simple CR3BP system, diverge and impact the surface [43, 53, 54, 55].
   - Since the trajectory involves multiple revolutions around Mars, it could spend a significant amount of time within Mars' and potentially even Deimos' and Phobos' eclipse regions. During an eclipse, the sail would either generate low or no thrust and can influence the time of flight for the escape or capture segments.
   - Constraining sail steering rates and capabilities. Real sail actuators cannot steer at the higher rates demanded by the control profiles obtained in this thesis, especially for spiral trajectories where an instantaneous 180 deg rotation of the sail is required, and fast changes in attitude occur at lower altitudes. This also extends to the maximum cone angles that a practical sail can take, as they are inherently limited by the thermal and structural constraints of the sail [56]. Thus a more practical simulation should incorporate these constraints during optimization - which might again lead to an increase in mission time.
   - Considering optimal imperfections and their associated uncertainties. The present trajectories assume an ideal sail, where the photons are reflected in a specular manner from a flat surface. In reality, the sail experiences diffuse reflection, absorption, and thermal emission, and is not perfectly flat, but instead exhibits billowing and wrinkles [19]. Additionally, the sail's optical properties may also degrade over time [57]. To accurately model the dynamics of solar sails, various sophisticated mathematical models have been developed in the past to account for these imperfections [19, 57, 58].
   - Finally, the trajectories obtained from any models should be validated against a comparatively higher fidelity ephemeris model to check whether they can best approximate the real-world scenario.

5. **Martian moon to moon transfer:** Instead of focusing solely on a single moon, the solar sail's fuel-less low-thrust capabilities could be an efficient possibility for targeting both Deimos and Phobos as sample-return destinations within a single mission. This mission framework could involve visiting either Deimos first and then Phobos or vice versa. A preliminary analysis for such a mission scenario was conducted in this study using the patched CR3BP model, as detailed in Appendix C. It was found that unlike other multi-moon systems such as the Jovian moons [59], Phobos and Deimos, having almost negligible mass, did not have heteroclinic-like connections between their respective Lagrange points when employing both fixed sail attitude and locally optimal control laws.

   This essentially translates to designing transfers between two planetocentric near-circular orbits, which has been an ongoing challenge using solar sails due to their inherently low

control authority - especially since they cannot face towards the Sun. However, despite these challenges, it has been demonstrated that even non-ideal solar sails possess the capability to achieve transfers between planet-centered near-circular orbits [60]. Achieving time-optimal transfers between such orbits necessitates a sufficiently accurate initial guess to solve the optimal control problem, as illustrated earlier in this thesis. The locally optimal control law applied in this thesis focuses on maximizing the rate of change of the orbit semi-major axis. While effective, this alone may not be adequate for achieving rendezvous with the desired orbit. Consequently, additional analytical approaches have been explored, such as blending locally optimal control laws for various orbital elements using a solar sail. For instance, a solar sailing Q-law for planetocentric orbits was recently devised [61]. Methods like these could thus be explored in the future for solar sail transfers between Deimos and Phobos, and potentially employ the patched 2BP-CR3BP approach to ensure transfer to orbits near the moons which require a multi-body system approximation.

Bibliography

[1] T. Usui, K. i. Bajo, W. Fujiya, Y. Furukawa, M. Koike, Y. N. Miura, H. Sugahara, S. Tachibana, Y. Takano, and K. Kuramoto, "The Importance of Phobos Sample Return for Understanding the Mars-Moon System," 6 2020.

[2] S. Campagnola, C. H. Yam, Y. Tsuda, O. Naoko, and Y. Kawakatsu, "Mission analysis for the Martian Moons Explorer (MMX) mission," *Acta Astronautica*, vol. 146, pp. 409–417, 5 2018.

[3] E. Sefton-Nash, G. Thébault, O. Witasse, D. Koschny, B. Sánchez-Cano, and A. Cardesín-Moinelo, "Visibility analysis of Phobos to support a science and exploration platform," *Earth, Planets and Space*, vol. 73, 12 2021.

[4] A. N. Deutsch, J. W. Head, K. R. Ramsley, C. M. Pieters, R. W. Potter, A. M. Palumbo, M. S. Bramble, J. P. Cassanelli, E. R. Jawin, L. M. Jozwiak, H. H. Kaplan, C. F. Lynch, A. C. Pascuzzo, L. Qiao, and D. K. Weiss, "Science exploration architecture for Phobos and Deimos: The role of Phobos and Deimos in the future exploration of Mars," *Advances in Space Research*, vol. 62, pp. 2174–2186, 10 2018.

[5] S. L. Murchie, D. T. Britt, and C. M. Pieters, "The value of Phobos sample return," *Planetary and Space Science*, vol. 102, no. C, pp. 176–182, 2014.

[6] T. C. Duxbury, A. V. Zakharov, H. Hoffmann, and E. A. Guinness, "Spacecraft exploration of Phobos and Deimos," *Planetary and Space Science*, vol. 102, no. C, pp. 9–17, 2014.

[7] C. Bezrouk and J. S. Parker, "Ballistic capture into distant retrograde orbits around Phobos: an approach to entering orbit around Phobos without a critical maneuver near the moon," *Celestial Mechanics and Dynamical Astronomy*, vol. 130, 2 2018.

[8] C. A. Raymond, T. H. Prettyman, S. Diniega, and P. Team, "PANDORA-Unlocking the Mysteries of the Moons of Mars," tech. rep., 2015.

[9] A. L. Genova, D. Korsmeyer, L. Plice, M. Loucks, and F. Y. Yang, "Trajectory design for the phobos and deimos & mars environment (PADME) spacecraft," in *AIAA/AAS Astrodynamics Specialist Conference, 2016*, American Institute of Aeronautics and Astronautics Inc, AIAA, 2016.

[10] J. Oberst, K. Wickhusen, K. Willner, K. Gwinner, S. Spiridonova, R. Kahle, A. Coates, A. Herique, D. Plettemeier, M. Díaz-Michelena, A. Zakharov, Y. Futaana, M. Pätzold, P. Rosenblatt, D. J. Lawrence, V. Lainey, A. Gibbings, and I. Gerth, "DePhine – The Deimos and Phobos Interior Explorer," *Advances in Space Research*, vol. 62, pp. 2220–2238, 10 2018.

[11] S. Barraclough, A. Ratcliffe, R. Buchwald, H. Scheer, M. Chapuy, M. Garland, and D. Rebuffat, "PHOOTPRINT : A European Phobos Sample Return Mission," tech. rep., 2014.

[12] Y. Kawakatsu, K. Kuramoto, T. Usui, H. Sugahara, H. Otake, R. Yasumitsu, K. Yoshikawa, S. Mary, M. Grebenstein, H. Sawada, T. Imada, T. Shimada, K. Ogawa, M. Otsuki, M. Baba, K. Fujita, K. Zacny, D. Van Dyne, Y. Satou, and A. Tokaji, "Preliminary Design of Martian Moons eXploration (MMX)," in *Proceedings of the International Astronautical Congress, IAC*, vol. A3, International Astronautical Federation, IAF, 2021.

[13] R. T. Nallapu, G. Dektor, N. Kenia, J. Uglietta, S. Ichikawa, M. Herreras-Martinez, A. Choudhari, A. Chandra, S. Schwartz, E. Asphaug, and J. Thangavelautham, "Trajectory design of perseus: A cubesat mission concept to phobos," *Aerospace*, vol. 7, pp. 1–31, 12 2020.

[14] N. Strange, R. G. Merrill, D. Landau, B. Drake, J. Brophy, and R. Hofer, "Human missions to phobos and deimos using combined chemical and solar electric propulsion," in *47th AIAA/ASME/SAE/ASEE Joint Propulsion Conference and Exhibit 2011*, 2011.

[15] E. Belbruno and J. Miller, "Human & Robotic mission applications of low-energy transfers to Phobos & Deimos," tech. rep., 1993.

[16] B. Park, *Low-Thrust Trajectory Design for Tours of the Martian Moons Low-thrust rendezvous design for tour of moons*. PhD thesis, 2021.

[17] U. Derz, A. Ohndorf, and B. Bischof, "Mission Analysis of Robotic, Low Thrust Missions to the Martian moons Deimos and Phobos," in *IAC*, 2011.

[18] J. A. Englander, M. A. Vavrina, B. Naasz, R. G. Merill, and M. Qu, "Mars, phobos, and deimos sample return enabled by ARRM alternative trade study spacecraft," in *AIAA/AAS Astrodynamics Specialist Conference 2014*, American Institute of Aeronautics and Astronautics Inc., 2014.

[19] C. R. McInnes, *Solar Sailing Technology, Dynamics and Mission Applications*. 1999.

[20] A. S. Gohardani, "A historical glance at solar sails," in *AIAA SPACE 2014 Conference and Exposition*, American Institute of Aeronautics and Astronautics Inc., 2014.

[21] NASA, "The Voyage of Mariner 10, Chapter 7," 1978.

[22] Y. Tsuda, O. Mori, R. Funase, H. Sawada, T. Yamamoto, T. Saiki, T. Endo, and J. Kawaguchi, "Flight status of IKAROS deep space solar sail demonstrator," *Acta Astronautica*, vol. 69, no. 9-10, pp. 833–840, 2011.

[23] C. Katan and D. Lanning, "NASA's Next Solar Sail: Lessons from NanoSail-D2."

[24] D. A. Spencer, B. Betts, J. M. Bellardo, A. Diaz, B. Plante, and J. R. Mansell, "The LightSail 2 solar sailing technology demonstration," *Advances in Space Research*, vol. 67, pp. 2878–2889, 5 2021.

[25] J. Heiligers, B. Diedrich, B. Derbes, and C. R. Mcinnes, "Sunjammer: Preliminary end-to-end-mission design," in *AIAA/AAS Astrodynamics Specialist Conference 2014*, American Institute of Aeronautics and Astronautics Inc., 2014.

[26] J. Heiligers, M. Vergaaij, and M. Ceriotti, "End-to-end trajectory design for a solar-sail-only pole-sitter at Venus, Earth, and Mars," *Advances in Space Research*, vol. 67, pp. 2995–3011, 5 2021.

[27] M. Ceriotti, J. Heiligers, and C. R. McInnes, "Trajectory and spacecraft design for a pole-sitter mission," *Journal of Spacecraft and Rockets*, vol. 51, no. 1, pp. 311–326, 2014.

[28] R. J. McKay, M. MacDonald, J. Biggs, and C. McInnes, "Survey of highly-non-Keplerian orbits with low-thrust propulsion," *Journal of Guidance, Control, and Dynamics*, vol. 34, no. 3, pp. 645–666, 2011.

[29] J. Heiligers, M. Ceriotti, C. R. McInnes, and J. D. Biggs, "Displaced geostationary orbit design using hybrid sail propulsion," *Journal of Guidance, Control, and Dynamics*, vol. 34, no. 6, pp. 1852–1866, 2011.

[30] J. Heiligers, J. S. Parker, and M. MacDonald, "Novel solar-sail mission concepts for high-latitude earth and lunar observation," in *Journal of Guidance, Control, and Dynamics*, vol. 41, pp. 212–230, American Institute of Aeronautics and Astronautics Inc., 2018.

[31] M. Leipold, H. Fichtner, B. Heber, P. Groepper, S. Lascar, F. Burger, M. Eiden, T. Niederstadt, C. Sickinger, L. Herbeck, B. Dachwald, and W. Seboldt, "Heliopause Explorer-a sailcraft mission to the outer boundaries of the solar system," *Acta Astronautica*, vol. 59, pp. 785–796, 10 2006.

[32] R. Heller and M. Hippke, " Deceleration of High-velocity Interstellar Photon Sails into Bound Orbits at α Centauri ," *The Astrophysical Journal*, vol. 835, p. L32, 2 2017.

[33] P. Daukantas, "Breakthrough Starshot," tech. rep., 2017.

[34] B. Dachwald and W. Seboldt, "Multiple near-Earth asteroid rendezvous and sample return using first generation solar sailcraft," *Acta Astronautica*, vol. 57, pp. 864–875, 12 2005.

[35] G. W. Hughes, M. Macdonald, C. R. McInnes, A. Atzei, and P. Falkner, "Terrestrial planet sample return missions using solar sail propulsion," *Acta Astronautica*, vol. 59, pp. 797–806, 10 2006.

[36] G. W. Hughes, M. Macdonald, C. R. McInnes, A. Atzei, and P. Falkner, "Analysis of a solar sail mercury sample return mission," in *International Astronautical Federation - 55th International Astronautical Congress 2004*, vol. 9, pp. 6106–6116, 2004.

[37] K. Zhu, R. Zhang, D. Xu, J. Wang, and S. Li, "Venus round trip using solar sail," *Science China: Physics, Mechanics and Astronomy*, vol. 55, pp. 1485–1499, 8 2012.

[38] R. L. Staehle, B. Anderson, B. Betts, D. Blaney, C. Chow, L. Friedman, H. Hemmati, D. Jones, A. Klesh, P. Liewer, J. Lazio, M. Wen-Yu Lo, P. Mouroulis, N. Murphy, P. J. Pingree, J. Puig-Suari, T. Svitek, A. Williams, and T. Wilson, "Interplanetary CubeSats: Opening the Solar System to a Broad Community at Lower Cost," tech. rep., 2012.

[39] G. L. Matloff, T. Taylor, C. Powell, and T. Moton, "Phobos/deimos sample return via solar sail," *Annals of the New York Academy of Sciences*, vol. 1065, pp. 429–440, 2005.

[40] D. Canales, M. Gupta, B. Park, and K. C. Howell, "A transfer trajectory framework for the exploration of Phobos and Deimos leveraging resonant orbits," *Acta Astronautica*, vol. 194, pp. 263–276, 5 2022.

[41] H. Han, X. Li, and J. Ren, "Transfer between libration orbits through the outer branches of manifolds for Phobos exploration," *Acta Astronautica*, vol. 189, pp. 321–336, 12 2021.

[42] M. S. Wallace, J. S. Parker, N. J. Strange, and D. Grebow, "Orbital Operations for Phobos and Deimos Exploration," in *AIAA/AAS Astrodynamics Specialist Conference 2012*, 2012.

[43] Y. Wang and X. Wu, "Analysis of Phobos' dynamical environment considering effects of ephemerides and physical libration," *Monthly Notices of the Royal Astronomical Society*, vol. 497, pp. 416–434, 9 2020.

[44] W. Sang Koon, M. W. Lo, J. E. Marsden, and S. D. Ross, *Dynamical Systems, the Three-Body Problem and Space Mission Design*. 1.3 ed., 2006.

[45] R. L. Anderson and M. W. Lo, "Role of invariant manifolds in low-thrust trajectory design," *Journal of Guidance, Control, and Dynamics*, vol. 32, no. 6, pp. 1921–1930, 2009.

[46] F. Topputo, M. Vasile, and F. Bernelli-Zazzera, "Low Energy Interplanetary Transfers Exploiting Invariant Manifolds of the Restricted Three-Body Problem," *The Journal of the Astronautical Sciences*, vol. 53, no. 4, pp. 353–372, 2004.

[47] G. Mingotti, F. Topputo, and F. Bernelli-Zazzera, "Earth-Mars transfers with ballistic escape and low-thrust capture," *Celestial Mechanics and Dynamical Astronomy*, vol. 110, pp. 169–188, 6 2011.

[48] M. Vergaaij and J. Heiligers, "Time-optimal solar sail heteroclinic-like connections for an Earth-Mars cycler," *Acta Astronautica*, vol. 152, pp. 474–485, 11 2018.

[49] M. Vergaaij and J. Heiligers, "Solar-sail trajectory design to planetary pole sitters," *Journal of Guidance, Control, and Dynamics*, vol. 42, no. 6, pp. 1402–1412, 2019.

[50] J. Heiligers, G. Mingotti, and C. R. McInnes, "Optimal solar sail transfers between Halo orbits of different Sun-planet systems," *Advances in Space Research*, vol. 55, pp. 1405–1421, 3 2015.

[51] R. M. Fitzgerald, "Characterizing minimum-time solar sail geostationary orbit transfers using pseudospectral optimal control," *Journal of Spacecraft and Rockets*, vol. 58, no. 4, pp. 997–1009, 2021.

[52] E. Tresaco, A. Elipe, and J. P. S. Carvalho, "Frozen orbits for a solar sail around mercury," *Journal of Guidance, Control, and Dynamics*, vol. 39, no. 7, pp. 1657–1664, 2016.

[53] M. Zamaro and J. D. Biggs, "Identification of new orbits to enable future mission opportunities for the human exploration of the Martian moon Phobos," *Acta Astronautica*, vol. 119, pp. 160–182, 2 2016.

[54] D. J. Scheeres, S. Van wal, Z. Olikara, and N. Baresi, "Dynamics in the Phobos environment," *Advances in Space Research*, vol. 63, pp. 476–495, 1 2019.

[55] D. J. Scheeres, *Orbital Motion in Strongly Perturbed Environments Applications to Asteroid, Comet and Planetary Satellite Orbiters*. Springer, 2012.

[56] H. Spencer and K. A. Carroll, "Real Solar Sails Are Not Ideal, And Yes It Matters," 2014.

[57] B. Dachwald, G. Mengali, A. A. Quarta, and M. Macdonald, "Parametric model and optimal control of solar sails with optical degradation," *Journal of Guidance, Control, and Dynamics*, vol. 29, no. 5, pp. 1170–1178, 2006.

[58] X. Huang, X. Zeng, C. Circi, G. Vulpetti, and D. Qiao, "Analysis of the solar sail deformation based on the point cloud method," *Advances in Space Research*, vol. 67, pp. 2613–2627, 5 2021.

[59] W. Sang Koon, M. W. Lo, J. E. Jerrold Marsden, and S. D. Ross, "Constructing a Low Energy Transfer Between Jovian Moons," tech. rep., 2000.

[60] A. Herasimenka, L. Dell'elce, J. B. Caillau, and J. B. Pomet, "Controllability Properties of Solar Sails," *Journal of Guidance, Control, and Dynamics*, vol. 46, pp. 900–909, 5 2023.

[61] K. Oguri, G. Lantoine, A. E. Petropoulos, and J. W. McMahon, "Solar Sailing Q-Law for Planetocentric, Many-Revolution Sail Orbit Transfers," *Journal of Guidance, Control, and Dynamics*, vol. 46, pp. 2005–2014, 10 2023.

[62] Solar System Dynamics, "Three-Body Periodic Orbits."

[63] J. S. Parker and R. L. Anderson, *Low-energy lunar trajectory design*. 2013.

[64] A. K. de Almeida Junior and A. F. B. de Almeida Prado, “Comparisons between the circular restricted three-body and bi-circular four body problems for transfers between the two smaller primaries,” *Scientific Reports*, vol. 12, 12 2022.

[65] M. Zamaro, *Natural and artificial orbits around the Martian moon Phobos*. PhD thesis, University of Strathclyde, Glasgow, Scotland, 2015.

[66] N. K. M. Bakx and M. J. Heiligers, “Using solar-sail induced dynamics to increase the warning time for solar storms heading towards earth,” tech. rep., 2021.

[67] P. Virtanen, R. Gommers, T. E. Oliphant, M. Haberland, T. Reddy, D. Cournapeau, E. Burovski, P. Peterson, W. Weckesser, J. Bright, S. J. van der Walt, M. Brett, J. Wilson, K. J. Millman, N. Mayorov, A. R. J. Nelson, E. Jones, R. Kern, E. Larson, C. J. Carey, I. Polat, Y. Feng, E. W. Moore, J. VanderPlas, D. Laxalde, J. Perktold, R. Cimrman, I. Henriksen, E. A. Quintero, C. R. Harris, A. M. Archibald, A. H. Ribeiro, F. Pedregosa, P. van Mulbregt, and SciPy 1.0 Contributors, “SciPy 1.0: Fundamental Algorithms for Scientific }Computing in Python,” *Nature Methods*, vol. 17, pp. 261–272, 2020.

[68] L. Petzold, “Automatic selection of methods for solving stiff and nonstiff systems of ordinary differential equations,” *SIAM Journal on Scientific and Statistical Computing*, vol. 4, pp. 136–148, 1983.

[69] K. V. Price, R. M. Storn, and J. A. Lampinen, *Differential Evolution: A practical approach to global optimization*. Springer, 2005.

[70] Solar System Dynamics, “Planets and planetary satellites.”

[71] A. Farrés, “Transfer orbits to L4 with a solar sail in the Earth-Sun system,” *Acta Astronautica*, vol. 137, pp. 78–90, 8 2017.

A Verification and Validation

This appendix discusses the verification and validation of the mathematical models and numerical techniques used to produce the sample-return solar sail trajectories from the Martian moons in the thesis. The chapter is divided into two sections: Section A.1 verifies the dynamical models, and Section A.2 the PSOPT optimization technique.

A.1. Dynamical Model

All the components of the dynamical model discussed in the journal article are verified in this section, this includes: the circular restricted three-body problem (CR3BP), frame transformations, solar sail acceleration, fourth-body perturbation and J_2 perturbation.

A.1.1. Circular Restricted Three-body Problem

Three major components need to be verified to verify the implementation of the CR3BP for the present application: the accurate computation of the Lagrange point locations, the computation of ballistic invariant manifolds and the propagation of the CR3BP equations of motion (EoM), the latter two are combined into a single section.

Lagrange Points

The CR3BP exhibits five equilibrium solutions, called the Lagrange points, of which this study utilizes the colinear L_1 and L_2 points for different phases of the missions. To reiterate, the EoM of an un-perturbed CR3BP are presented again:

$$\ddot{x} = 2\dot{y} + \frac{\partial U}{\partial x}, \quad \ddot{y} = -2\dot{x} + \frac{\partial U}{\partial y}, \quad \ddot{z} = \frac{\partial U}{\partial z} \tag{A.1}$$

where U represents the effective gravitational potential given by Eq. A.2.

$$U = -\frac{1}{2}(x^2 + y^2) - \frac{1-\mu}{r_1} - \frac{\mu}{r_2} \tag{A.2}$$

Now, for a body to be in equilibrium, the gradient of the effective potential (∇U) should be zero. Thus, the colinear Lagrange points, that lie along the line of the primaries, can be computed as:

$$\frac{\partial U}{\partial x} = x - (1-\mu)\frac{x+\mu}{r_1^3} - \mu\frac{x-1+\mu}{r_2^3} = 0 \tag{A.3}$$

where, $r_1 = |\mu + x|$ is the distance from the first primary along the x-axis and $r_2 = |1 - \mu - x|$ is the distance from the second primary. The Eq. A.3 has three real roots between the intervals, $(-\infty, -\mu)$, $(-\mu, 1-\mu)$ and $(1-\mu, \infty)$ respectively. However, given that it does not have a closed analytical solution, they are computed using the Newton-Raphson method. The locations of these points computed in this thesis are successfully verified against the values for the Sun-Earth (SE) and Mars-Phobos (MP) systems available in literature [62], shown in Table A.1.

Table A.1: The estimated and literature positions of the Lagrange points [62].

		L_1	L_2	L_3
Estimated	Sun-Earth	0.98997092	1.01009043	-1.000001272
	Mars-Phobos	0.99824982	1.00175219	-1.000000006
Literature	Sun-Earth	0.98997092	1.01009044	-1.00000127
	Mars-Phobos	0.99824982	1.00175219	-1.00000001

Invariant Manifolds

To generate initial guesses for transfer trajectories, the implementation of invariant manifolds is crucial. The stable and unstable invariant manifolds are computed by perturbing the motions along the eigenvectors corresponding to the non-imaginary eigenvalues of the Jacobian matrix (A). The Jacobian is derived from the linearized approximation of the EoM, Eq. A.1, in the proximity of the Lagrange point of interest. This Jacobian matrix is defined as:

$$A = \begin{bmatrix} 0 & 0 & 0 & 1 & 0 & 0 \\ 0 & 0 & 0 & 0 & 1 & 0 \\ 0 & 0 & 0 & 0 & 0 & 1 \\ U_{xx} & U_{xy} & U_{xz} & 0 & 2 & 0 \\ U_{xy} & U_{yy} & U_{yz} & -2 & 0 & 0 \\ U_{xz} & U_{yz} & U_{zz} & 0 & 0 & 0 \end{bmatrix} \tag{A.4}$$

Here, U_{ij} indicates the second-order partial derivatives of the effective potential with respect to i and j. The stable eigenvector corresponds to the negative real eigenvalue, while the unstable eigenvector corresponds to the positive real eigenvalue.

Verification is performed by computing the eigenvalues associated with the Sun-Earth CR3BP system and comparing them with literature, as outlined in Table A.2. This comparison ensures the correct implementation of the invariant manifolds in the study.

Table A.2: The estimated and literature eigenvalues for the Sun-Earth CR3BP system [63]

		γ_1	γ_2	γ_3	γ_4
Estimated	L_1	2.53265917	-2.53265917	2.08645356i	-2.08645356i
	L_2	-2.48431672	2.48431672	2.05701419i	-2.05701419i
Literature	L_1	-2.532659	2.532659	2.0864535i	-2.0864535i
	L_2	-2.484317	2.484317	2.057014i	-2.057014i

While this does indeed confirm the right computation of the eigenvalues and consequently the eigenvectors, the propagation of the manifolds isn't verified. This was again achieved by plotting the stable and unstable invariant manifolds emanating from the Earth-Moon L_1 point and cross-referencing them with existing literature, as illustrated in Fig. A.1. This also verifies the correct implementation and integration of the CR3BP EoM.

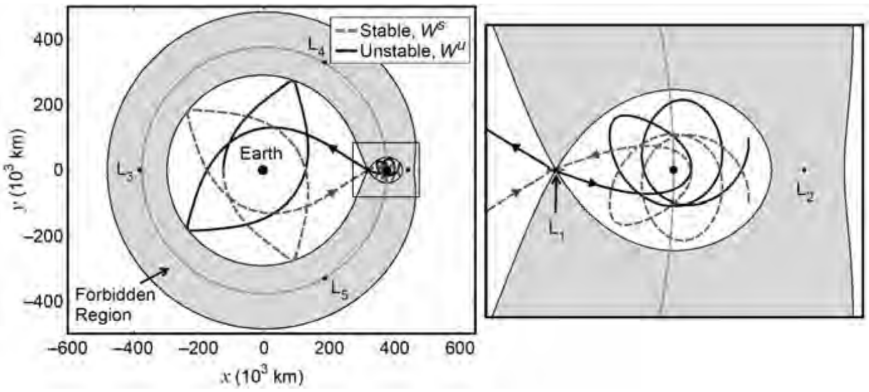

(a) Plot from literature [63].

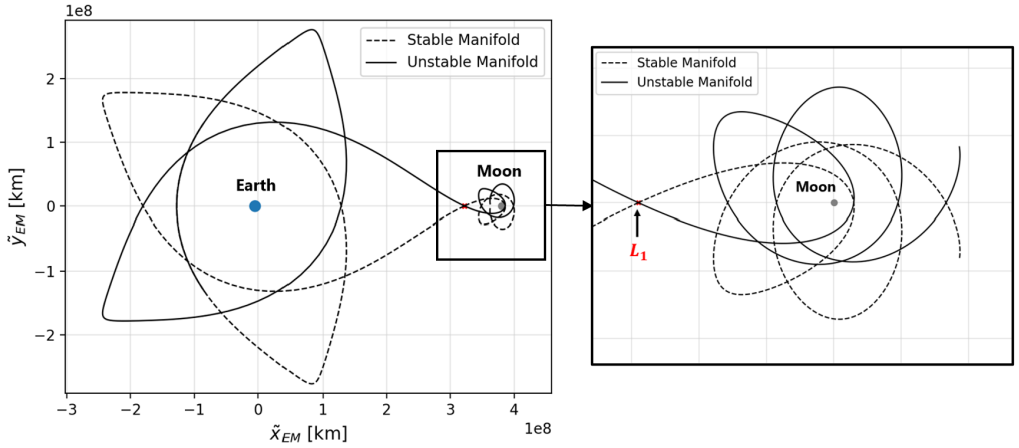

(b) Reproduced plot.

Figure A.1: Stable and Unstable invariant manifolds associated with the Earth-Moon L_1 point.

A.1.2. Frame Transformations

Two different sets of reference frame transformations are used in this thesis: 1. transformations between the planar inertial and CR3BP reference frames, and 2. between the inclined Mars-Moons CR3BP and Sun-Mars CR3BP.

Between CR3BP and Inertial

The transformation from a CR3BP to an inertial frame is verified by plotting Earth's orbit in the heliocentric inertial reference (H), as illustrated in Fig. A.2. Here, the state of Earth in the Sun-Earth (SE) CR3BP frame, $[1-\mu_{SE} \quad 0 \quad 0 \quad 0 \quad 0 \quad 0]^T$, is transformed to the heliocentric inertial frame. The radius of Earth's orbit aligns with the anticipated value of $1.49 \cdot 10^8$ km, forming a perfectly circular trajectory about the Sun. Moreover, the velocity component is tangential to the orbit, exhibiting magnitudes that conform to the expected circular velocity at this altitude, 29.7 km/s. Since the reverse transformation yields the anticipated states of the Sun ($x = -\mu_{SE}$) and Earth ($x = 1-\mu_{SE}$) in the SE CR3BP, the CR3BP to inertial transformation is considered correctly implemented.

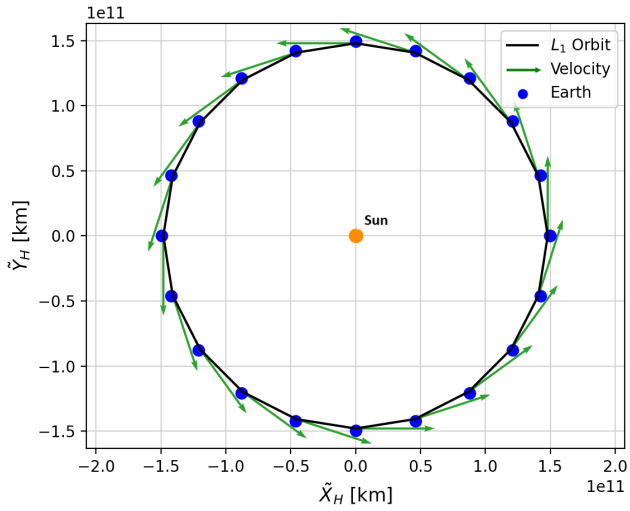

Figure A.2: States of Earth in the heliocentric inertial reference frame (H)

Mars-Moon CR3BP and Sun-Mars CR3BP

The transformation between the Mars-Moon (MM) Circular Restricted Three-Body Problem (CR3BP) and the Sun-Mars (SM) CR3BP involves two intermediate inertial reference frames: a Mars-centered ecliptic frame aligned with the ecliptic plane and the SM CR3BP, and a Mars-centered equatorial frame inclined at 26 deg with respect to the ecliptic. To validate these transformations, the coordinate axes of these frames are visualized in other reference frames.

In Fig. A.3a, the position axes of the Mars-centered ecliptic frame in the heliocentric inertial reference frame are depicted. As intended, their reference axes are parallel, with only the origin translated to the centre of Mars. Similarly, in Fig. A.3b, the position axes of the Mars-Phobos CR3BP are visualized in the Sun-Mars frame, with a longitude of ascending node equal to zero. The orbit is well inclined at 26 deg to the ecliptic, with the x-axis consistently pointing along the Mars-Deimos line and the z-axis being perpendicular to the orbital plane. Consequently, the transformation of the position vectors is deemed accurate.

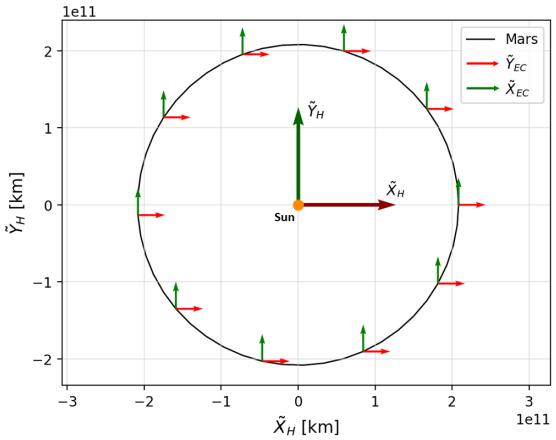

(a) Position axes of the Mars-centered ecliptic frame M_{EC} shown in the heliocentric inertial reference frame.

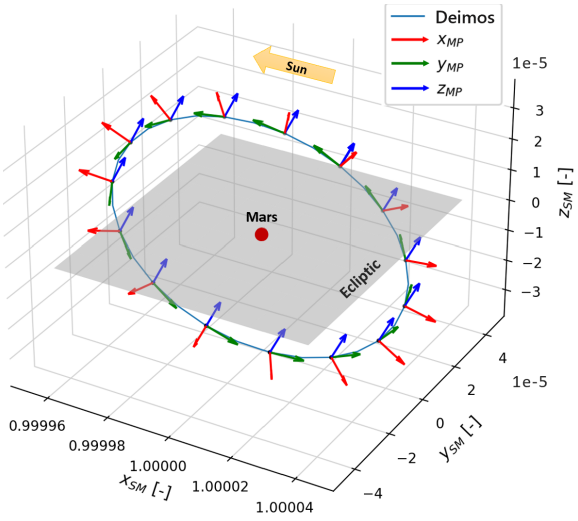

(b) Position axes of MarS-Deimos CR3BP in the Sun-Mars CR3BP reference frame.

Figure A.3: Verification of frame transformation from a Sun-Mars CR3BP to a Mars-Moon CR3BP and vice versa - for position.

While the preceding discussion successfully verifies the transformation of the position vectors, it does not specify whether the velocity components are transformed correctly. To achieve this, an arbitrary initial state in the MD frame is propagated. The same initial state is then transformed into the SM frame and propagated separately in the SM. The states of both these integrated trajectories are then transformed into the other frames; for instance, those integrated in SM are transformed into MD, and those in MD are transformed into SM. Figures A.4b and A.4a show that these trajectories accurately overlap each other. However, since the initial state is defined only in the MD system and later transformed to SM for propagation in SM, this method of verification may not entirely reflect any inaccuracies in the transformation. Nonetheless, considering that the transformation between the SM and MD frames involves intermediate transformations between CR3BP and inertial frames, something that has been verified before, and the fact that the obtained integrated trajectory in the SM frame in Fig. A.4b is inclined as expected, the transformation of the velocity between these frames is considered verified.

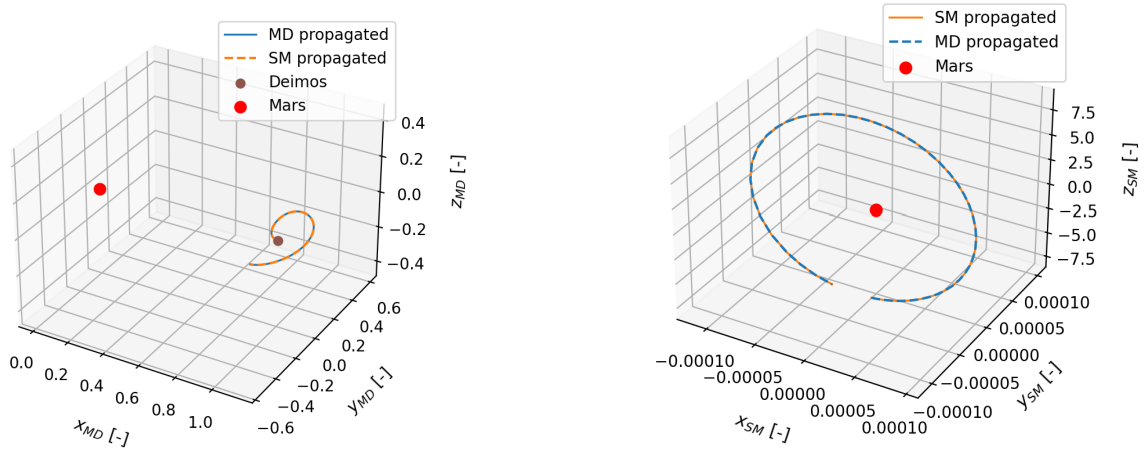

(a) Trajectory shown in the Mars-Deimos system.

(b) Trajectory shown in the Sun-Mars system.

Figure A.4: Verification of the frame transformations between the Sun-Mars and Mars-Deimos CR3BP - for velocity.

Transformation for Fourth-bodies in Mars-moon CR3BP

The motion of a fourth body in the Mars-Moon system can be described by performing three sets of transformations: from a Sun-planet (SP) CR3BP to heliocentric inertial, from heliocentric inertial to Sun-Mars CR3BP, and from Sun-Mars CR3BP to Mars-moon CR3BP. If the perturber is a planet, the state in the Sun-planet CR3BP that undergoes these transformations is $[1-\mu_{SP} \quad 0 \quad 0 \quad 0 \quad 0 \quad 0]^T$, while if it is the Sun, the state taken is $[-\mu_{SP} \quad 0 \quad 0 \quad 0 \quad 0 \quad 0]^T$. Although all the transformation steps required to realize a fourth body's motion in the Mars-Moon system have been successfully verified, as a sanity check, it is checked whether these results align with the commonly used analytical formulation of the Sun's motion in the Earth-Moon CR3BP system for a two-dimensional system (i.e., the Earth, Moon, and Sun all lie on the ecliptic). This equation is given as follows [50]:

$$\hat{\mathbf{S}}(t) = [\cos(\Omega_s t + \Omega_0) \quad -\sin\Omega_s t + \Omega_0 \quad 0] \tag{A.5}$$

where $\hat{\mathbf{S}}$ is the position vector of the Sun with respect to the CR3BP barycenter, Ω_s is the ratio of the synodic lunar period and the sidereal lunar period, t is the non-dimensional time in the respective CR3BP system, and ω_0 is the angle between sun-sail line and the x-axis at $t = 0$. For the Earth-Moon CR3BP, $\Omega_s = 0.9252$.

The result is shown in Fig. A.5, and it is evident that both the solution obtained from Eq. A.5 (labelled as "literature") and the transformations employed in this thesis almost perfectly align

with each other. The small misalignments are attributed to the unknown values of EM CR3BP characteristic parameters used to derive the value of Ω_s, which might not coincide with those used in this thesis.

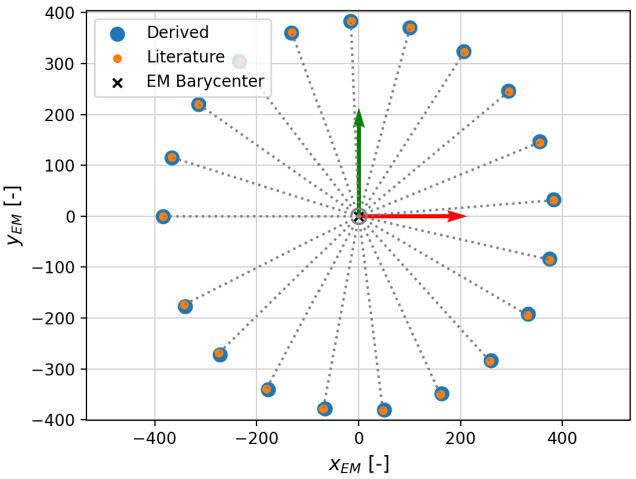

Figure A.5: The motion of the Sun in an Earth-Moon system transformed using the analytical expression using literature [50] and the transformations employed in this thesis (labelled "Derived"). The transformations used in this thesis assume an inclination and raan of 0deg for generating this plot. Dotted lines are the lines joining the EM barycenter and the values obtained from the literature formulations. Green and red arrows are the scaled unit vectors representing the y and x-axis of the EM CR3BP frame, respectively.

A.1.3. Solar sail Acceleration

The inclusion of solar sail acceleration in the dynamics is achieved by simply introducing an additional acceleration term to Eq. A.1. The specific formulation of sail acceleration depends on whether the dynamics are being propagated within a Sun-planet CR3BP or a Mars-moon CR3BP, as detailed in Chapter 2. To verify the accurate implementation of sail acceleration in a CR3BP system, a sail-perturbed halo orbit is reproduced about the SE L_1 artificial equilibrium point (AEP). This is done for a sail lightness number of 0.05 and is compared with data provided for its literature counterpart [25].

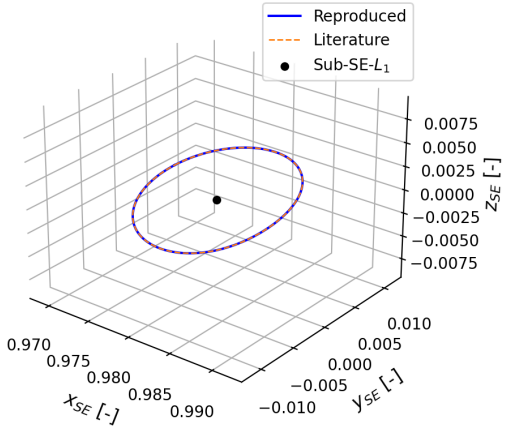

(a) Solar sail halo orbit about the Sun-Earth Sub-L_1 point. The dashed orange curve corresponds to the reference orbit, while the solid dashed curve is the reproduced halo orbit.

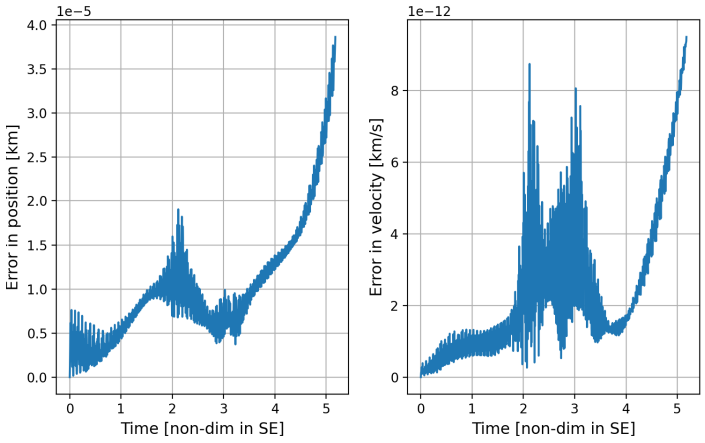

(b) Position and velocity error computed against the reference solution.

Figure A.6: Solar sail model verification using the data provided by the author of Ref. [25], Heiligers, for a lightness number of 0.05.

AEPs, similar to classical equilibrium points, represent locations where a stationary solar sail experiences zero net acceleration in a CR3BP. The SE L_1 AEP is located closer to the Sun at position $(0.98040998, 0, 0)$ for $\beta = 0.05$ and a cone angle of zero degrees. The propagated halo orbit also considers a zero-degree cone angle. Figure A.6a shows a comparison between the reproduced and original halo orbits, both of which appear to overlap perfectly. The errors between these orbits, depicted in Fig. A.6b, are deemed sufficiently low to verify the accurate implementation of the sail acceleration. It is to be noted that these errors are originally computed in the SE CR3BP system, where the maximum errors are on the order of 10^{-13}, limited only by numerical precision.

Given that the primary difference in formulating sail acceleration for Mars-moon involves the need for a frame transformation to factor in the Sun's position - a step verified in the preceding section - its verification in the SE system can be extended to the Mars-moon system too.

A.1.4. Fourth-body Perturbation

To verify the fourth-body perturbations, their magnitude and directions are looked at separately. For ease of explanation, the formulation of the fourth-body perturbation is restated:

$$\mathbf{a_4} = \frac{\partial U_4}{\partial r_4} \tag{A.6}$$

where,

$$U_4 = \mu_4 \left(\frac{1}{r_{3,4}} - \frac{\mathbf{r} \cdot \mathbf{r_4}}{r_4^3} \right) \tag{A.7}$$

where, $\mathbf{r_4}$ is the position vector from the barycenter to the fourth body, $\mathbf{r}_{3,4}$ is the position vector from the particle (spacecraft) to the fourth body which is given as $\mathbf{r}_{3,4} = \mathbf{r}_4 - \mathbf{r}$, and μ_4 is the dimensionless gravitational parameter of the fourth body with respect to the specified CR3BP system. The fourth-body perturbing acceleration is a relative acceleration acting on a particle in a CR3BP frame. It comprises of two separate components: 1. the absolute gravitational acceleration acting on the particle by the fourth body ($\frac{\mu_4}{r_{3,4}}$) and 2. the absolute acceleration between the primaries and the fourth-body ($\mu_4 \frac{\mathbf{r} \cdot \mathbf{r_4}}{r_4^3}$).

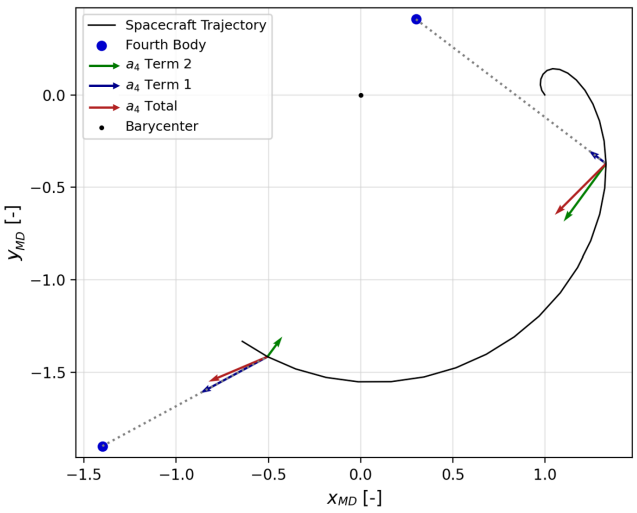

Figure A.7: Separate components of the fourth-body perturbation plotted in a Mars-Deimos CR3BP frame, assuming that Deimos' orbit lies in the ecliptic. The green solid arrow corresponds to acceleration by the fourth body on the particle, the blue arrow is the absolute acceleration between the CR3BP system and the perturber, and the red arrow indicates the total relative acceleration experienced by the particle. The dashed line joins the perturber and the particle at a certain instance along its trajectory.

To verify the direction of the acceleration, these components are computed along an arbitrary trajectory in a Mars-Deimos CR3BP system. The results are visualized in Fig. A.7. As expected, the first component aligns with the line connecting the fourth body and the particle - pointing towards the perturber, while the second component is parallel to the line joining the CR3BP barycenter and the fourth body - pointing towards the barycenter.
To verify the magnitude of this relative perturbation, a plot generated by Kardec and Bertachini [64], illustrating the perturbation magnitudes by the Sun in a Mars-Phobos CR3BP, is reproduced. The original and replicated plots are shown in Fig. A.8. It is to be noted that these plots specifically pertain to a particular instance in time, i.e., for a specific orientation of the Sun relative to the CR3BP frame. It is also assumed that the moon's orbit lies in the ecliptic.

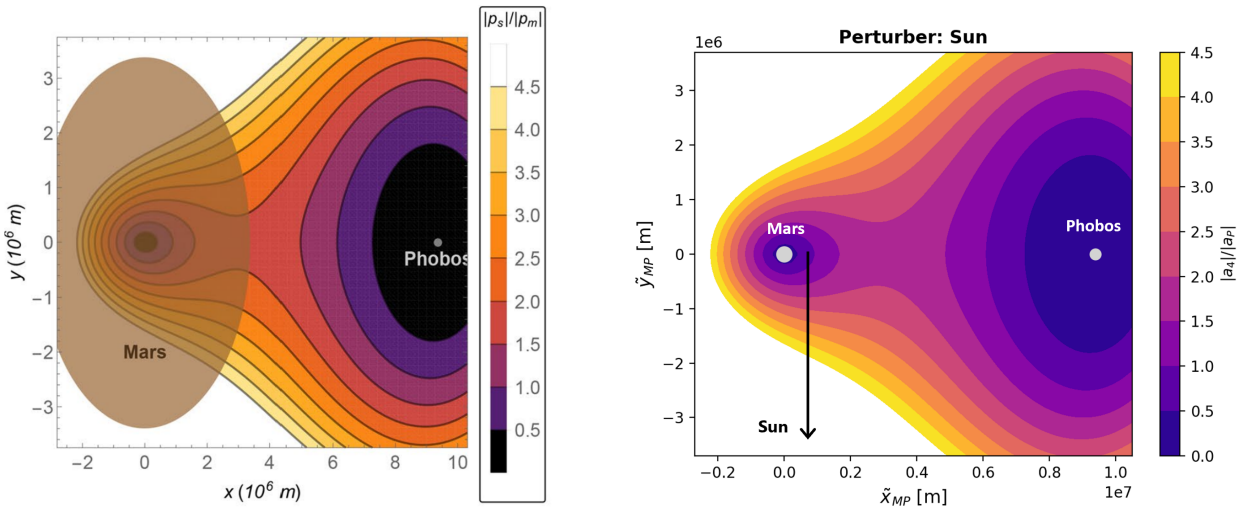

(a) The plot found in the reference [64].

(b) The reproduced plot.

Figure A.8: Verification of the fourth-body perturbation magnitude. The perturber is the Sun in a Mars-Phobos CR3BP reference frame planar to the ecliptic. This image is a snapshot at a particular instance in time for a specific orientation of the Sun. The perturbation magnitude is given as the ratio of the fourth-body perturbation due to the Sun ($|\mathbf{p_s}|$ or $|\mathbf{a_4}|$) and the point-mass gravitational acceleration of Phobos ($|\mathbf{p_m}|$ or $|\mathbf{a_p}|$).

A.1.5. J_2 Perturbation

The J_2 perturbations are verified by computing the displacement in the positions of the Mars-Phobos colinear Lagrange points $L_{1,2}$ under the perturbed Mars and Phobos J_2 environment and comparing them against literature. The new displaced colinear Lagrange points are computed by simply adding additional perturbation terms, due to both the oblateness of Mars and Phobos, to Eq. A.3 followed by the application of the Newton-Raphson method. It was found that both L_1 and L_2 are displaced by 365.45m farther away from the moon relative to their original location. This value closely aligns with the displacement of 365m calculated by Zamaro [65].

A.2. PSOPT

The optimal control problem (OCP) in this study is solved using the direct pseudospectral method implemented in the open-source software package PSOPT. Past literature, including studies such as references [48, 49, 50, 66], have demonstrated PSOPT's capability to successfully converge to local minima for similar dynamical models, objectives, and constraints. As such, no separate verification is necessary for the same.

However, since a direct pseudospectral method outputs the state and control variables at discrete time intervals, ensuring valid results only at these nodes, it is necessary to validate whether the output remains valid for a continuously integrated solution. This validation is performed by rein-

tegrating the states using a control law derived by interpolating the optimal control obtained from PSOPT. The interpolation is performed using a cubic spline, and the EoM are solved with a variable step size variable order implicit integrator LSODA, with a relative and absolute tolerance of 10^{-11}. If the reintegrated solution is sufficiently accurate, i.e., it satisfies the constraints, it is considered to be valid. This is performed in two ways for each leg:

1. **Linkage constraint:** This involves checking whether the linkage constraint between two interplanetary phases is satisfied. The procedure includes propagating the states forward from the departure state in the interplanetary phase and propagating the states backwards in time from the arrival state. The Euclidean error in position and velocity at the linkage is then computed. As an example, for leg 2, the state at the end of the spiral escape trajectory at the Martian SOI is propagated forward in time in the Sun-Mars CR3BP, while the states from Sun-Earth L_2 are propagated backwards.
2. **Arrival boundary constraint:** This method involves fully propagating the interplanetary trajectory from the departure to the arrival state to check whether it satisfies the arrival boundary constraint. For instance, the integration is performed from the state at the Martian SOI to the SE-L_2 for leg 2.

The results from reintegration are presented in Table A.3. Given the large interplanetary distance between Earth and Mars, 10^8km, these errors are considered sufficiently small and can be corrected through small manoeuvres along the trajectory. Hence, the PSOPT solution is deemed valid.

Table A.3: Discontinuities at the linkages and arrival states for reintegrated trajectories for both legs. Those at linkages are obtained by forward and backward propagation of two separate phases while those at arrival are produced by full integration of the interplanetary trajectory. The non-dim discontinuity at arrival for leg 1 is computed in the Sun-Mars frame while the rest is in Sun-Earth.

	Discontinuity location	Δr		Δv	
		[non-dim]	[km]	[non-dim]	[km/s]
Leg 1	Linkage	$3.24 \cdot 10^{-5}$ SE	4845.11	$3.33 \cdot 10^{-5}$ SE	$2.11 \cdot 10^{-4}$
	Arrival	$1.13 \cdot 10^{-4}$ SM	25845.82	$3.32 \cdot 10^{-4}$ SM	$1.03 \cdot 10^{-2}$
Leg 2	Linkage	$1.61 \cdot 10^{-4}$ SE	24117.37	$7.21 \cdot 10^{-5}$ SE	$3.11 \cdot 10^{-3}$
	Arrival	$3.06 \cdot 10^{-4}$ SE	45829.28	$3.51 \cdot 10^{-4}$ SE	$1.9 \cdot 10^{-2}$

The position and velocity errors between the reintegrated solution and the PSOPT results, plotted as a function of time, are shown in Fig. A.9 for leg 1. Here, Fig. A.9a represents the forward propagated trajectory in the SE system up to the linkage point, while Fig. A.9b corresponds to the backward propagated trajectory in the SM system. Notably, a significant portion of the error is contributed by the backwards propagated trajectory, characterized by a sharp spike to errors exceeding 10^3 km for position and 10^{-3} km/s for velocity. This phenomenon can be attributed to the rather irregular control profile depicted in Fig. A.10 (specifically shown for leg 1) at the end of the Sun-Mars phase, leading to less accurate interpolation between the last few nodes. This discrepancy is a result of the boundary constraint at the end of the SM phase, requiring the state and control to be identical to those at the start of the spiral capture trajectory to Deimos within the Martian SOI that has been computed separately as part of the initial guess and not optimized along with the interplanetary phases using PSOPT. On the other hand, errors in the SE phase are an order of magnitude lower, showing a consistent increase owing to its comparatively smooth control profile as seen in Fig. A.10. The same observations were made for leg 2. Additionally, errors for full integration (at arrival state) are larger than those at the linkage solely due to the accumulation of errors over the two phases.

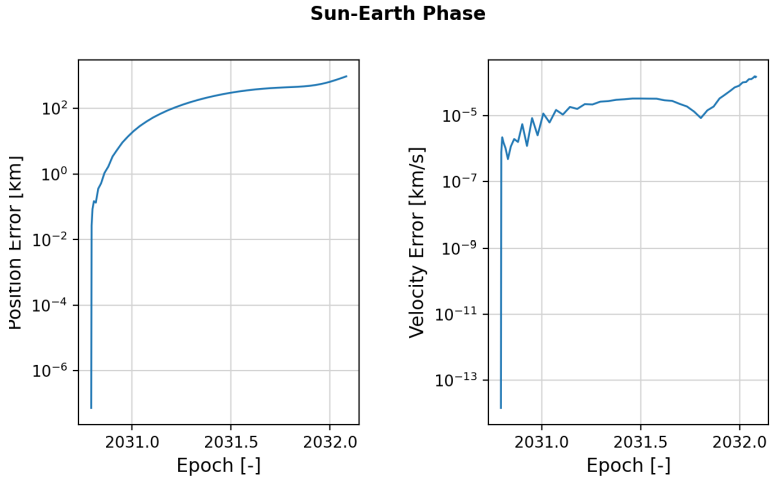

(a) Trajectory propagated forwards in time in the Sun-Earth system - phase 1.

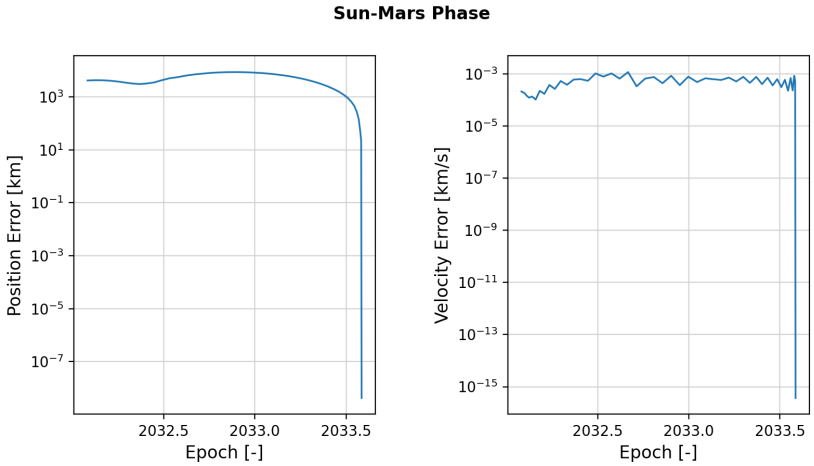

(b) Trajectory propagated backwards in time in the Sun-Mars system - phase 2.

Figure A.9: Norm of position and velocity errors between the PSOPT optimal results and reintegrated trajectory for leg 1.

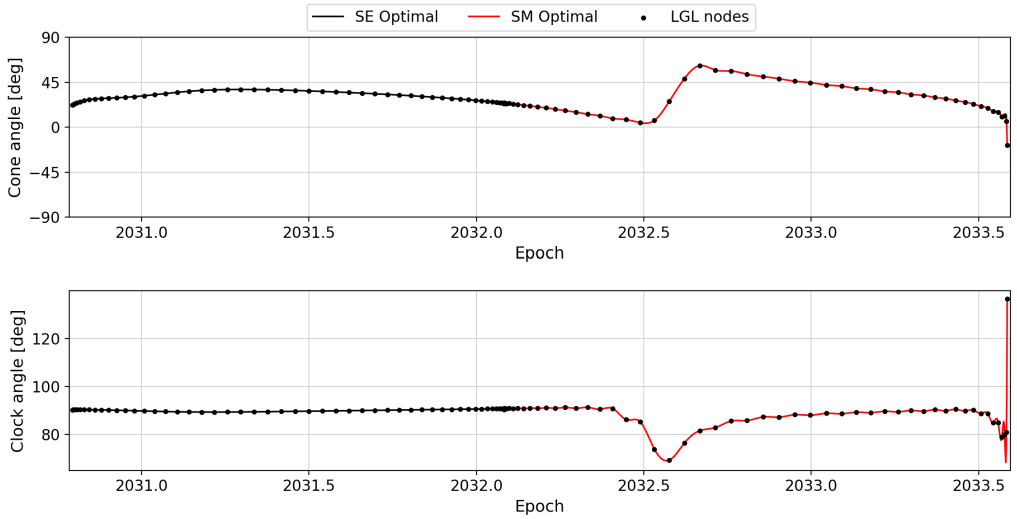

Figure A.10: Interpolated control profile for the interplanetary phases of leg 1 along with the Legendre-Gauss-Lobatto (LGL) nodes displayed using black dots.

The integration error can be reduced by considering a finer mesh grid for both interplanetary

phases. Currently, the mesh was refined from 50, 80 to 100 nodes for the entire interplanetary trajectory (50 for each phase) and was solved using a tolerance of 10^{-6}. However, further refinement was not possible given the 32-bit build of PSOPT, which was constantly running out of the allocated memory. Although it is feasible to modify the package to a 64-bit build, this process demands a substantial amount of time and was deemed unimportant for the current study, which primarily aimed to design a preliminary trajectory.

B Numerical Techniques for Initial Guess Generation

This appendix chapter outlines the settings used for various numerical techniques during the generation of initial guesses. The chapter is divided into two sections: Section B.1 focuses on selecting a suitable integration scheme, and Section B.2 delves into the tuning procedure for the differential evolution (DE) algorithm and presents the final DE parameters used in this thesis.

B.1. Integrator Selection

While PSOPT employs its own integrator as part of the pseudospectral method to solve the OCP, a separate integrator is required to generate initial guesses for PSOPT. Given that the process of generating initial guesses involves a computationally demanding Monte Carlo analysis and differential evolution, selecting an integrator becomes crucial to ensure computational feasibility. This, however, should not come at the cost of the solution's accuracy.

To select an appropriate integrator, various integration schemes are used to propagate the EoM in two distinct systems: a Sun-Planet CR3BP and a Mars-Moon CR3BP system. Considering both dynamical models ensures that the non-autonomy of a Mars-Moon system, resulting from the varying position of the Sun, is also considered during integrator selection. The resulting position and velocity at the end of the propagation are compared to a benchmark solution, and a subsequent trade-off is conducted between the integrator accuracy and computational time to decide on a suitable integrator for the study. Higher weightage is given to integrators that require less time to propagate the initial value problem.

The analysis considers integration schemes available in the open-source Python library `scipy` [67]. These include:

- `RK45`: Single-step, explicit and variable step-size Rung-Kutta integrator of order 5(4).
- `DOP853`: Single-step, explicit and variable step-size Runge-Kutta integrator of order 8(5,3).
- `LSODA`: Multi-step, variable step-size, variable order and implicit integrator that switches between the Adam methods for non-stiff problems and backward differentiation formulas (BDF) for stiff problems [68].

For each integration scheme under consideration, four values of tolerance are considered: 10^{-5}, 10^{-7}, 10^{-9} and 10^{-11}.

While several other integrators, such as multi-step Adams-Bashforth-Moulton (ABM), explicit Runge-Kutta-Fehlberg of different orders, and others exist, due to their unavailability in `scipy`, they were not considered. Nonetheless, the chosen schemes do holistically represent most of the commonly used integrator categories for trajectory design.

The integrator employed to generate the benchmark solution is DOP853 with a relative and absolute tolerance of 10^{-14}. In the case of the Sun-Planet scenario, a sail-perturbed manifold emanating from the SE-L_2 point with a constant sail attitude of 30deg cone angle and 30deg clock angle is propagated for four years. This prolonged trajectory ensures that it extends just beyond the Martian orbit, thereby accounting for the accumulation of truncation error during integrator selection,

given the substantial propagation time. For the Mars-Deimos system, a similar constant attitude sail-perturbed trajectory is propagated from the MD-L_1 for 100 revolutions of Deimos about Mars, roughly equivalent to about 120 days.

While no specific CPU time requirement was stipulated for the integrator due to the uncertainty in the number of runs during the tuning of the differential evolution algorithm, a requirement on the position and velocity error was indeed considered. Keeping in mind the minimum required linkage position and velocity error of $\Delta r \leq 10^{-3}$ and $\Delta v \leq 10^{-2}$ in a CR3BP frame (refer to the article in Chapter 2), any integrator with errors two to three magnitudes below this threshold is deemed suitable. Once the accuracy requirement is satisfied, the scheme with the lowest computational time is chosen. The results for both the Sun-Earth and Mars-Deimos systems are presented in Figs. B.1 and B.2, respectively. Based on these outcomes, the integration scheme selected for generating the initial guesses is LSODA, with 10^{-9} as the relative and absolute tolerance. It is to be noted that the error profiles of all the integrators are dominated by truncation errors.

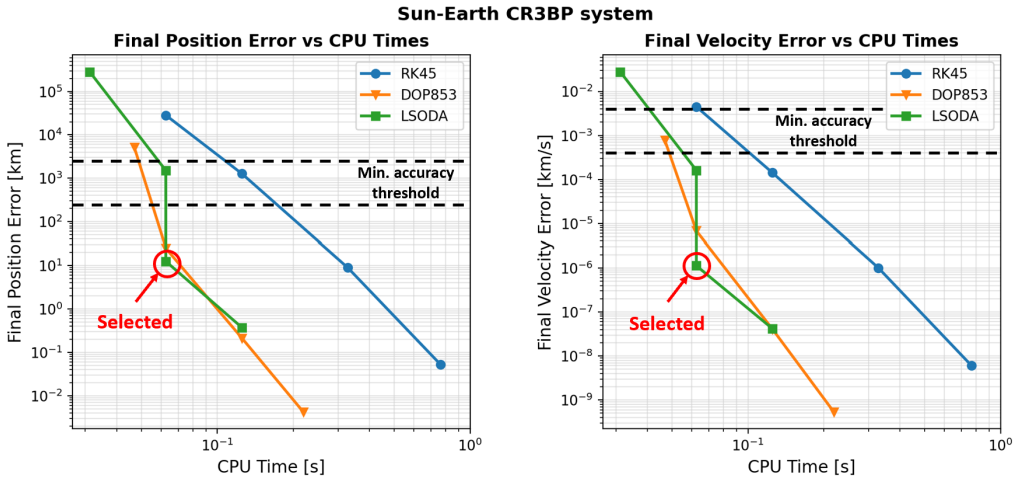

Figure B.1: Position and velocity error for various integrators against the CPU time for the Sun-Earth case. For each integrator, the position and velocity errors are proportional to the integrator tolerance - the largest errors are associated with the largest tolerance (10^{-5}) and the smallest errors with the smallest tolerance (10^{-11}).

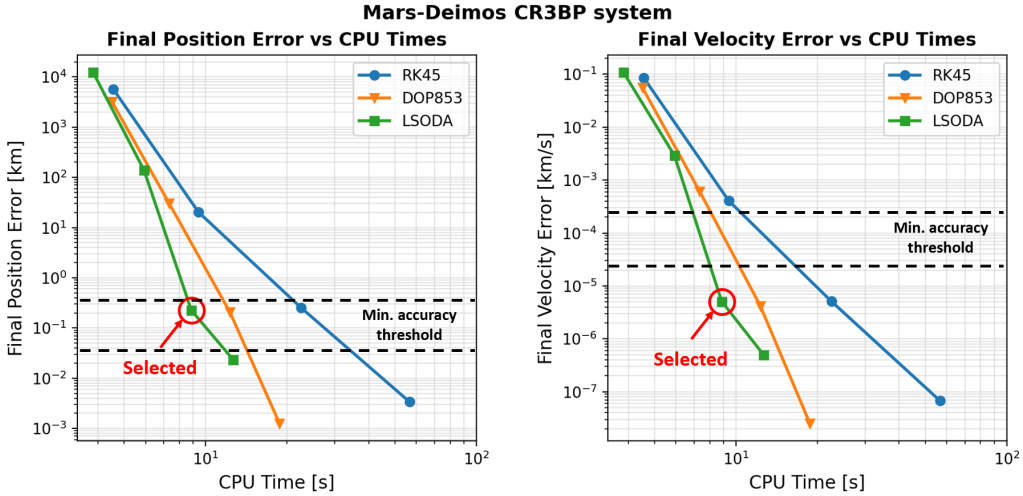

Figure B.2: Position and velocity error for various integrators against the CPU time for the Mars-Deimos case. For each integrator, the position and velocity errors are proportional to the integrator tolerance - the largest errors are associated with the largest tolerance (10^{-5}) and the smallest errors with the smallest tolerance (10^{-11}).

B.2. Differential Evolution Tuning

Differential evolution (DE) is a metaheuristic global optimization algorithm belonging to the class of evolutionary algorithms that are inspired by Darwin's theory of evolution. The algorithm begins with randomly initialising a population of candidate solutions (design variables). Through iterative processes involving mutation, crossover, and selection, the population evolves until it either converges to a solution within a specified tolerance limit or reaches the maximum limit set for the number of generations. In the current study, both these criteria were used as termination conditions, with a tolerance set to 0.01, and the maximum number of generations adjusted during the tuning process. The particular implementation of the differential evolution part of the Python library `scipy` as `scipy.optimize.differential_evolution` method was used whilst also employing multiprocessing.

The differential evolution algorithm relies on parameters such as the mutation rate, crossover ratio (CR), population size (N_p), and seed to seek the global optimum. The values chosen for these parameters are problem-specific and need to be tuned for optimal performance. In this thesis, parameters considered for tuning were the crossover ratio, population size, seed, and weights of the objective functions. The mutation rate was assumed to vary randomly within the range $(0.5, 1)$ to potentially speed up the convergence and was not included in the tuning process. For other parameters, like the crossover ratio and population sizes, the values considered for tuning were based on rules of thumb provided by Price et al. [69] for highly non-convex problems, which based on the Monte Carlo analysis was the nature of the problem at hand. Population sizes were chosen to be equal to or greater than ten times the number of design variables (seven), with values of 70, 105, and 140. Crossover ratios were set to mid-to-high values, specifically 0.4, 0.6, 0.8, and 0.9.

Among the weights w_1, w_2, w_3, and w_4 in the objective functions, Eqs. 32 and 35 in the article, only w_2 and w_4 were tuned, with values of 100 and 1000 used for tuning. This decision was based on the relative magnitudes of the expected times-of-flight values (approximately 10^3 to 10^2) for leg 1 and the duration of stay associated with the objective for leg 2, in comparison to the position and velocity errors. The position and velocity errors were considered in the Sun-Earth dimensional units, expected to have values on the order of magnitudes greater than 10^5 and 10^{-1}, respectively. For the same reason, the weights w_1 and w_3, acting as the scaling factors for velocity, were kept constant at 5000000, which is the ratio between the maximum position and velocity error requirements ($1.5 \cdot 10^5$ and 0.3) in the inertial frame. This ensures that each variable being minimized is treated with roughly the same importance by the algorithm.

Given the computationally demanding problem, particularly due to the spiral trajectories, instead of conducting a grid search, the DE algorithm was tuned by varying one set of parameters at a time. First, the parameters N_p, seed, and weights were fixed at 70, 56587, and 1000, respectively, with only the values of CR varied in each run performed for 100 generations, as illustrated in Fig. B.3a. These results were then utilized to fix the value for CR while varying the remaining parameters. The convergence of the fitness for different population sizes and seeds is shown in Figs. B.3b and B.3c, respectively. Subsequently, for the selected values of CR, N_p, and seed, the weights were tuned for 200 generations. Finally, with the obtained set of tuned parameters, an additional 100 generations were performed (300 in total), where the solution for leg 1 converged within the set tolerance, while that for leg 2 did not but was still considered sufficiently optimal for an initial guess. Table B.1 lists the values of parameters taken by the tuned DE algorithm.

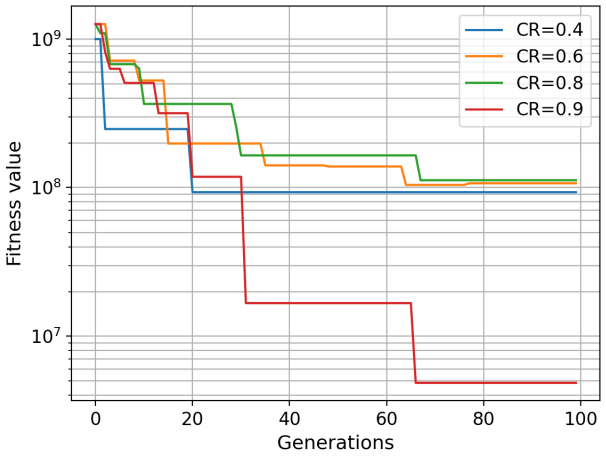

(a) Crossover ratio. $CR = 0.9$ found the best solution.

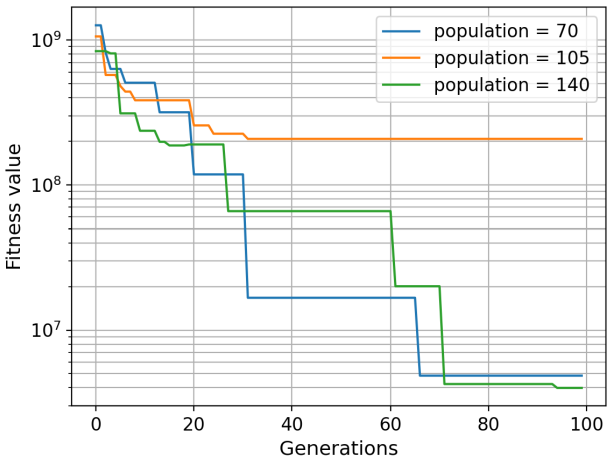

(b) Population sizes. $N_p = 140$ is the best.

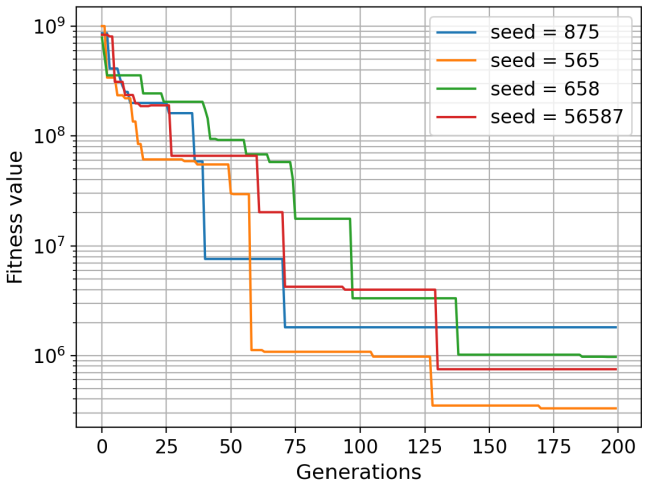

(c) Different seeds. Seed 565 is the most optimal.

Figure B.3: Convergence of the fitness over the generations for different values of the parameters - shown for leg 1.

Table B.1: Parameters for the tuned differential evolution algorithm for both the legs of the mission.

	N_p	CR	Seed	w_2	w_4
Leg 1	140	0.9	565	100	-
Leg 2	70	0.9	56587	-	1000

C Moon to Moon Transfer

This section presents the results obtained from a preliminary analysis for devising a transfer between Phobos and Deimos using a solar sail. Similar to the transfers to Deimos, an ideal sail with a lightness number of 0.05 is assumed, and trajectories are established in a patched CR3BP model. The orbit of Phobos is considered to be planar to that of Deimos, i.e. it is also inclined at 26 deg to the ecliptic with a raan of 83 deg. The characteristic parameters taken for Phobos along with its initial phase angle (ϕ_0), with respect to the x-axis of the Mars-centered equatorial frame (M_E), is summarized in Table C.1.

Table C.1: Characteristic parameters of the Mars-Phobos CR3BP system and Phobos' initial phase angle. Based on the values provided by NASA/JPL's Solar System Dynamics group [70].

Parameters	μ [-]	λ [km]	τ [s]	ϕ_0 [deg]
Values	$1.611 \cdot 10^{-8}$	$9.468 \cdot 10^{3}$	$4.452 \cdot 10^{3}$	172.3214

Here, heteroclinic-like connections are sought between the Mars-Deimos (MD) L_1 and Mars-Phobos (MP) L_2 Lagrange points by minimizing the position and velocity errors at the linkages between the solar-sail perturbed invariant manifolds originating from these points. Two different control laws are employed to achieve this: one with a sail featuring fixed cone and clock angles for both the MD and MP phases, and the other with a sail following the locally optimal steering law, maximizing the rate of change of the Jacobi constant (JC). Similar to the approach outlined in the article, the linkage errors $\Delta r \leq 10^{-3}$ and $\Delta v \leq 10^{-2}$ in the Mars-Phobos system are regarded as criteria to achieve a satisfactory result that ensures the feasibility of obtaining continuous transfers between the moons.

A Monte Carlo analysis was conducted for both control laws for a transfer from MD-L_1 to MP-L_2 involving an unstable manifold from Deimos and a stable manifold from Phobos. The results are illustrated in Fig. C.1a for fixed control and Fig. C.1b for locally optimal control, where the relation between the position error, velocity error and difference in Jacobi constant in the Sun-Mars frame (ΔJC_{SM}) at the linkage is shown. It's worth noting that for fixed control, the cone and clock angles of stable and unstable manifolds may not necessarily be the same. From the figures, it was concluded that even with roughly 33,000 samples, none of the data points met both the required Δr and Δv criteria.

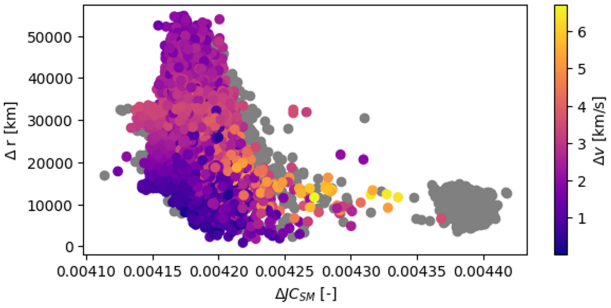

(a) Using fixed cone and clock angles. The greyed-out points represent the designs that either impacted the moons or Mars.

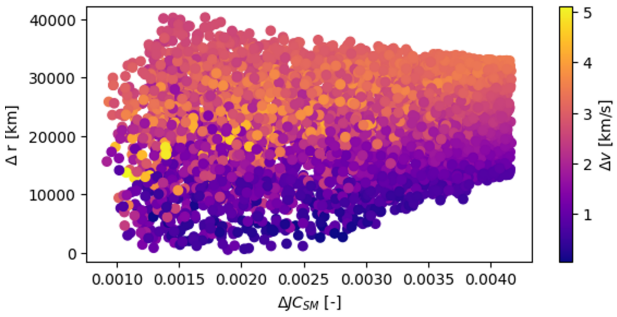

(b) Using locally optimal steering law.

Figure C.1: Results of Monte Carlo analysis showing a scatter plot for the position error, velocity error and difference in the Jacobi constant computed in the Sun-Mars frame at the linkages.

To further evaluate the feasibility of these control laws in producing trajectories that meet the linkage requirements, a map was generated to illustrate the general relationship between Δr, Δv, and ΔJC as depicted in Fig. C.2. It was generated by calculating the maximum feasible value of ΔJC in the Sun-Mars frame for various combinations of Δr and Δv. The plot reveals that to meet the requirements, a ΔJC of less than $2 \cdot 10^{-4}$ is essential, a criterion that neither of the implemented control laws satisfies in Fig. C.1. Although the locally optimal control law narrows the gap between the Jacobi constants of the two manifolds, it falls short of achieving the desired output.

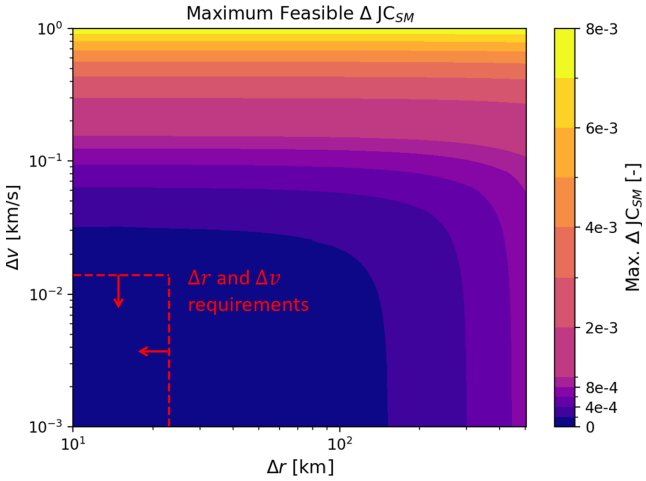

Figure C.2: Relation between position errors, velocity errors and maximum feasible difference in Jacobi constants.

The impracticality of achieving the desired outcome is further evident in the trajectory depicted in Fig. C.3 plotted, in the M_E frame, for the solution with adequately low position and velocity errors for the locally optimal steering. It is evident that the current steering law alone cannot close the energy gap, and requires either the use of alternative control laws or a series of impulsive maneuvers.

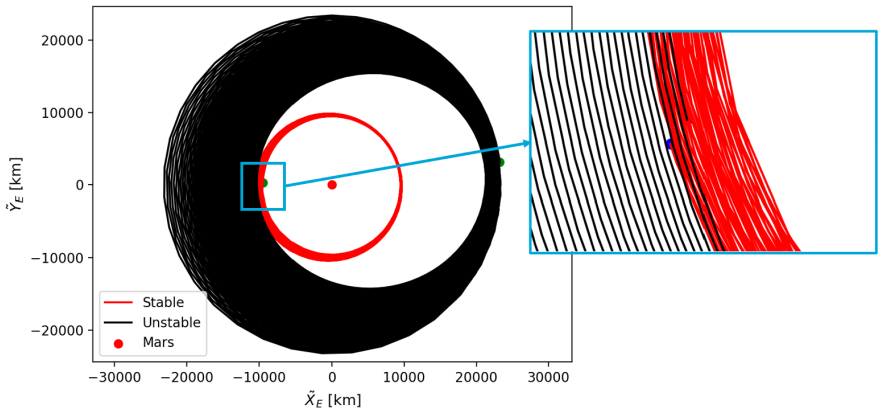

Figure C.3: Trajectory of the solution with sufficiently low linkage errors employing the locally optimal steering for a Deimos to Phobos transfer. The zoomed-in image shows the end state of the stable and unstable manifold at the linkage condition. It is plotted in the Mars-centered equatorial reference frame.

D Sensitivity of the manifold distance parameter

This chapter discusses the sensitivity of the distance parameter ϵ, which defines the magnitude by which the state at the Lagrange points is perturbed in the direction of the stable or unstable eigenvectors to ride along their respective manifolds. This application of ϵ for the computation of the initial state is shown by restating the following equation:

$$\mathbf{x}_{0,s} = \mathbf{x} \pm \epsilon \mathbf{v}_s, \qquad \mathbf{x}_{0,u} = \mathbf{x} \pm \epsilon \mathbf{v}_u \tag{D.1}$$

where $\mathbf{x}_{0,s}$ and $\mathbf{x}_{0,u}$ are the initial perturbed state associated with the stable and unstable manifolds for the eigenvectors $\mathbf{v}_s$ and $\mathbf{v}_u$, respectively. The signs ($\pm$) in the Eq. (D.1) depict the interior or exterior branches of the manifold. An interior branch is the one that moves towards the second primary while an exterior branch moves away.

Typically, the chosen value for ϵ falls within the range of 10^{-4} to 10^{-6} [46]. A smaller ϵ value results in a solution that closely follows the invariant manifolds associated with the Lagrange point. Generally, for classical manifolds, the states of the manifolds propagated using this linear approximation for different values of ϵ between 10^{-4} and 10^{-6} is consistent. The only primary distinction lying in the fact that those propagated with smaller values evolve more slowly with time, better approximating the manifolds, as illustrated in Fig. D.1 for both branches of the ballistic unstable manifolds (zero force due to SRP) from the sub-SE-L_1 point (refer to Section A.1.3) for a solar sail with a lightness number of 0.01.

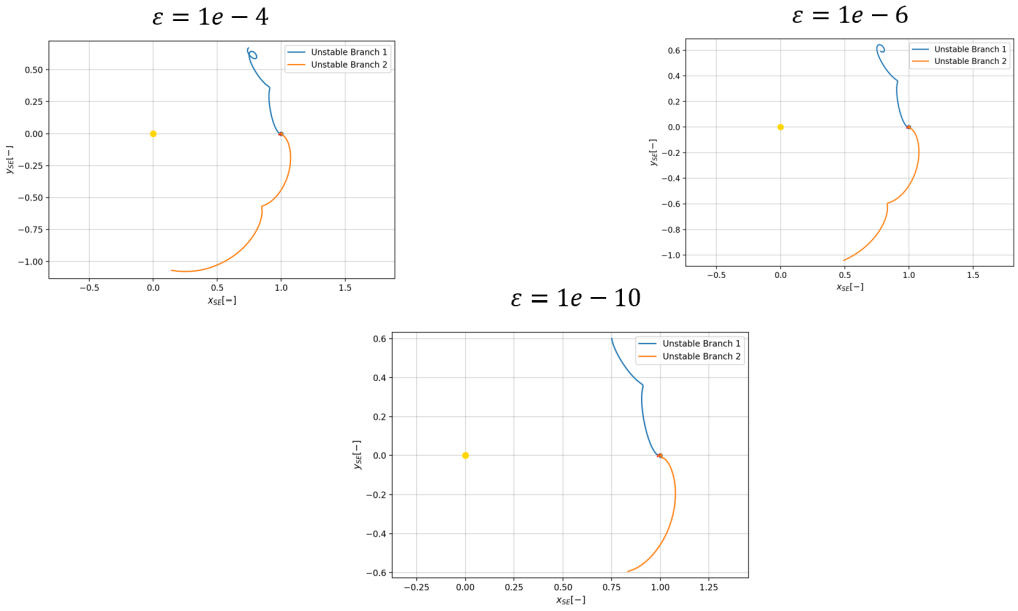

Figure D.1: Classical (ballistic) one-dimensional invariant unstable manifolds propagated for different distance parameters (10^{-4}, 10^{-6} and 10^{-10}) from the sub-L_1 point of the Sun-Earth system for a solar sail with lightness number 0.01. Unstable branch 1 (in blue) is the exterior branch while unstable branch 2 (in orange) is the interior branch. The yellow dot is the Sun.

However, while reproducing the sail-perturbed manifolds generated by Farrés et al. [71] from the same sub-L_1 point for a solar sail with a lightness number of 0.01 and cone angle of -20deg, it was noted that trajectories produced with different distance parameters were strikingly different. This can be observed in Fig. D.2, where four different values of distance parameters are shown, along with a case where the lightness number of the solar sail is zero (ballistic). Here it is seen that as the value of the distance parameter increases, both the branches of the unstable manifolds gradually end up overlapping. None of the past literature explicitly mention this behaviour. Note that although these figures specifically show only the unstable manifolds of a particular Lagrange point in the SE system, similar behaviour was noticed for stable manifolds and other colinear Lagrange points in different CR3BP systems.

This observed behaviour is attributed to the fact that smaller values of the distance parameter result in initial states starting very close to the Lagrange point. Consequently, the acceleration acting on the particle, solely due to the accelerations in the CR3BP, is much smaller than the perturbing acceleration by the sail. This leads to a significant influence on the directions of both branches, causing them to follow in the same direction. This is further supported by the similarity observed between the case with the lowest distance parameter ($\epsilon = 10^{-4}$) and the ballistic case ($\beta = 0$), where the particle starts at a much further distance from the sub-L_1 point, leading to the total acceleration experienced by it being less dominated by the sail.

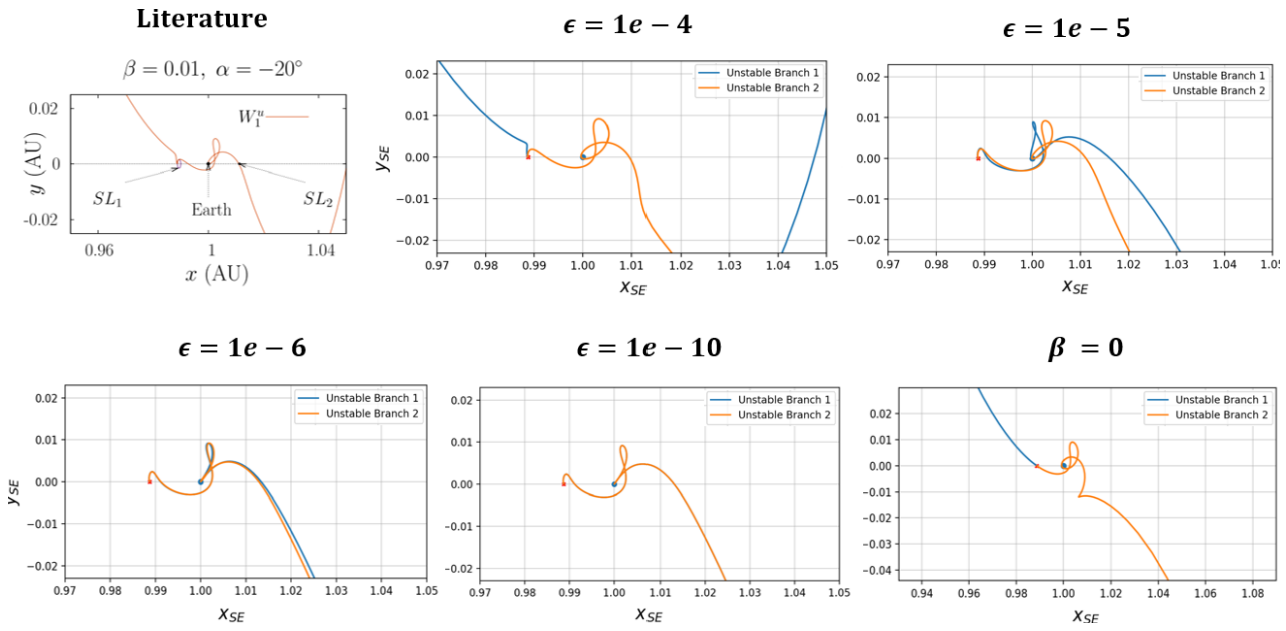

Figure D.2: Exterior (unstable branch 1 in blue) and interior (unstable branch 2 in orange) unstable branches plotted from the SE sub-L_1 point for $\beta = 0.01$. The case labelled "Literature" corresponds to the plot obtained from reference [71] for $\epsilon = 10^{-4}$ with a cone angle of -20deg. Additionally, $\epsilon = 10^{-4}$, 10^{-5}, 10^{-6} and 10^{-4} for the same cone angle are also shown. The case labelled "$\beta = 0$" corresponds to the ballistic case. The blue dot is the Earth.

Therefore, the ambiguity in selecting an appropriate distance parameter can be solved by considering it as another design variable during the initial guess generation. However, to avoid increasing the computational effort, the current study adopts a fixed value for the distance parameter, i.e., $\epsilon = 10^{-4}$. This choice is based on the observation that, for both SE-L_2 and MD-L_1, this value results in branches that move away from each other, similar to the scenario depicted in Fig. D.2, providing two distinct choices for manifolds for obtaining the initial guess. For the final application, among the two branches, the exterior branches - those that move away from the secondary - were chosen for both the SE and MD systems. Additionally, it was reasoned that if this particular value of the distance parameter cannot achieve position and velocity errors between the manifolds below the

specified requirements, a different value of the distance parameter could be employed; however, this was not found to be necessary.

E Additional Plots

This appendix chapter presents relevant additional plots that complement certain arguments mentioned in the journal article.

Periodicity of the fourth-body perturbations

Figure E.1 shows different fourth body perturbing accelerations normalized with Phobos' point mass gravity at an arbitrary point in the Mars-Phobos system. It is evident that all the perturbations exhibit periodicity within a timeframe of less than 3 years, forming the basis for the perturbation analysis conducted in this paper.

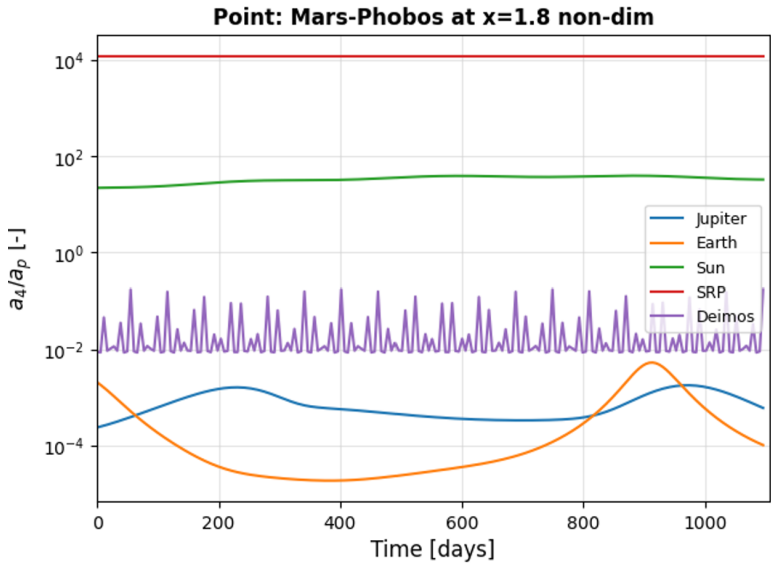

Figure E.1: Perturbations in gravitational acceleration, normalized against the Phobos' point mass gravity, at an arbitrary point (x = 1.8) within the Mars-Phobos CR3BP system, observed from January 1, 2030, to January 1, 2033.

Length of the ballistic segment

During the generation of the initial guesses for the spiral trajectory, a short ballistic segment was introduced to prevent immediate impacts with Deimos as soon as the sail departs from the Mars-Deimos L_1 point. Given the short orbital period of Deimos, there are multiple instances in each orbit where an immediate powered flight, depending on the relative orientation of the Sun and the solar sail, might result in an impact with the moon. Therefore, the addition of a ballistic segment is preferred; it ensures that the spacecraft moves sufficiently away from the moon before initiating powered flight. However, for this the ballistic flight should be long enough, requiring a grid search to identify the appropriate time of flight (ToF) for the ballistic segment.

The grid search was performed with two varying parameters: ballistic ToFs and the location of Mars in its orbit around the Sun. The reason for selecting Mars' orbital position is Deimos' inclined orbit, due to which the sail acceleration experienced by the spacecraft varies depending on the location of Mars in its orbit. The results obtained are shown in Fig. E.2, where ballistic flights up to 0.20 days were found to impact the moon immediately. Thus, including some factor of safety, 0.25 days was chosen as the constant ToF for the ballistic segment. Additionally, it is noted that the other outliers impacting the moon at higher ballistic ToFs do so after moving away from the moon and

not immediately. This occurs due to a specific orientation of the Sun in the Mars-Deimos system, causing the sail-perturbed trajectory to run back into the moon.

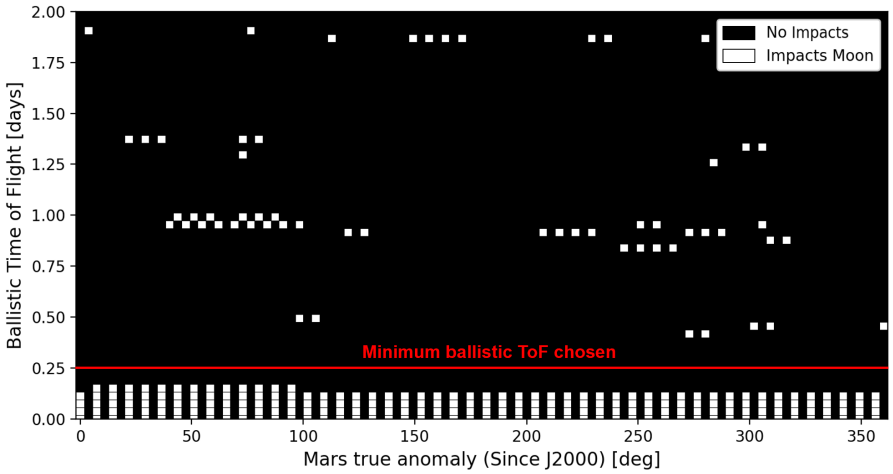

Figure E.2: Selection of the time of flight for the ballistic segment. Mars' initial position is taken at J2000, for a circular orbit around the Sun. The black regions indicate no impacts, while the white grids are associated with impacts with Deimos. This was plotted for the unstable manifold from Mars-Deimos L_1, the same results were observed for the stable manifold.

Linkage errors as a function of cone and clock angles

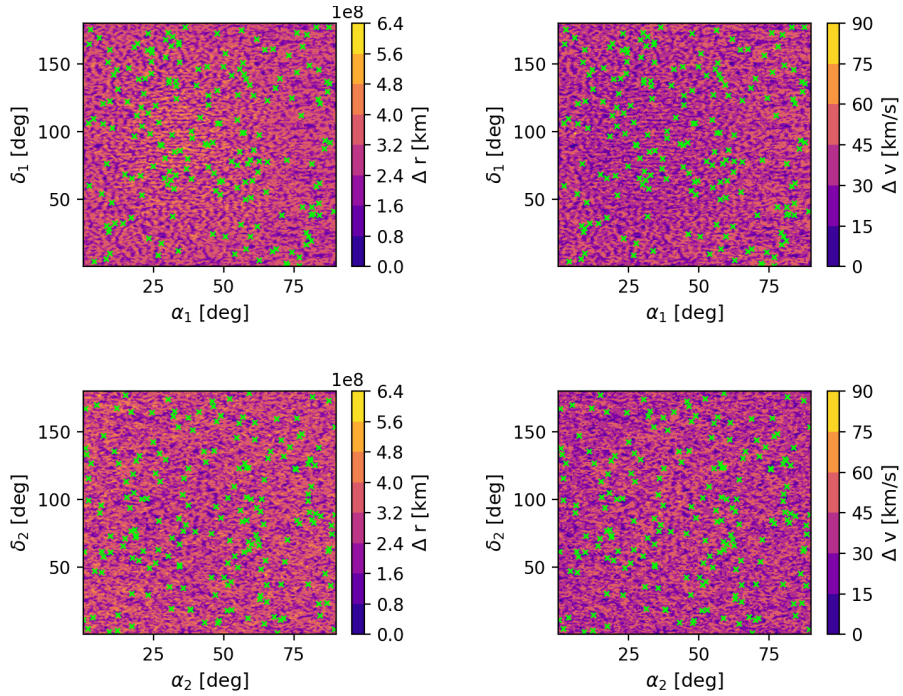

Figure E.3: Position and velocity errors at linkages shown for combinations of cone and clock angles for mission leg 1. α_1 and δ_1 correspond to the cone and clock angles of the unstable manifold (from Sun-Earth L_2), respectively, and α_2 and δ_2 to that of the stable manifold (from Mars-Deimos L_1). The green crosses represent the designs that impacted either Deimos or Mars.

Figure E.3 is a result of the Monte Carlo analysis where the position and velocity errors at linkages for mission leg 1 are shown as a function of cone and clock angles. It is evident from the figure that no clear correlation between the attitude angles and linkage errors exists.

Escape and capture spiral trajectories

Figure E.4 is a plot between the time of flight of the escape trajectory and the departure epoch. It clearly illustrates that similar to the capture trajectory, the minimum and maximum values of the escape time vary periodically with the epoch at departure from Deimos - with a half Martian year period.

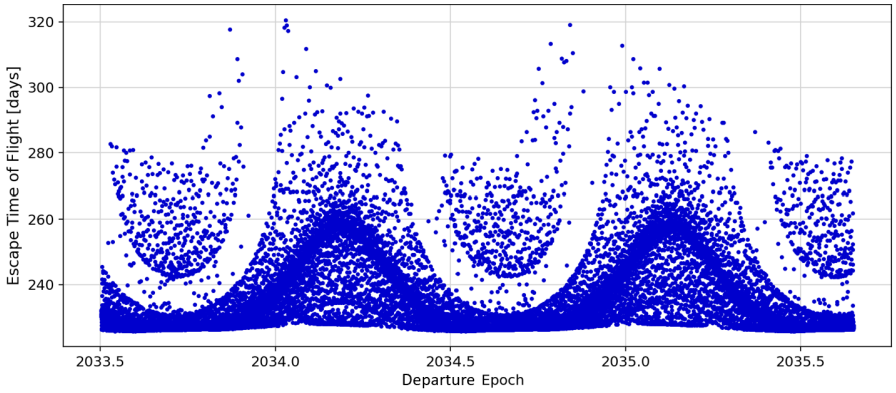

Figure E.4: Escape time of flight plotted against the departure epoch for mission leg 2

Figure E.5 shows the locations from which the trajectories either escape or get captured on the Martian sphere of influence (SOI) for varying spiral ToF. To facilitate the depiction of these locations on the SOI, spherical coordinates of right ascension and declination are utilized. This assumes a frame centred at Mars in a Sun-Mars CR3BP system, with the x-axis pointing along the Sun-Mars line (opposite to the Sun), the z-axis normal to the Sun-Mars plane, and the y-axis completing the right-handed reference frame. Right ascension is positive along the positive y-components, while declination is positive along the positive z-component. The figure illustrates that the solar sail consistently escapes or enters the Martian SOI from the anti-sun direction. Spiral times are almost uniformly distributed about the declination, but exhibit smaller times at large right ascension. The capture trajectories enter at negative right ascension while the escape exits at positive right ascensions.

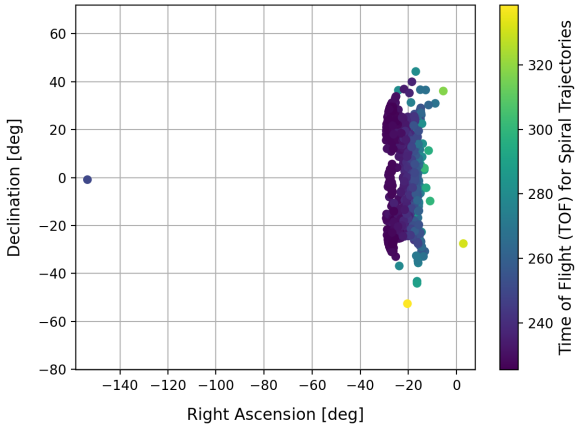

(a) Capture trajectories - leg 1

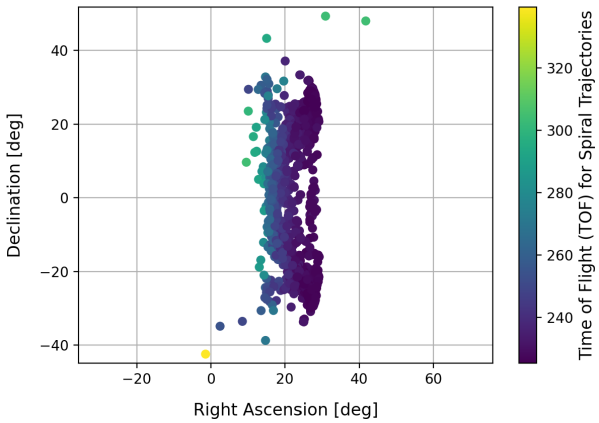

(b) Escape trajectories - leg 2

Figure E.5: Locations at the Martian sphere of influence at which the trajectories either escape or get captured. Their respective time of flights within the Martian system are also specified.

Figures E.6 illustrate the orientations of Deimos' orbit in the Sun-Mars frame at departure/arrival, using the right ascension of ascending node (raan), for which minimum and maximum escape (Fig. E.6b) or capture times (Fig. E.6a) are observed. The raan used here is defined with respect to

the x-axis pointing on the Sun-Mars line centred at Mars, similar to the right ascension along the Sun-Mars plane, i.e. the ecliptic in this study. The majority of obtained solutions that exhibit small or large spiral times are seen to be spaced by almost 180 deg, indicating that the orientation of Deimos's orbit at the time of departure/arrival in the Sun-Mars frame indeed causes the capture/escape times to behave periodically, as shown in Fig. E.4. This periodic behaviour is attributed to certain orientations allowing for a better alignment of the orbital velocity vector and the sun-sail line, resulting in a larger sail acceleration available to be directed along the velocity vector.

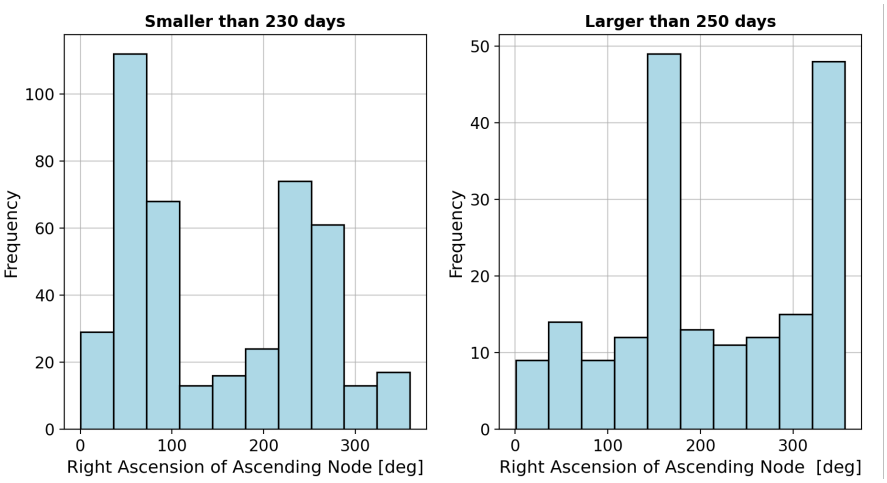

(a) Capture trajectories.

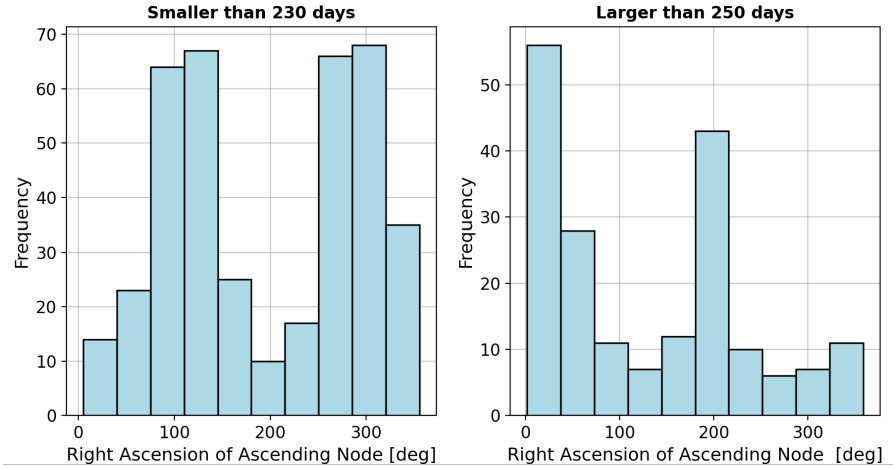

(b) Escape trajectories.

Figure E.6: Frequency distribution of trajectories with spiral time of flights less than 230 days and greater than 250 days for varying values of the right ascension of ascending node of Deimos' orbit on the ecliptic at the time of departure or arrival.

Complementary figures for the optimal trajectories

Figure E.8 depicts the interplanetary trajectories for both leg 1 and leg 2 plotted with coordinate axes unequally scaled, plotted in the heliocentric inertial reference frame. It clearly illustrates how the sail's optimal interplanetary control profile changes the inclination of the trajectory to either rendezvous with the state at the Martian SOI for leg 1 or at the SE-L_1 point for leg 2.

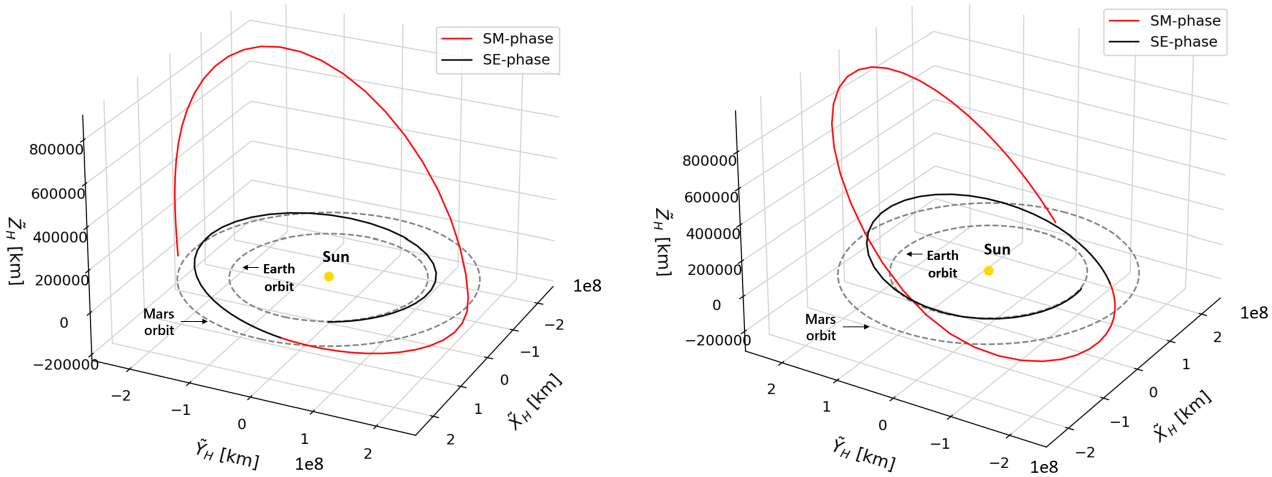

(a) Leg 1 **(b)** Leg 2

Figure E.7: Alternate view of the PSOPT obtained optimal interplanetary trajectories with coordinate axes not scaled equally. It is plotted in the heliocentric inertial reference frame.

Figure E.8 shows how the inclination of the locally optimal capture or escape trajectories changes with time in the Sun-Mars CR3BP frame with the coordinate axis centred at Mars. The inclination monotonically increases during the escape spiral and decreases during the capture phase. This complements the explanations provided in the conference article for the obtained control profiles.

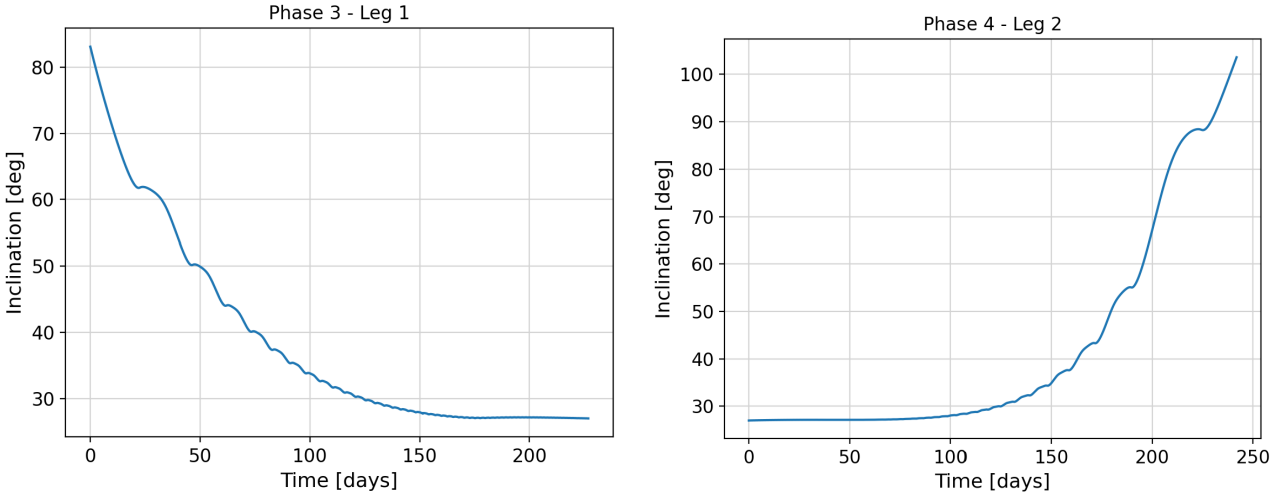

(a) Capture Spiral - Phase 3: From Martian SOI to MD-L_1 **(b)** Escape Spiral - Phase 4: From MD-L_1 to Martian SOI

Figure E.8: Varying inclinations of trajectories arriving at or departing from the Mars-Deimos L_1 point within the Martian SOI with respect to the Sun-Mars plane.